NOISE REDUCTION CONTROL STRATEGY OF A PERMANENT MAGNET SYNCHRONOUS MACHINE FOR VEHICLE APPLICATIONS

A Thesis

by

RANDY GENE DOOLITTLE

Submitted to the Office of Graduate Studies of
Texas A&M University
in partial fulfillment of the requirements for the degree of

MASTER OF SCIENCE

May 2008

Major Subject: Electrical Engineering

NOISE REDUCTION CONTROL STRATEGY OF A PERMANENT MAGNET SYNCHRONOUS MACHINE FOR VEHICLE APPLICATIONS

A Thesis

by

RANDY GENE DOOLITTLE

Submitted to the Office of Graduate Studies of
Texas A&M University
in partial fulfillment of the requirements for the degree of

MASTER OF SCIENCE

Approved by:

Chair of Committee,	Mehrdad Ehsani
Committee Members,	Prasad Enjeti
	Jim Xiuquan Ji
	Robert Shandley
Head of Department,	Costas Georghiades

May 2008

Major Subject: Electrical Engineering

ABSTRACT

Noise Reduction Control Strategy of a Permanent Magnet Synchronous Machine for Vehicle Applications. (May 2008)
Randy Gene Doolittle, B.S., Texas A&M University
Chair of Advisory Committee: Dr. Mehrdad Ehsani

The purpose of this work was to investigate a permanent magnet synchronous machine which will be produced by an industry partner of the Institut für Stromrichtertechnik und Elektrische Antriebe (ISEA) an institute of the Rheinisch Westfälisch Technische Hochschule - Aachen, Germany (RWTH).

The machine manufacturer noted certain abnormalities with the frequency spectrum produced by an electric machine that they were developing; this problem was brought to ISEA in order to be investigated. My work continues the work of my supervisor, Dipl.-Ing Matthias Bösing, and seeks to further examine the machine for a much wider range of operating points, determine the relationship between current amplitude, harmonics, control angle and rotor position on radial force components of the machine and therefore stresses on the stator; which are the primary causes of electrical machine noise. Rather than investigate acoustic issues in particular, the study was limited to the study of electromagnetically generated radial force ripple, which is the cause of stator deflection modes and therefore the emission of sound waves.

The primary results of this thesis researched the operation of a permanent magnet synchronous machine and described its behavior with regards to force, torque, and force and torque ripple and their spectrums versus numerous parameters, including control angle, secant current and rotor position. Next, the work used provided data, literature and the simulation results for this thesis in order to deconstruct the operation regions of

the particular machine and therefore link the causes of particular noise spectral components to the operation of the machine. From this it was possible to identify potential ways to eliminate these areas of noise. Following this, the thesis examined a particular abnormality in the torque and force waveforms produced by the machine and devised actions which could correct this abnormality. After identifying this asymmetry, the work explored how to choose an optimal control strategy for eliminating particular harmonics based on the simulated operating points and a desired command torque. Finally, the research built on the previous work by supplementing the method of current harmonic injection for eliminating radial force harmonics in this machine, with a method of determining an optimal operating point before the injection currents are calculated.

DEDICATION

This work is dedicated to my wife and my parents, who have done everything they could to support me in my endeavor of academic achievement. Particularly I dedicate this work to my father, who did not live to see its completion, but always did everything he could to ensure that despite our meager means, I made it through college.

ACKNOWLEDGEMENTS

I, Randy Gene Doolittle, hereby declare that this submission, except for the supervision by the Institute for Power Electronics and Electrical Drives (ISEA) of RWTH-Aachen, is solely my own work. Information derived from the published or unpublished work of others has been acknowledged in the text and a list of references is appropriately given following the text.

Aachen, Germany; February 28, 2008

During the completion of the work for my master's degree, I completed a Diplomarbeit, albeit unofficially, at the Institut für Stromrichtertechnik und Elektrische Antriebe (ISEA) an institute of the Rheinisch Westfälisch Technische Hochschule - Aachen, Germany (RWTH). I was able to do this through the cooperation of the institute's Director, Univ.-Prof. Dr. ir. Rik W. De Doncker and the approval of my own professor Dr. Mehrdad Ehsani. I wish to thank both gentlemen for their flexibility in allowing me to add an international component to my graduate studies, allow me to learn how German students are educated and how to better interact with German engineers. I would also like to thank my supervisor, Dipl.-Ing Matthias Bösing, for taking on an international student as one of his first Diplomanden. I know that my special situation posed unique difficulties, but I hope that he gained some experience from me, as I did from him. Finally, I would like to thank all of my lab mates at the Power Electronics and Motor Drives Laboratory (PEMDL) at Texas A&M University, particularly Alex Skorcz and Hugo Mena, who inspired me to stay at Texas A&M for my masters degree and without whose help and friendship my graduate studies would have been far less enjoyable.

TABLE OF CONTENTS

CHAPTER Page

LIST OF FIGURES

Page

Page

Page

LIST OF TABLES

CHAPTER I

INTRODUCTION

Since the beginning of the industrial revolution man has increasingly relied on fossil fuels in order to power his progress in industry. After more reliable and efficient electric machines replaced coal and petroleum fired steam machines during the second industrial revolution, huge power plants were built to efficiently produce electricity for these electric machines. During the same time frame, practical petroleum powered vehicles were developed in Germany by Karl Benz among others, replacing earlier alcohol, hydrogen and electrically powered vehicles.

Industrial and technological gains over the last 100 years have been directly proportional to the ever increasing use of energy and have transformed man and the world he lives in. Adjustable speed drives (ASDs) continue this industrial progression, while improving the use of existing energy and due to the uncertain future and side-effects of fossil fuels that power both the automobile and the majority of electricity production, these advances are desperately in need.

1.1 – Modern Energy Consumption and Unwanted Side-Effects

The two major consumers of fossil fuels and therefore producers of unwanted pollution, particularly in the form of greenhouse gasses and chiefly carbon dioxide (CO_2), are the power generation industry and transportation industry. More precisely the use of transportation and electric products whose source energy derives from fossil fuels is the source of the pollution. The machine investigated in this thesis is intended for use in the transportation industry and therefore these issues related to the transportation sector will be stressed.

This thesis follows the style of *IEEE Transactions on Industry Applications.*

1.1.1 Oil, the Economy and the Future

Scholars, oil corporations and world governments have known for years that the proved reserves of petroleum cannot meet the rising future demand for petroleum. If technology cannot significantly offset the demand for petroleum products in the near future, the supply of oil will run out. As shown in [1], the growth of demand is particularly high in the Asia-Pacific region, where industrialization and personal wealth growth, primarily in India and China, has pushed demand for petroleum up 50% between the years 1980 and 2000. Comparatively the rest of the world, including that region, has only seen an increase of 16% during the same time frame. The world has 1,312 billion barrels of technically available proved oil reserves, led by Saudi Arabia at 264.2 billion barrels (20.1%) and followed by Canada with 178.8 billion barrels (13.6%). The world consumes 82.59 million barrels of oil per day, easily led by the United States at 20.73 million barrels per day and followed by the European Union (EU) at 14.68 million barrels per day. Using these estimates and assuming no increase in consumption, which is unlikely; unless new technologies are heavily utilized, the last year of oil availability will in the next 35-40 years, less than 200 years after its first use as a transportation fuel [1],[2],[3].

As noted above, the United States consumes 20.73 million barrels of oil per day, which is 25% of the world's consumption. However, the US only produces 7.61 million barrels a day and actually exports 1.048 million of those barrels, thus having to import 13.15 million barrels of oil per day, with the largest percentage 17.3% of that coming from Canada [2]. This need for crude oil is a significant part, 152 billion dollars (8.2%), of US total imports with a value of 1.861 trillion dollars. Partially due to a hunger for foreign energy products the trade deficit was 811 billion dollars in 2006. With the rising cost of crude oil, hitting over 100 dollars per barrel in both January and February of 2008, the cost of imported oil will reach 476 billion dollars in 2008, or 312% of the cost of the same volume of oil in 2006 [2].

Tensions over future energy supplies and the costs of those supplies, combined with the notoriety of the topic of global warming from the movie "An Inconvenient Truth," have raised awareness about environmental topics. The movie, starring Albert A. Gore Jr., combined with the efforts of the United Nations Intergovernmental Panel on Climate Change (UN-IPCC) earned both parties a share of the 2007 Nobel Peace Prize. One of the members of the UN-IPCC who received a portion of the Nobel Peace Prize was a Texas A&M researcher, Dr. Bruce McCarl, who studies the impact of climate change on agriculture and therefore the economic and geopolitical impact of our energy production, use and how that threatens the peace of the planet [4].

1.1.2 Oil and Carbon Dioxide (CO_2)

A chief amongst greenhouse gasses is CO_2 which is a primary product of burning fossil fuels, along with energy in the form of heat. Since 40% of US energy use comes from petroleum, 38% used in the transportation sector and 2% elsewhere, it shows that a significant amount of the total CO_2 production of the US comes from the transportation sector. The combustion of a hydrocarbon is shown verbally in Equation 1.1 and then chemically in Equation 1.2 [5].

$$Hydrocarbon + Air \rightarrow Heat + Water + CarbonDioxide + Nitrogen \qquad (1.1)$$

Or more specifically, depending on the composition of the hydrocarbon, the more carbon atoms in the hydrocarbon chain, the more CO_2 is released based on the generalized hydrocarbon-air combustion equation below.

$$C_xH_y + (x + \frac{y}{4})O_2 + 3.76(x + \frac{y}{4})N_2 \rightarrow xCO_2 + (\frac{y}{2})H_2O + 3.76(x + \frac{y}{4})N_2 \qquad (1.2)$$

This is the ideal stoichiometric combustion of a hydrocarbon and air and the resulting flue gasses, the reality is that the combustion, nor the fuel, is ever ideal and results in various extra byproducts such as nitrous oxides (NO_x), carbon monoxide (CO), sulfur dioxide (SO_2) as well as unburned hydrocarbons, particularly when a rich air fuel mixture is used (over 12.5:1 for an internal combustion engine (ICE) using gasoline). Equation 1.2 also shows that the variable "x" governs the number of CO_2 molecules released per combustion reaction. The problem is of course, the most energy in a hydrocarbon resides within its carbon double bonds. Therefore, the larger "x" is, the more volumetric energy density that hydrocarbon has as a fuel, which makes it better as a transportation fuel and worse for CO_2 emissions.

Another important factor to the volumetric and gravimetric energy density of a fuel is the amount of oxidizer contained in the fuel hydrocarbon. Fuels which are liquids at standard temperature and pressure (STP) are inherently more efficient than fuels which are gaseous due to compression, tankage, distribution and combustion energy losses [6]. In transportation applications, combustion has an ever-present oxidizer, namely air, and only requires the molecule to have more oxidizer in situations where high revolutions per minute (RPMs) or high compression ratios can necessitate the need and usefulness of the fuel having its own oxidizer [6]. Alcohol fuels (ethanol, methanol, nitro-methane) are used in high power ICE applications where a fuel containing its own oxidizer is beneficial, because of both high RPM and high compression. However, for economical energy density the relationship between those fuels is likened to that of batteries and ultra-capacitors. The same study showed that fuels which are liquids at standard temperature and pressure are the best fuels for transportation applications and further demonstrated that diesel fuel, particularly from a renewable source, when utilized with highly efficient small ICEs could provide a more efficient way to utilize liquid fuels in conjunction with available automotive transportation, which would create lower CO_2 emissions from the transportation sector, while retaining the desirable liquid phase-state of a transportation fuel. Such a system could potentially bridge the gap until improved

electrochemical technology and wider consumer adoption of alternative powered vehicles combined with the development of mass transportation solutions such as high speed trains and regenerative busses are realized in the United States [7].

1.2 Adjustable Speed Drives and Vehicular Applications

In the past 20 years ASDs have progressed with advancements in the solid state semi-conductors used to control the machines. This paired with ever-improved computer modeling and design of electric machines, drive technology has a higher efficiency and understanding than ever before [8],[9]. While those advances had an impact on all ASDs, of particular interest is the improvements and cost reduction of permanent magnet materials leading to more wide scale use of permanent magnet machines (PMMs).

Due to these improvements the price point for all ASDs, particularly PMMs, has dropped substantially and when combined with their long-term energy cost reduction, maintenance cost reduction, space reduction and high performance; ASDs are a rapidly growing market. Also, the power curve of an internal combustion engine (ICE) behaves poorly naturally and must be manipulated by a multi-gear transmission and differential in order to more closely mimic the natural response desired by the load and expected driving conditions. An ASD however naturally is controlled to meet the desired performance of the application [10]. The space reduction due to higher power density and higher performance have made this type of machine the preferred platform for automotive applications where space is at a premium and efficiency equates to vehicle range.

1.2.1 ASD Benefits to Fuel Savings in Traffic

More than half of Americans live within 20 miles of where they work equating to approximately a 40 mile round trip daily. If ASD technology is used as part of a plug in hybrid platform, such a range with current technology does not require gasoline at all. If one extends this daily drive to 30 mile one way makes some small gasoline necessary to charge the batteries during the trip, but only using current technology the ability is there to reduce the dependence of transportation on oil, if the mentality of American drivers was to change [11].

This is important because CO_2 production issues, particularly in Europe as well as the growing petroleum costs have forced automakers to look at differing approaches to vehicles including, hybrid, diesel, fuel cell and alternative fuel vehicles, which are all growing in acceptance and prominence. According to [12], consumers in the United States spent wasted 2.9 billion gallons of petroleum products (gasoline, diesel) while sitting in traffic costing the US economy a total of 78.2 billion dollars or 0.5% of the GDP for 2006 [3]. Hybrid and other emerging vehicles do not need to operate their internal combustion engines at low revolutions per minute < 2000 (RPMs) and low loads, where internal combustion engines (ICEs) are only maximally 17.1% efficient and more realistically near 10% [1]. In fact, low-speed "stop and go" city driving is where most people use their vehicles and the place where ASDs perform best when compared to ICEs.

1.2.2 BWM Mild Hybrid Mass Introduction

Because the majority of people drive only a small distance and in urban traffic areas BMW AG has taken a large step to improve efficiency in their fleet. BWM has added as standard feature to their entire 2008 1-Series "start and stop" technology using an integrated starter generator (ISG) [13],[14]. This system uses an electric motor to act as

a generator to charge batteries and provide electric power to the vehicle when it is in traffic, at low speeds or at a stop, at which time the ICE is shut down. Upon higher speed operation or low battery charge the electric machine is also used as a starter in order to "turn over" the ICE to begin operation again. After the ICE is started again, the electric machine may act as a load to charge the batteries. A similar system has been employed by GM on its Silverado and Sierra trucks where a 42V belt driven ISG can provide between 7-10% fuel economy savings [15]. Although, this is defined by many as a "mild-hybrid," BWM has been very careful not to market the technology as such and rather is going to quietly incorporate this efficiency feature as part of their standard package, most likely gauging whether the technology performs well on a large scale and can be reliable to scale to the rest of their fleet. Incorporation into their entire fleet would increase the fuel efficiency by of the entire BMW product line as a whole and create a competitive advantage which would likely force the response of other manufacturers.

1.2.3 Toyota Prius

In the automotive sector there are primarily two platforms to work with as a hybrid researcher, as one will encounter patents from either two companies as they work on this technology. The first is the Toyota Motor Corporation, the world's second leading automaker, whose Toyota Hybrid System, Hybrid Synergy Drive (HSG) and successful Prius model made much of the automotive industry take notice of hybrid vehicles since its release in 1997. In the first 10 months of 2007, the Prius model sold 137,114 units in the US, which is projected to account for 54% of all hybrid sales in the US. However, the total penetration of the hybrid market is still limited, only estimated to move 300,000 units, or 2%, of the expected 16 million new automobiles purchased in the US in 2007 [16],[17].

1.2.4 General Motors and Full Hybrid Market

The second major hybrid manufacturer is the General Motors Corporation, the world's leading automaker, who in conjunction with its Global Hybrid Cooperation (GHC) partners, Daimler AG, BWM AG and Chrysler LLC, have developed hybrid technology based on GM and Allison's Advanced Hybrid System two-mode (AHS-2) parallel hybrid patents. This platform is designed as a torque coupling platform based on two PMSMs and an ISG mounted in a conventional rear wheel drive (RWD) multi-gear transmission casing, making it easily integratable into a standard luxury, truck or sport utility vehicle RWD vehicle chassis [14],[17],[18]. Figure 1.1 below is an illustration of the AHS-2 full hybrid system as realized into a product for BWM. The two electric motors allow the entire system of the ICE, the two electric motors and the drive shaft to function like a continuously variable transmission [18]. The platform is very similar to the SEL Transmission developed at the Technische Universität Chemnitz in a project lead by Prof. Dr.-Ing Peter Tenberge in 2000 [19]. Because of its positive torque coupling characteristics, when compared to Toyota's technology, the members of the GHC chose to work together with GM, rather than license Toyota's technology [17].

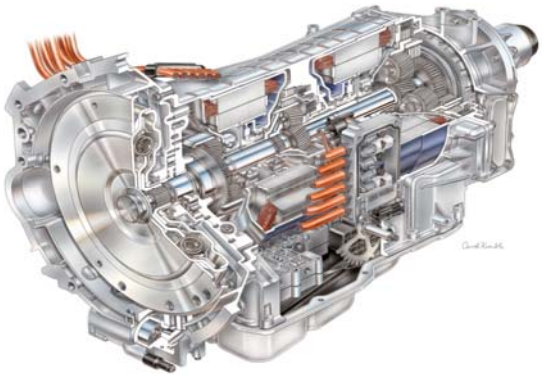

Figure 1.1 Cutaway Schematic of the BMW Model of the AHS-2 [14]

The members of the GHC will release nine hybrid trucks or SUVs in the 24 months following November 2007; these models are listed in Table 1.1 on the following page, which includes past, present and known future hybrid vehicle models and is color coded by manufacturer technology platform. Table 1.1 is an expanded and improved version of tables found in [11],[20],[21]. This table clearly shows that automakers are either pairing primarily with the technology of Toyota or GM, with a few other automakers grouping together to form smaller groups.

The most impressive change listed in Table 1.1 is that several GM based models which previously incorporated mild-hybrid technology will become full hybrids utilizing the AHS-2 platform of the GHC. The Chevrolet Silverado and its twin the GMC Sierra will become full hybrids with the 2008 models, both of which have been mild hybrids based on induction machine ISGs since the 2005 model. In switching from the belt driven induction machine ISG to a full hybrid utilizing PMSMs, the truck will improve from 7% fuel efficiency savings to up to 25% [15],[16]. Also, of note the Chrysler Aspen and Dodge Durango SUVs are expected to improve their city fuel economy by 40% over their respective ICE-only counterparts [17].

Due to the overwhelming prevalence of the PMSM as the machine of choice for traction motor applications, the author chose to research a topic which concentrated on this machine and its corresponding ASD platform. Through previous coursework, the author has learned that the automotive industry has very high inertia, and because the PMSM has been adopted, economy of scale and the previously mentioned machine benefits tells us that its use and development will continue for years to come in the automotive sector.

Table 1.1: List of Numerous Known Hybrid Production Vehicles

Company	Model	Production Years	Hybrid Topology
Citroën	C2/C3C4	2004-Present	Micro-Hybrid (Stop-Start)
Volvo	C30	2008	Full-Hybrid
Audi (Volkswagen)	A4 Duo	1997-1998	
Audi (Volkswagen)	Q7	2008	
Volkswagen	Touareg	2009	
Porsche	Cayanne	2009	
Honda	Accord Hybrid	2005-2007	Mild-Hybrid (IMA)
Honda	Civic Hybrid	2003-2005	Mild-Hybrid (IMA)
Honda	Civic Hybrid (2nd Gen)	2006-Present	Mild-Hybrid (IMA)
Honda	Insight	1999-2006	Mild-Hybrid (IMA)
Nissan	Altima HEV	2007-Present	Full-Hybrid
Mazda	Tribute Hybrid (Ford Escape)	2007-Present	Full-Hybrid
Lexus (Toyota)	GS 450h	2007-Present	Full-Hybrid
Lexus (Toyota)	LS 460h	2007-Present	Full-Hybrid
Lexus (Toyota)	LS 600h	2007-Present	Full-Hybrid
Lexus (Toyota)	RX 400h	2005-2009	Full-Hybrid
Lexus (Toyota)	RX 400h (3rd Gen)	2009	Full-Hybrid
Toyota	Camry Hybrid	2007-Present	Full-Hybrid
Toyota	Prius	1997-2005	Full-Hybrid
Toyota	Prius (2nd Gen)	2005-2008	Full-Hybrid
Toyota	Prius (3rd Gen)	2008	Full-Hybrid
Toyota	Sienna (3rd Gen)	2008	Full-Hybrid
Toyota	Highlander Hybrid	2005-2007	Full-Hybrid
Toyota	Highlander Hybrid (2nd Gen)	2007-Present	Full-Hybrid
Toyota	Alphard	2002-Present	Full-Hybrid
Ford	Fusion Hybrid	2008	Full-Hybrid
Ford	Escape Hybrid	2005-Present	Full-Hybrid
Mercury (Ford)	Milan Hybrid (Fusion Twin)	2008	Full-Hybrid
Mercury (Ford)	Mariner Hybrid (Escape)	2005-Present	Full-Hybrid
BMW	1-Series	2007-Present	Mild-Hybrid (ISG)
BMW	X6 Active Hybrid	2008	Full-Hybrid
Mercedes-Benz (Daimler)	ML450 Hybrid	2009	Full-Hybrid
Mercedes-Benz (Daimler)	S-Class	2009	Mild-Hybrid
Chrysler	Aspen	2007-Present	Full-Hybrid
Dodge (Chrysler)	Durango	2007-Present	Full-Hybrid
Saturn (GM)	Aura Hybrid "Green Line"	2008	Mild-Hybrid (BAS)
Saturn (GM)	Vue Hybrid "Green Line"	2007-2008	Mild-Hybrid (BAS)
Saturn (GM)	Vue Hybrid AHS-2 "Green Line"	2008	Full-Hybrid
Cadillac (GM)	Escalade	2008	Full-Hybrid
Chevrolet (GM)	Malibu Hybrid	2008	Mild-Hybrid (BAS)
Chevrolet (GM)	Equinox	2008	Full-Hybrid
Chevrolet (GM)	Tahoe	2007-Present	Full-Hybrid
Chevrolet (GM)	Silverado Classic 15 Hybrid	2005-2007	Mild-Hybrid (BAS)
Chevrolet (GM)	Silverado Hybrid	2008	Full-Hybrid
GMC (GM)	Yukon	2007-Present	Full-Hybrid
GMC (GM)	Sierra Classic 15 Hybrid	2005-2007	Mild-Hybrid (BAS)
GMC (GM)	Sierra Hybrid	2008	Full-Hybrid

1.3 Thesis Overview

In Chapter II, Permanent Magnet Machine topologies will be introduced and equations will be shown for the Permanent Magnet Synchronous Machine in general. Following that in Chapter III, the specific PMSM that was investigated in this thesis will be introduced as well as a general investigation of its properties and performance. Chapter IV will then define and explore acoustic vibrations in electrical machines in general. Then Chapter V will discuss the analysis, isolation and improvements that could be made to this machine in order to improve electromagnetically produced noise. Finally Chapter VI will state major findings, contributions and specify further work which could be done on the topic of this thesis in further research.

CHAPTER II

INITIAL ANALYSIS OF MACHINE

The first thing which needed to be done was attempt to mathematically derive many basic machine parameters and check all the available information from the industry partner against the ANSYS model provided by the thesis supervisor. Some of the provided tabular results from the industry partner utilize values regarded as unknowns in this study, so they were clearly known to associates who worked for that company; however these values were not released to ISEA. Because of this fact, a creative way to obtain the machine parameters from a static model and the available information had to be developed.

2.1 Introduction to the Investigated Machine

2.1.1 Available Machine Parameters

The information available directly from the industry partner was the following:

1. Geometry (some disagree and are of varying stages of the design process)
2. R_S (the secant resistance) at one temperature value and operating point
3. I_S (secant current), Gamma (γ) (load angle) and average torque (T_{EM} in d-q space for a given ω, γ and $I_{S,RMS}$)
4. Materials, which steel and which magnet composition was used, as well as k_S

The information that was not available:

1. V_S (secant voltage) or a phase voltage to give a value to the BackEMF (E)
2. L_A, L_B, L_C (phase inductances), L_S (secant inductance), or L_D and L_Q
3. λ_D^M (magnet flux linkage) or B_G (air gap flux density)

The thesis supervisor programmed the geometry model using all available information and made reasonable assumptions about unknowns. This thesis continues to work and

improve on this machine model, constructed in the ANSYS Finite Element (FE) program. One pole of the Internal Permanent Magnet Synchronous Machine (IPMSM) is shown below in Figure 2.1. The machine is a 10 pole (p), 60 slot (N_S), dual layer "V" shaped IPMSM. The machine has a full pitch dual layer winding, and of particular interest later is that the eight turns per phase are designed in such a way where it is not possible to increase the turn number.

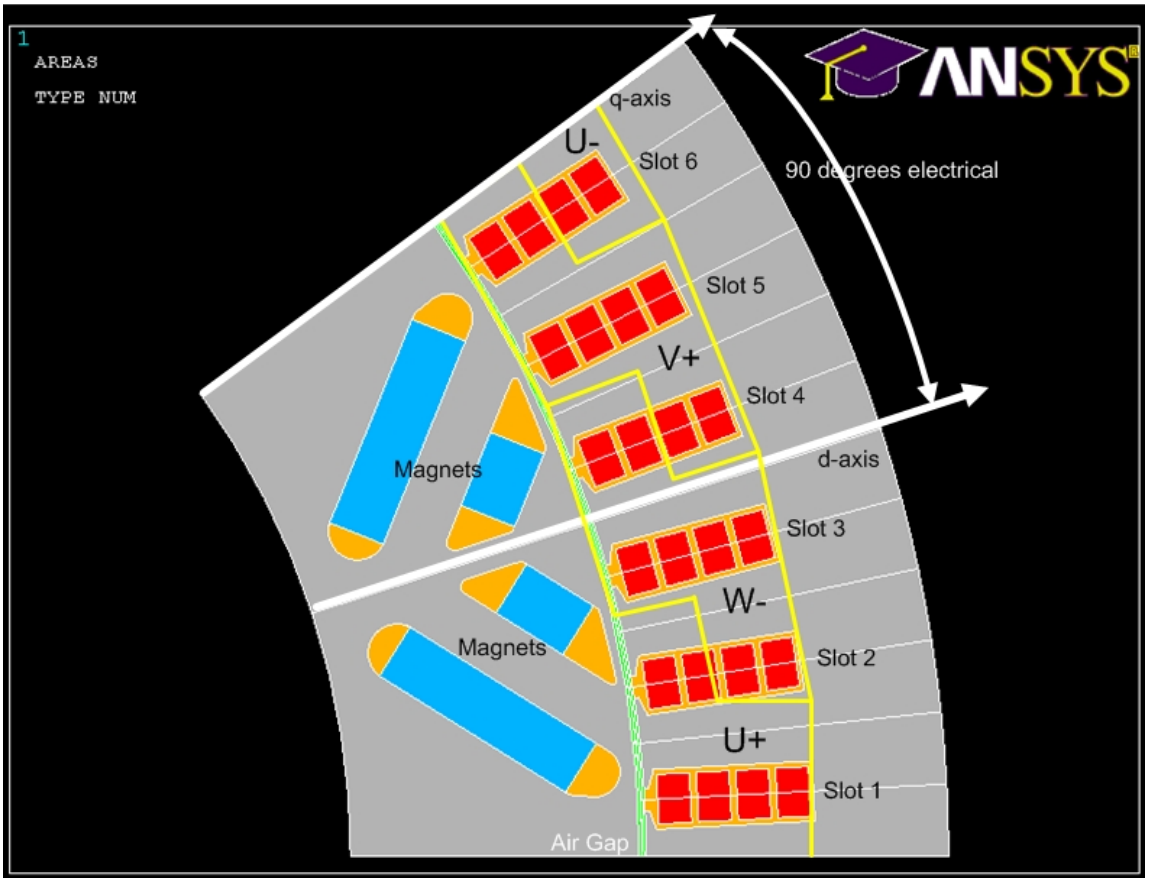

Figure 2.1 Single Pole of a Ten Pole PMSM Similar to the Investigated Machine

A single pole model of a machine is sufficient for 2D analysis in Finite Element Method (FEM) as long as no rotor or stator eccentricities are considered. This is because otherwise no new data is gained by adding more poles as they are identical to the single modeled pole and do note solve the accuracy issues of a 2D model (eddy currents and end winding flux leakage ~5-10% of the magnetizing flux) [21] and adding more poles only adds computation time. Therefore, a single pole model was is sufficient to model the entire 10 pole machine, only the results of the single pole need to be scaled by $p*10 = 10\,poles$ and $(p*10)*0.09$ as the machine stack is 90mm deep and ANSYS assumes a depth of 1m in 2D simulations.

Full geometry was given as well as several other more detailed graphics were given to describe exact slot shape, as well as particular orientations of rotor magnets and flux barriers. The only issue of note is that these other drawings did not agree with each other and it is entirely possible that the data provided to ISEA was a mixture of several design iterations of the machine. On the following page is Table 2.1, this table contains all the machine parameters that the author had available, as well as some which have been previously used in [23] in order to design a PMSM which operated with a very long constant power region similarly to this machine.

Table 2.1 Known Machine Parameters Based on Available Information

Variable	**Motor Type**	**Two Layer "V" Internal PMSM**
m	Phase Number	3
p	Poles	10
q	Slots/Pole/Phase	2
N_S	Slots	60
B_G	Air Gap Flux Density	
$B_{S,max}$	Stator Flux Density	1.7 T (rotor runs in saturation >2.0)
	Stator Material	Laminated Silicon Steel
k_S	Stacking Factor	0.93
	Magnet Material	Neodymium ($Nd_2Fe_{14}B$)
Ratings		
$T_{EM,rated}$	d-q rated Torque	309Nm
$V_{S,rated}$	Secant Voltage	
$I_{S,rated,rms}$	Secant Rated RMS Current	300A
$P_{,rated}$	Rated Machine Power	
$P_{,max}$	Maximum Machine Power	64.5kW
$\omega_{,max}$	Top Speed	
E	Back EMF @ Top Speed	400V (assumed could be 600V)
R_S	Secant Resistance	3.27mΩ @ 300A, 165°C
Motor Size Parameters		all values given in mm
D_{OS}	Outer Stator Diameter	242
D_{IS}	Inner Stator Diameter	187.57
R_{OS}	Outer Stator Radius	121
R_{IS}	Inner Stator Radius	93.785
g	Air Gap Length	0.575
R_{OS}-R_{IS}	Tooth Length Plus Back Iron Width	27.215
W_{BI}	Back Iron Width	12.615
D_{IS}/D_{OS}	Split Ratio	0.775
L_{TOOTH}	Radial Length of Tooth	14.6
W_{TOOTH}	Tangential Width of Tooth	6.046
W_{SHOE}	Tangential Width of Shoe	7.851
W_{SHOE}/W_{TOOTH}	Ratio of Tooth to Shoe Width	1.299
W_{SLOT}	Slot Opening Width	1.97
$W_{BI}/(R_{OS}-R_{IS})$	Ratio of Available Iron for Back Iron	0.463531
$L_{TOOTH}/(R_{OS}-R_{IS})$	Ratio of Available Iron for ToothLength	0.536469

2.1.2 Rotor Reference Frame (d-q Space)

Because the average torque was available to work with, a reasonable place to start was the d-q reference frame, since average torque exists naturally in this frame. Using T_{EM}, I_S and γ as the primary solid data to derive the other machine parameters, the relations shown in Figure 2.2 and Equations 2.1 to 2.10 were found using Quadrant II of d-q space. The relationship in Figure 2.2 represents a lagging power factor common to a system which is heavily inductive, such as an electric machine. Also, according to [24] a lagging power factor in synchronous machines is used in order to achieve maximum torque per ampere operation and optimal decoupling of the transient response.

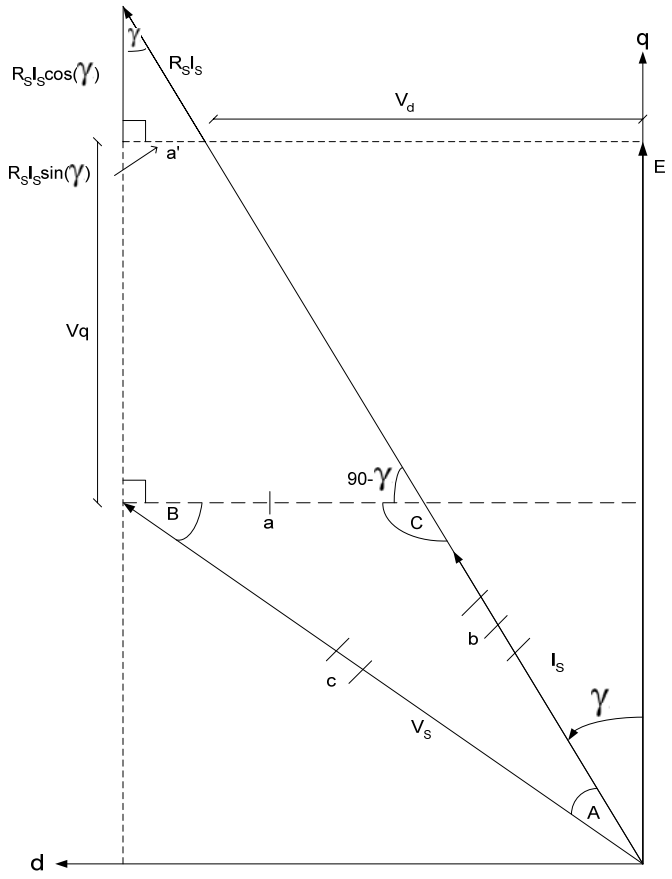

Figure 2.2 Use of Available Parameters to Build a Triangle Based Solution in d-q Space

Utilizing the Law of Sines applied to the machine model in d-q Space and given Is, γ and T_{EM} the following equations are realized.

Solve for:

$$90-(\phi-\gamma) \tag{2.1}$$

$$\angle B = 90-(\phi-\gamma) \tag{2.2}$$

$$\angle A = \phi \tag{2.3}$$

$$\angle C = 90+\phi \tag{2.4}$$

$$\frac{V_S}{\sin(90+\gamma)}\left[\sin(90-(\phi+\gamma)\right] \tag{2.5}$$

After solving for these apply the Law of Sines:

$$\frac{c}{\sin(\angle C)} = \frac{b}{\sin(\angle B)} = \frac{a}{\sin(\angle A)} \tag{2.6}$$

$$\text{We know } V_S = c \text{ and } \angle A, \angle B, \angle C \tag{2.7}$$

This means that you know a and b, and if you know those you can solve for a', which equals $R_S I_S \sin(\gamma)$. Using the property of similar triangles, the right triangle with the sum of V_q and $R_S I_S \cos(\gamma)$ can be found as follows:

$$s = \frac{a'}{R_S I_S \sin(\gamma)} \tag{2.8}$$

$$V_q = (R_S I_S \cos(\gamma))s - R_S I_S \cos(\gamma)) = (s-1)R_S I_S \cos(\gamma) \tag{2.9}$$

$$E = V_q + V_S \sin(90-(\phi+\gamma)) \tag{2.10}$$

The problem with this approach is that one needs L_D and L_Q or E (Back EMF) to complete the equations as:

$$V_q = R_S I_S + \frac{d}{dt}(L_Q I_Q) + \omega(L_D I_D + \lambda_D^M) \tag{2.11}$$

$$V_d = R_S I_D + \frac{d}{dt}(L_D I_D + \lambda_D^M) - \omega(L_Q I_Q) \tag{2.12}$$

The approach has been included due to its usefulness to use known parameters in d-q Space creatively to estimate or calculate other unknown parameters without the need to measure them or have terminal values. The primary goal of discovering L_D and L_Q with this method was not successful as E was needed in order to solve for them.

2.2 Initial Simulations – Testing the Machine for More Information

Because of the lack of success with a mathematical approach, the only other tool was the ANSYS model and scripts provided by Mr. Boesing. The goal of finding machine response and potentially the desired parameters was the goal of the next four tests presented in this section. The first test was a torque versus gamma test, where the response of the machine was observed with changing gamma. The second test was a torque versus rotor position test, followed by a saturation response test.

2.2.1 Torque versus Gamma Response

In this test line current ($I_{LINE,MAX}$) was held constant amplitude as was the rotor position (Θ_M) while the current was phase advanced adjusting gamma in the $\cos(\Theta_E+\gamma)$ equation controlling phase currents. The load angle (γ) was incremented by two electrical degrees (2°_E) from a value of -90°_E (Quadrant I) to 90°_E (Quadrant II); as gamma is defined as the positive counter-clockwise (CCW) rotation of the I_S vector from the Iq axis into Quadrant II in d-q space.

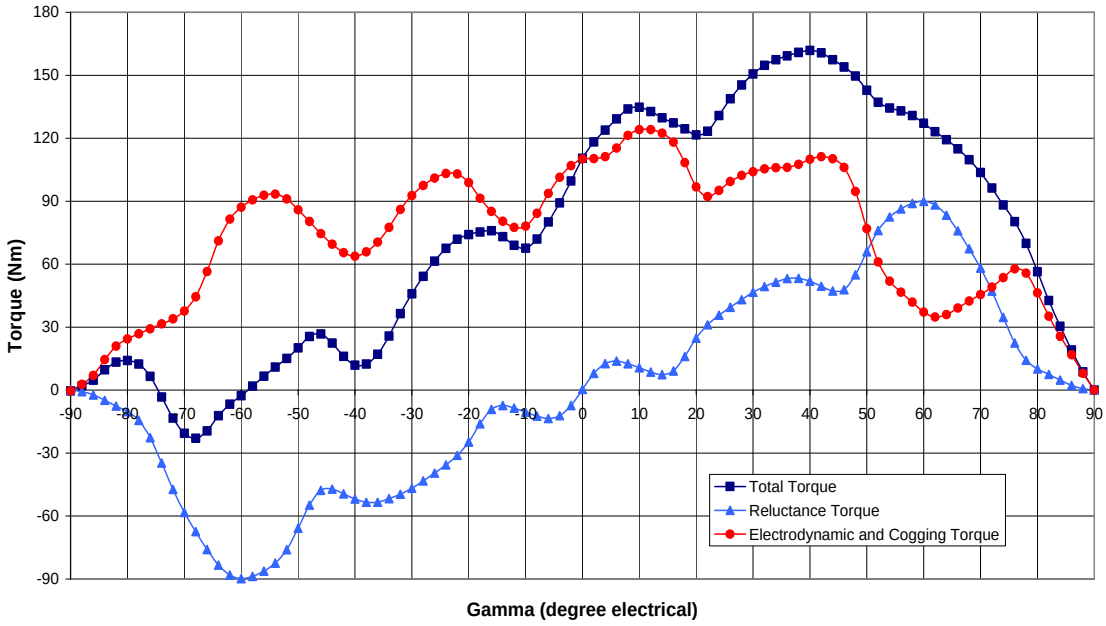

Figure 2.3 Machine Torque Response versus Gamma for 170A $I_{LINE,MAX}$

The response of the machine was as expected by observation of salient and non-salient torque response versus the load angle as shown in [10],[22]. The sweep of gamma behaved as a highly salient machine with interior magnets when compared with a surface or inset magnet machine. This test showed that the maximum torque for this machine is achieved when gamma is 40°_{E}, this result holds at least for lower currents, the saturation test in subheading 2.2.3 shows the effects of higher currents on the response of several machine parameters. The operation current for the initial tests was chosen as 170A $I_{LINE,MAX}$ or 147.22 $I_{S,RMS}$, this is because a parameterization study was done in the work by Dajaku [25], as an initial results chapter to his Doktorarbeit on thermal issues of IPMSMs. This student was working with a completely different company, who just happens to belong to the same research consortium and therefore had a few select results of the exact same machine under investigation in this thesis.

2.2.2 Torque versus Rotor Position

In any PMSM there are three torques, regardless of rotor design, these are:

Electrodynamic Torque – T_E

Reluctance Torque – T_R

Cogging Torque – T_C

And are represented mathematically as:

$$T_{EM} = (\frac{P}{2})(\frac{3}{2})(\lambda_D^M I_Q + (L_D - L_Q) I_D I_Q) \tag{2.13}$$

The sum of these three torques is Total Torque – T_{EM} and is seen from Equation 2.13 above. One might argue that T_R only exists in salient machines, however this is not the case, due to imperfections in manufacturing there is always reluctance torque, even if this value is negligible. The reason that cogging torque does not appear in the equation is because the equation is based on T_{EM}, which is an average torque usually taken over a multiple of the electric period of the machine. Because cogging torque is $1/2 f_E$ periodic and has an average value of 0 by definition, any measured multiple of the electrical period of the machine will not have a cogging torque component in the average torque. However, single rotor positions must account for its value. This periodicy is later exploited to allow for the estimation of λ_D^M (d-axis magnet flux linkage).

2.2.2.1 Total Torque

In order to obtain the total torque, the ANSYS model was provided with purely sinusoidal current waveforms with an 170A $I_{LINE,MAX}$ (147.22 $I_{S,RMS}$) and a gamma of

0°_{E}. The currents and the rotor were then stepped by 2°_{E} over the full simulation angle of 180°_{E} to result in 90 data points. Invoking the MAGSOLV ANSYS macro solves differential equation for the magnetic vector potential in order to solve the magnetic circuit and then the postprocessing TORQSUM macro outputs the total torque for each operating point with respect to the rotor and stator in a text file and uses two methods of Finite Element (FE) solving to provide answers, these two methods are the Virtual Work method and the Maxwell Stress Tensor method. All results in this thesis are oriented to the air gap and use the results provided by the Virtual Work method. The output text files were read into MATLAB by use of an m-file script and then transferred to Excel for manipulation because of personal preference.

2.2.2.2 Cogging Torque

The second test performed was a cogging torque test. To measure this, the $I_{LINE,MAX}$ variable of the simulation control ANSYS script was set to 0A. No current stator excitation results in a cogging torque which occurs due to rotor permanent magnet flux interaction with the varying reluctance of the stator due to slot openings and the amount of reluctance of the circular flux path through the back-iron, the air gap and through the rotor, corresponding to the geometry changes as a function of rotor position.

The results of this simulation were that cogging torque for this machine is roughly sinusoidal with peak amplitude of ~1.5Nm and a frequency of $1/2\,f_E$ or 30°_{E}, as shown below in Figure 2.4.

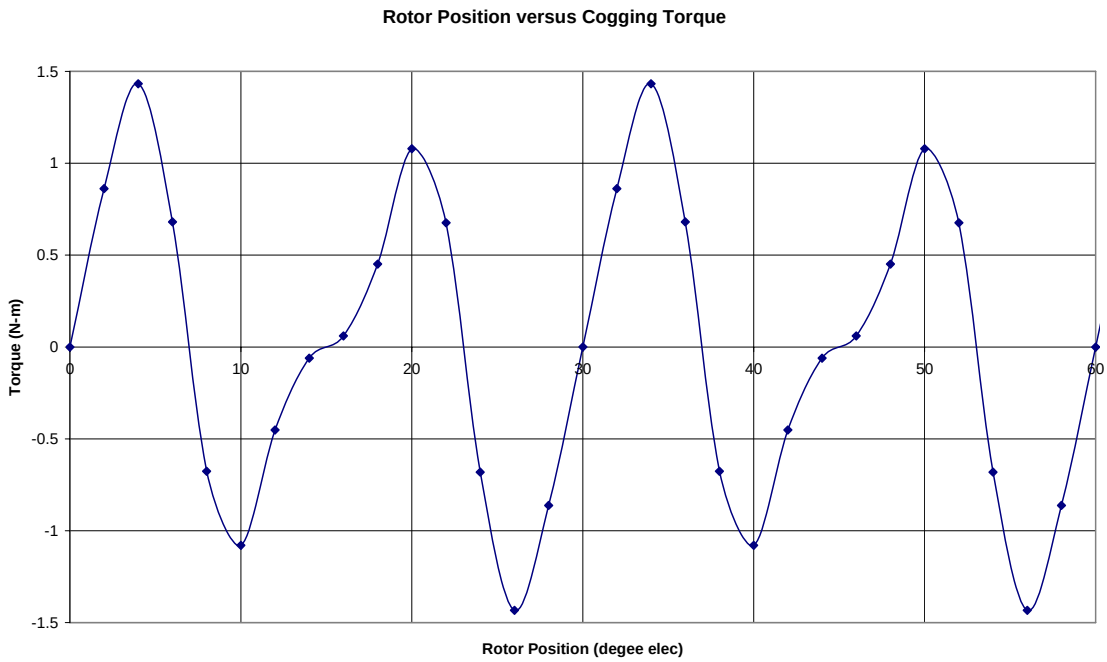

Figure 2.4 Cogging Torque with Respect to Rotor Position

2.2.2.3 Reluctance Torque

Reluctance torque exists in all electric machines to an extent because of manufacturing imperfections resulting in an easier path through the rotor in one of the rotor referred axes d or q. Reluctance is also purposefully utilized by rotors comprised of cold rolled steel, which is magnetically polarized in order to make it easier for flux to travel in one direction. Also, the use of laminated rotors and flux barriers within the rotor can change the reluctance of the rotor by impeding the travel of flux in one direction; typically in an interior permanent magnet synchronous machine (IPMSM) this is in the direction of the q-axis. The saliency ratio of an IPMSM is defined as L_Q/L_D, so the higher the value the more salient the machine is. As Figure 2.3 showed, utilization of reluctance torque allows for a higher maximum average torque and greater operating speed range for a machine.

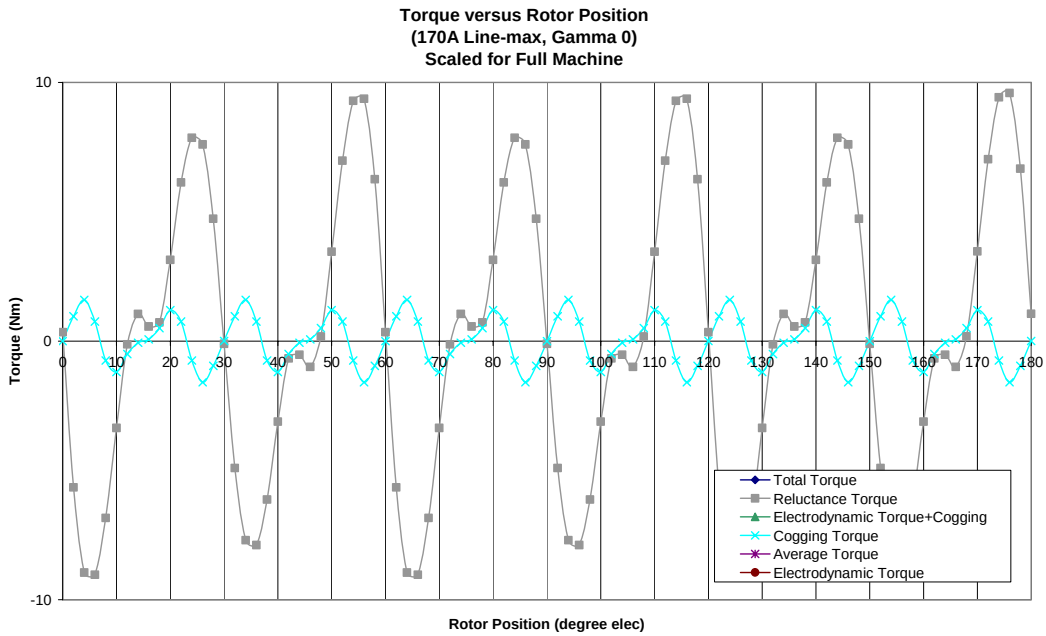

Figure 2.5 Zoomed-In Results of Reluctance and Cogging Torque

The process to obtain reluctance torque for this machine was to set the material parameters of the magnets to that of air, so that the simulation would see the magnets just as part of a flux barrier and the magnets would not interact with the stator flux to create electrodynamic torque. The choice to make the magnets have the same permeance as air is a common assumption among designing surface mounted magnet rotors and seems reasonable[1].

[1] Of course this method is only an approximation of the reluctance torque, because due to the magnets saturating the surrounding rotor iron, particularly the flux bridges used to retain the magnets, the flux flows somewhat differently in the machine during operation. If the fixed permeability method was employed and then the magnets were removed, the flux paths would operate more as they would with the magnets in operation and produce better results. This is because the finite elements would retain the permeability that they had when they were saturated from the magnets and therefore be less conducive to passing more flux though those particular finite elements.

The results in Figure 2.5 show that the reluctance torque is also roughly sinusoidal and periodic over $1/2\,f_E$ or 30°_E, similarly to cogging torque. Maximum reluctance torque positions are at the tooth edges and it has zero amplitude in the middle of each tooth. At 170A $I_{LINE,MAX}$ (147.22 $I_{S,RMS}$) reluctance torque has a maximum amplitude of 10Nm and has a periodic average of 0Nm, which was to be expected using $\gamma = 0^{\circ}_E$ as $I_D = 0$A in that case. This is because when gamma is 0°_E and therefore $I_D = 0$A, there is no contribution to T_{EM} from reluctance torque, so although this value varies absolutely with rotor position, when the Park Transform is applied to move the rotor position based values into d-q space, only the average value of the waveform, namely 0Nm is reflected in d-q space. If a value other than $\gamma = 0^{\circ}_E$ is used, then naturally there would be an I_D current and therefore a non-zero average to the reluctance waveform versus rotor position and likewise a non-zero contribution from the reluctance torque component of the torque equation in d-q space.

2.2.2.4 Electrodynamic Torque

In this model, electrodynamic torque, or the torque produced by the between the d-axis magnetic flux (λ_D^M) and the q-axis flux produced by stator currents and inductance (λ_Q) in quadrature, is not possible to be independently analyzed. The machine has inherent reluctance due to the interior magnets and flux barriers so it is impossible to remove the reluctance without having a completely different machine. However, knowing the rotor position based T_{EM} one can arithmetically subtract the other torque components to discover the electrodynamic torque as shown below.

$$T_E = T_{EM} - T_R - T_C \tag{2.14}$$

The first step was to remove the reluctance torque, which left a sum of electrodynamic and cogging torques, or torques which relate to the magnets directly. Following that,

subtraction of cogging torque left a good estimate of electrodynamic torque, resulting in Figure 2.6 below.

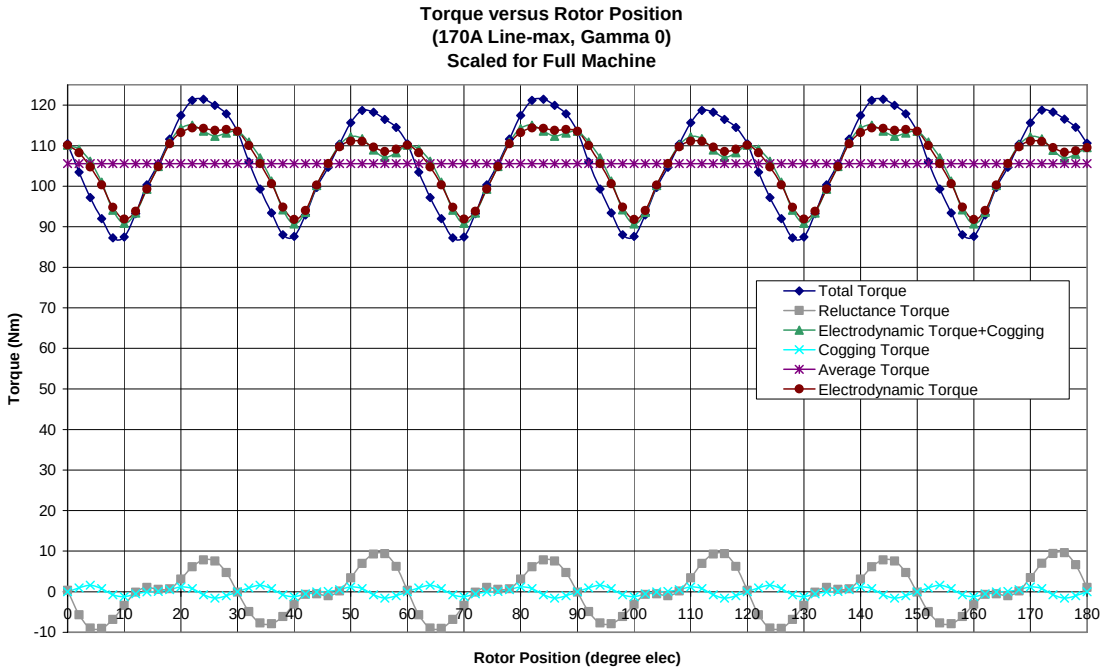

Figure 2.6 Torque Components versus Rotor Position for One Operating Point

2.2.2.5 Torque versus Rotor Position Final Remarks

The key result of this study identified that there is an imbalance of the electrodynamic torque at twice per electrical cycle ($1/2\,f_E$) or 30°_E. This imbalance occurs where the lower peak of the sinusoid was lower than the corresponding regional minimum the next half-cycle. To understand this, look at Figure 3.7 above, the local minimum around 10°_E is lower than the corresponding local minimum the next half-cycle occurring around 40°_E. This same effect occurs also at the local maximums, where the peak at 24°_E is higher than the peak at 54°_E. Because Figure 2.6 has the torque components reduced to their sources, it is easy to determine that the cause of this torque imbalance comes from a "droop," or lower magnitude of electrodynamic torque in the regions where the local

minimum and maximum is too low as shown in Figure 2.7. Aligning these positions where there is a "droop" in electrodynamic torque with the stator teeth and coils, Figure 2.8 on the following page shows that the reduction in electrodynamic torque could potentially come from reduced flux interaction when the d-axis magnet flux is in quadrature with the q-axis flux produced by slots which contain two separate phases.

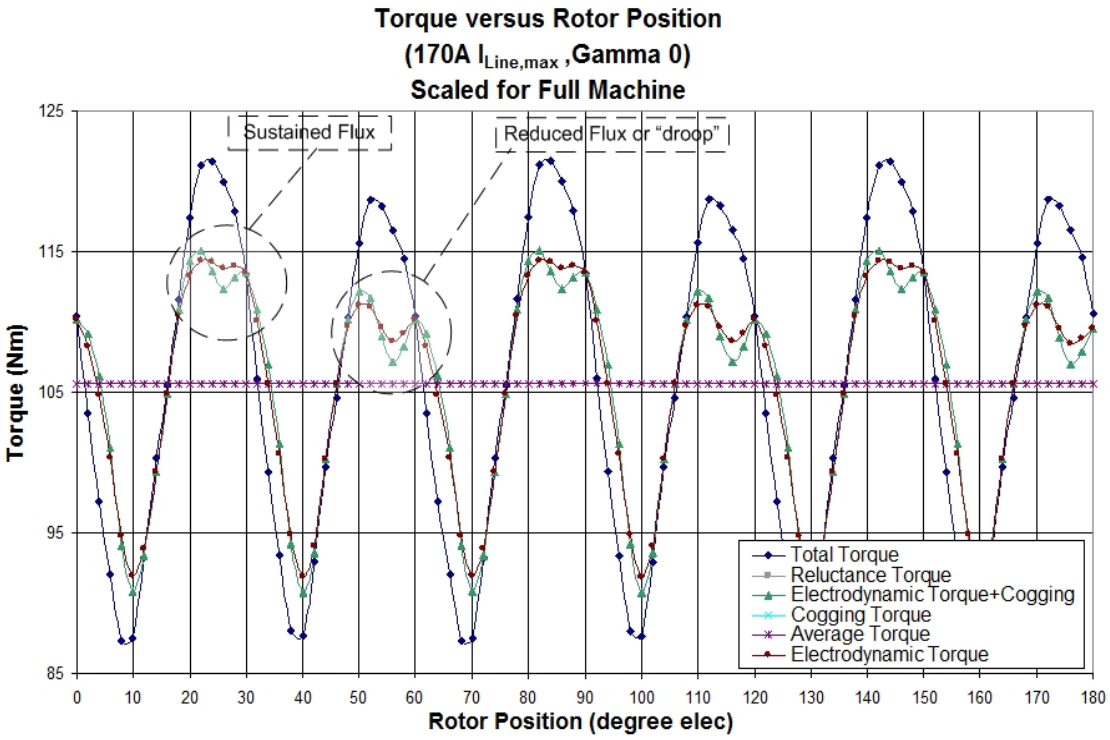

Figure 2.7 Zoomed-In Results of Electrodynamic Torque and the Significant "Droop"

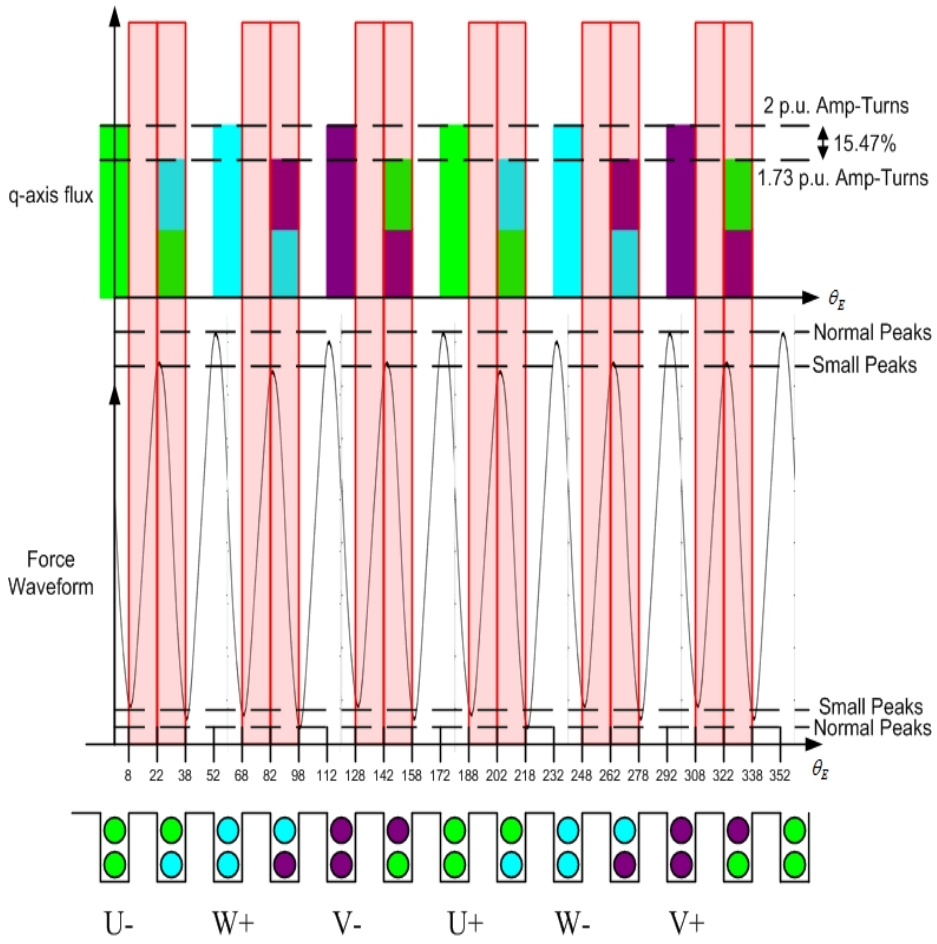

Figure 2.8 Spatial Orientation of Electrodynamic Torque "Droop" versus Flux and Coils

The results presented in Figure 2.8 have a different rotor position reference than earlier because these results came later after a model improvement where rotor position was decoupled from gamma to improve the simulation aspects which relate to reluctance components of operation. Also, due to personal preference and to make the model more closely represent other models in literature, the phase of the supply current waveforms was shifted from the sine function to the cosine function and the starting position of the rotor adjusted accordingly. Figure 2.8 above shows that directly after the rotor passes the point where there is a full phase slot ends at 8°_{E}, the local minimum at 9°_{E} reflects that there is not enough flux in the approaching half phase slot to support the torque waveform and therefore the local minimum is lower than its corresponding local

minimum the next half cycle at 39°_{E}. This decrease in flux from the half phase slot occurs through the half phase slot until the flux level normalizes once the rotor passes the slot wall of the half phase slot at 38°_{E}. This is the point where the d-axis representing the rotor position begins to approach another full phase slot and regains sufficient flux to support the torque waveform; the red highlighted sections of Figure 3.9 represent the region where there is a q-axis flux deficiency. The result of this imbalance, as well as potential corrective actions is explored in Chapter IV.

2.2.3 Saturation Test

Following the two tests to examine the behavior of the machine with respect to rotor position and gamma, a third test was conducted to examine the response of the machine to increasing currents. The thesis supervisor in [26] used specific operating points provided by the industry partner and this thesis sought out from the start of these basic tests to provide a more overall understanding of the machine's operation.

The methodology of this test was that gamma was set at its maximum torque value $\gamma = 40^{\circ}_{E}$ and then the line current $I_{LINE,MAX}$ was varied in increments of 50A from 100A until 400A (86.6A to 346.41A $I_{S,RMS}$). The value of gamma was chosen because it was the maximum torque value and a representation of running the machine in the flux weakening regime, which best utilizes a machine with high saliency such as this one and therefore is the most important to investigate. This thesis will also show later that the Maximum Torque per Ampere (MTPA) operation region with respect to gamma is centered around $\gamma = 40^{\circ}_{E}$, and because this region is used during the maximum torque section of the machine power curve at low speeds, operating points beginning at this gamma are particularly important.

2.2.3.1 Saturation Effects versus Rotor Position and Current

This simulation was run differently than the previous simulations, the results only cover two slots, 60°_{E} and consist of 30 samples taken every 2°_{E} as before, this change was done as many currents were going to be used and machine response provides no new information after two slots, as the model and currents are ideal. These results were also post-processed in a similar manner as the previous tests.

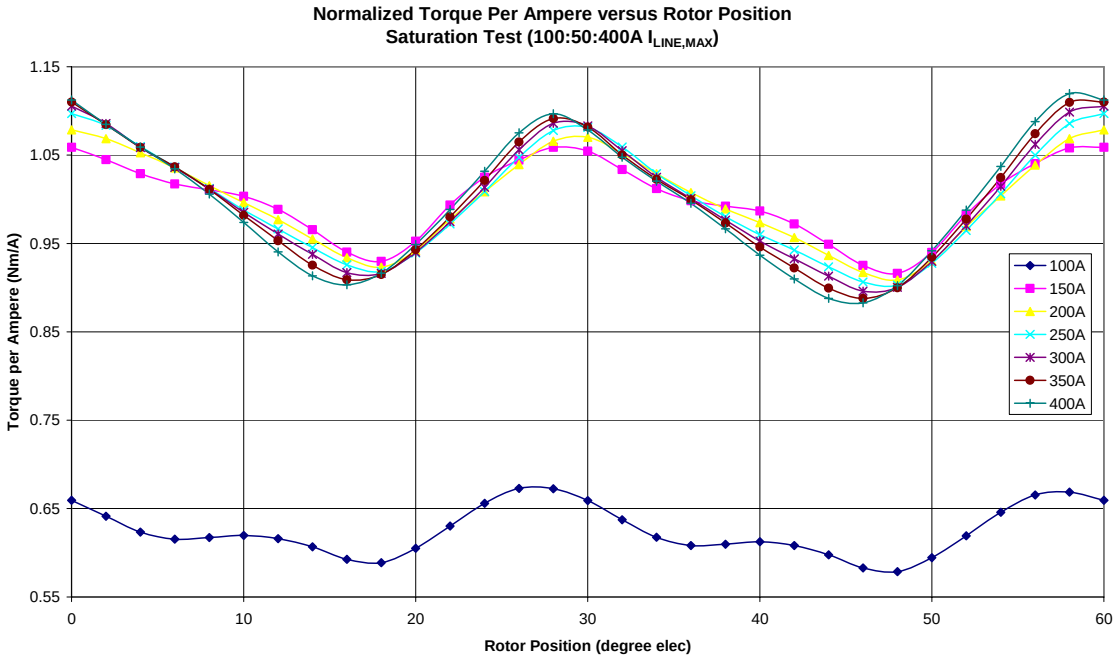

Figure 2.9 Normalized Torque per Ampere versus Rotor Position

Initially the torque curves from the test were examined, the most clear result was that the waveforms began to show a phase shift of the maximum torque peaks at 300A $I_{LINE,MAX}$ (259.81A $I_{S,RMS}$). Figure 2.9 shows this effect and was the first sign of saturation of the machine. It is interesting to note that the local maximum peak which was noted in the previous section of having reduced flux had a phase shift first, as the weaker flux was more susceptible to saturation effects. Having those results to show where the machine

began to saturate and some general information, the data was further analyzed to determine exactly where and what effects saturation was having. The second clear result was that the Normalized Torque per Ampere for a wide range of line currents was very similar in shape and magnitude. How these waveforms were determined is that the mean torque of each operating point was taken over 60°_{E} and then the resultant torque versus rotor position was scaled by the mean value. The only notable outlier in the data set was the result at 100A $I_{LINE,MAX}$, this is because the machine is not magnetically charged at that line current level and therefore does not behave as linearly as the currents above it.

To understand what effects saturation had on the torque output of the machine, the scaled simulation results for the entire machine were classified as shown in Table 2.2 on the following page. Each operating point was investigated for the following parameters: Maximum Torque, Minimum Torque, Average Torque, Maximum minus Average Torque, Average minus Minimum Torque, Average Torque per Ampere, Maximum Torque per Ampere, Minimum Torque per Ampere, Relative Change in Average, Maximum and Minimum Torques per Ampere with regards to the previous operating point. Table 2.2 displays the results of the saturation test and shows that at 300A $I_{LINE,MAX}$ the torque response begins to show machine saturation. The reader knows that the machine has entered saturation because the change in Minimum Torque per Ampere is negative for the first time. Following operating points higher into the saturation region reflect a similar pattern across the entire waveform, as is seen in the relative changes of the 350 and 400A operating points. This data allowed for the understanding of what was happening both with the saturation of the iron and point where flux permeability became limited as well as the effects of saturation on the shape of the torque waveform. The difference values of maximum, minimum and average torques, displayed on rows 5 and 6 of Table 2.2 show how the shape of the waveform changed with saturation. As the machine was in the middle of the linear magnetization region, the waveform itself became more balanced as the machine was run within the linear region of magnetism; this is certainly no surprise but is interesting to note. The

availability of the data showing the composition above and below the average torque line shows that below saturation the average torque line resides much nearer to the top of the waveform, suggesting that the upper part has wider peaks and therefore a larger integral. As the machine approaches saturation the width of the peaks and therefore the integral of the torque above and below the average torque line becomes more equal, reaching its most equal value at saturation. Following saturation the average torque line moves lower on the total waveform, suggesting that the area under the average torque line or the minimum peak widths are becoming wider, this trend continues deep into saturation and becomes more pronounced as the machine continues into saturation.

Table 2.2 Torque Response of the Saturation Test

Line Current	100	150	200	250	300	350	400
Max T	88.912	139.905	195.417	251.199	304.146	354.267	403.389
Min T	76.483	121.059	164.664	206.775	246.6	283.356	318.096
Avg T	82.622	132.136	181.165	228.997	275.161	319.124	360.302
Max T - Avg T	6.29	7.769	14.252	22.202	28.985	35.143	43.087
Avg T - Min T	6.139	11.077	16.501	22.222	28.561	35.768	42.206
Avg T per Amp	0.826	0.881	0.906	0.916	0.917	0.912	0.901
Max T per Amp	0.889	0.933	0.977	1.005	1.014	1.012	1.008
Min T per Amp	0.765	0.807	0.823	0.827	0.822	0.81	0.795
Increase AvgTperAmp	NA	0.055	0.025	0.01	0.001	-0.005	-0.011
Increase MaxTperAmp	NA	0.044	0.044	0.028	0.009	-0.002	-0.004
IncreaseMinTperAmp	NA	0.042	0.016	0.004	-0.005	-0.012	-0.014

2.2.3.2 Machine Saturation $I_{LINE,MAX}$ Values

The next question one might ask is, “how can you be so certain those values mean the machine is in saturation?” Clearly, if the machine can no longer produce the same amount of torque for a given per unit current input, this would indicate a loss of performance, meaning that the proportional nature of line current to average torque no longer exists. However, in order to more further verify the results and to investigate an

interesting effect in the machine, more tests were conducted to determine the points of machine saturation.

The first test was to look at the results for a large number of operating points with one gamma and determine how the average torque output was affected. Figure 2.10 below shows that, with $\gamma = 0^{\circ}_{E}$, three clear regions of average torque linearity exist with respect to line current. Below 155A $I_{LINE,MAX}$ (134.23A $I_{S,RMS}$), the iron is charging, or lining up with the applied H field and is in Region I of the steel magnetization curve. After this value, the machine torque and radial force behaves relatively linearly within bounds, which is shown in the middle red portion of Figure 2.10, until the point of saturation, defining Region II or the linear magnetic region. The final region, Region III or saturation, occurs at approximately 360A $I_{LINE,MAX}$ (311.77A $I_{S,RMS}$).

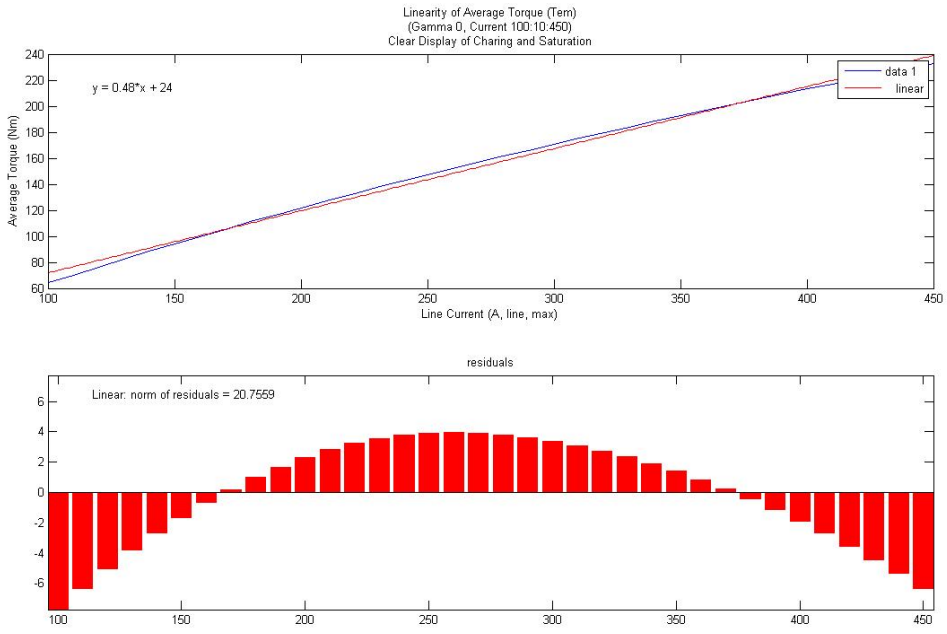

Figure 2.10 Linearity of Average Torque versus Line Current for $\gamma = 0^{\circ}_{E}$

It is also important to note that these regions shift with gamma and that the linear region shifts to higher currents as gamma is increased, this is of course because as gamma is increased it takes higher line currents to produce the same $I_{S,RMS}$. The most linear force and torque operation of the machine, meaning that there is the greatest bounded region of response is at $\gamma = 70^{\circ}_{E}$. This was discovered by analyzing the linearity of the average torque produced versus the line currents for each gamma investigated and then using the basic fit function in MATLAB in order to fit a linear curve, plot the residuals and show the norm of the residuals. The norm of the residuals of fitting the torque response versus the input line current would show how linearly proportional torque response actually was for a particular gamma. The author believes that this is a useful result because most literature on machine control makes the fundamental assumption that they are dealing with a magnetically linear machine in order to simplify the mathematical model. The fact that a "k" value which is a function of the load angle can be derived for a machine which could adjust for magnetic non-linearities is at least useful to demonstrate. Figure 2.11 on the next page demonstrates the wider band of bounded line currents within the linear magnetic region due to field weakening. The result is given at $\gamma = 70^{\circ}_{E}$, which as previously stated, is the gamma which the torque response is most linear. On the following page, Figure 2.12 shows the relative linearity versus gamma and provides evidence that $\gamma = 70^{\circ}_{E}$ is the most linear operating point, with respect to torque response.

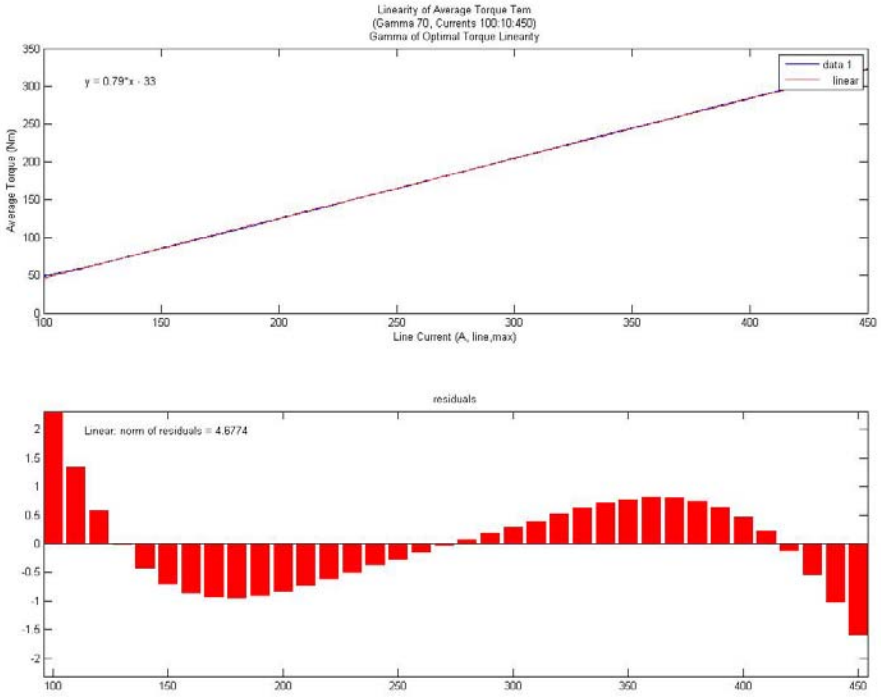

Figure 2.11 Linearity of Average Torque versus Line Current for $\gamma = 70^{\circ}_{E}$

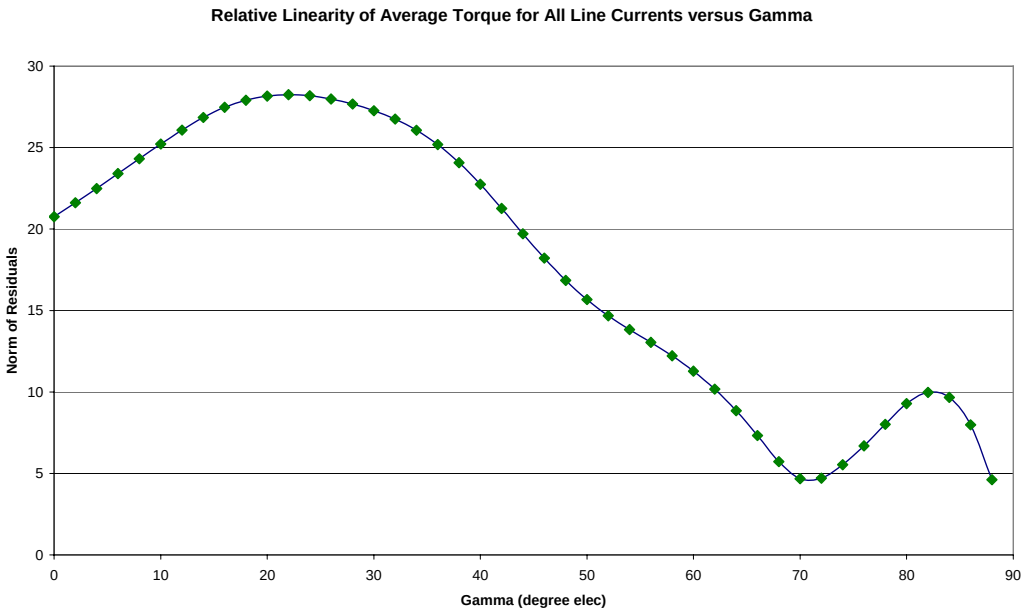

Figure 2.12 Relative Linearity of the Machine for Line Currents versus Gamma

The author believes that it is at $\gamma = 70^{\circ}_{E}$ that the electrodynamic torque and reluctance torque are in equilibrium and therefore an increase in line current increases both torque components equally and thus a very linear response occurs. This observation is supported by Figure 2.3, which shows the behavior of the torque components with respect to gamma. The point of $\gamma = 70^{\circ}_{E}$ appears later in Chapter IV as a peculiar "notch" in the spectrums of torque and force operating points. Figure 2.13 below is the representation of average torque for the 1656 operating points investigated in this thesis. A 3D table was made in order to parameterize Torque and Force components by (γ,Θ,I), (load angle, rotor position and line current or secant current).

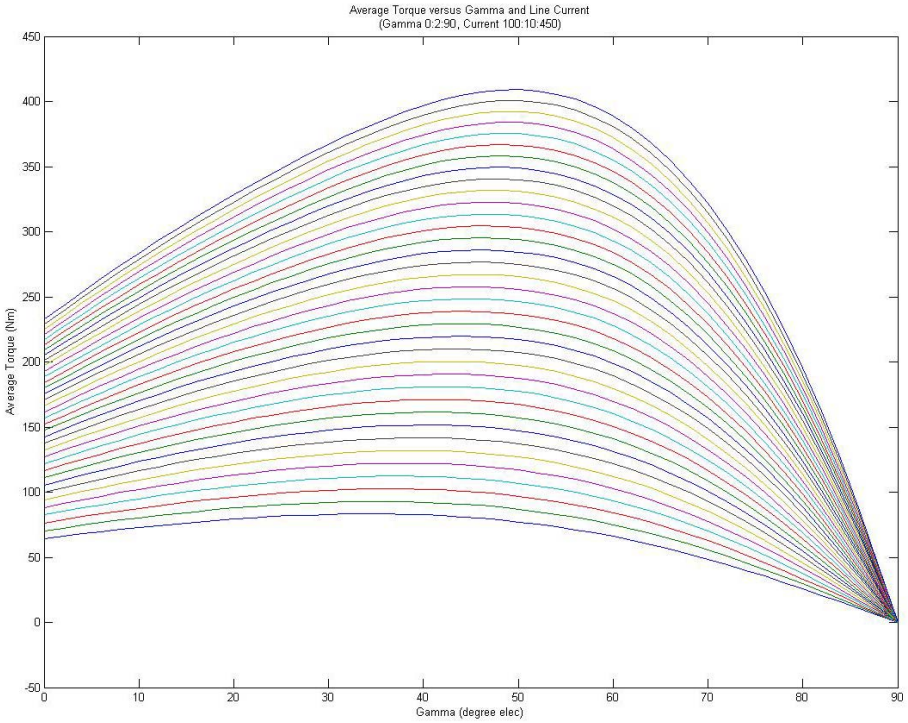

Figure 2.13 Average Torque versus Gamma and Line Currents

Figure 2.13 was the data set used in order to establish the torque linearities based on gamma as discussed in this sub-section and displayed in Figures 2.10, 2.11 and 2.12.

The last method used to establish saturation was to look at the B fields and flux lines within the ANSYS model itself. Using the previous linearity study to establish the expected line current values for charging current, or necessary H field strength in Amperes/meter to force the machine to behave regularly, the following flux density figures were created. Figure 2.14 below shows the 160A $I_{LINE,MAX}$,$\gamma = 0^{\circ}_{E}$ operating point and the model's flux density, with a flux line overlay added to demonstrate the primary flux paths through the rotor and stator. The figure shows that, while some points of the back-iron are near saturation, and the main flux return path is in saturation, there is limited arcing of flux and there are other flux paths that the stator flux may take through teeth which are unsaturated.

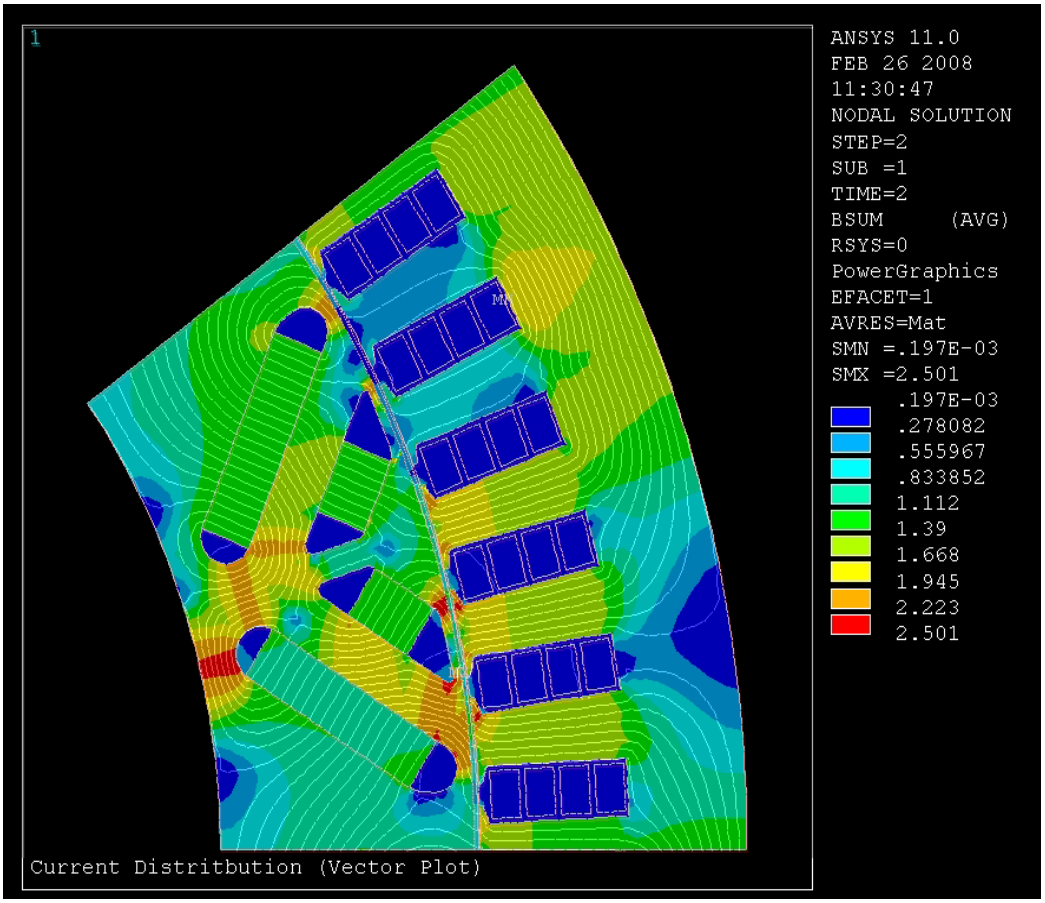

Figure 2.14 Model Flux Density (B) and Flux Lines at 160A $I_{LINE,MAX}$ (138.56A $I_{S,RMS}$)

Figure 2.15 below shows the 360A $I_{LINE,MAX},\gamma = 0^{\circ}_{E}$ operating point. The observer should note that the flux paths are almost the same, however the saturation of the flux paths are greatly increased. At this operating point, which represents the region where the machine shows saturation effects, one can see that both of the main flux paths through the back-iron are now saturated, one of which is near the maximum flux density for the material at over 2T. Furthermore, all of the teeth which serve as the main flux paths are now heavily saturated, which has forced flux to find a path of more permeance through less saturated teeth and even increased arcing through the air. Typically such fringe effects are either neglected by calculations or rolled into a "k" value in order to compensate for many non-linearities with a coefficient, [10] particularly enjoys creating empirically based coefficients.

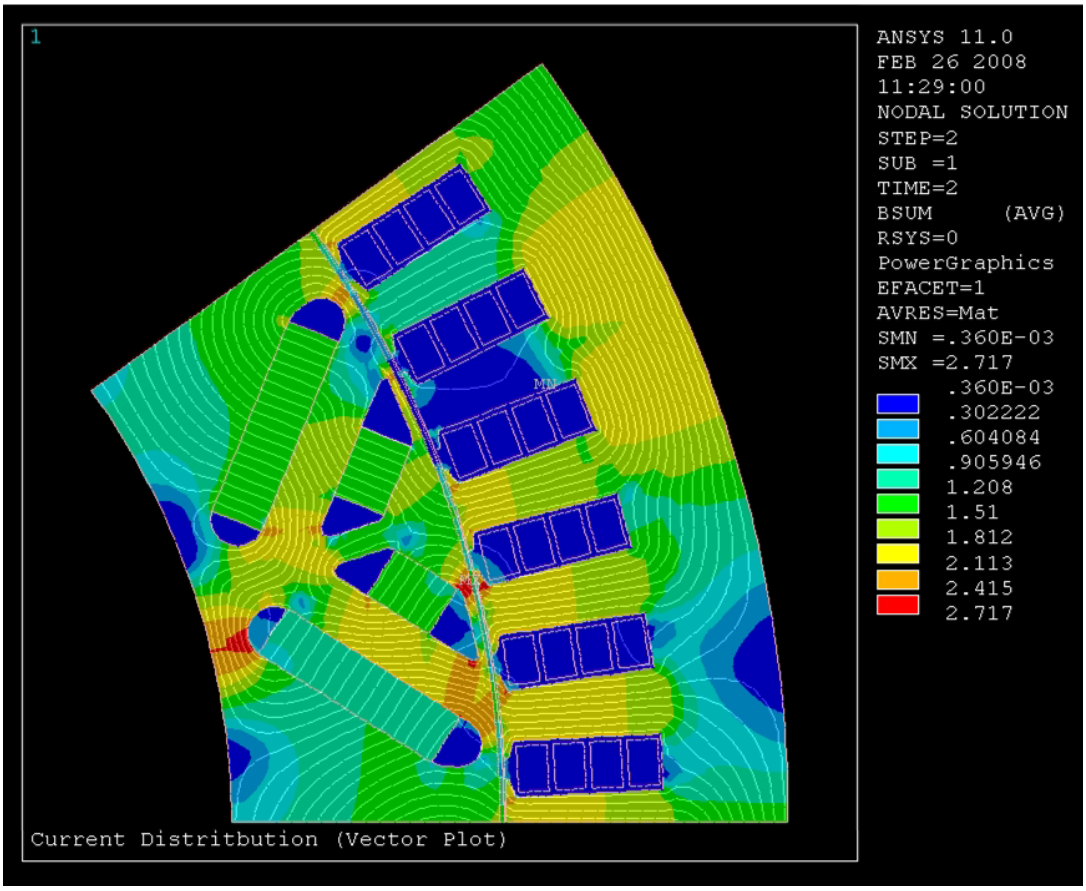

Figure 2.15 Model Flux Density (B) and Flux Lines at 360A $I_{LINE,MAX}$ (311.77A $I_{S,RMS}$)

2.2.3.3 Saturation Effects on Magnet Flux Linkage (λ_D^M)

Later a more precise data set was run where current intervals of 10A $I_{LINE,MAX}$ from 100A to 450A and this data was used to calculate magnet flux linkage. Using T_{EM} which is in d-q space for the simulations where $\gamma = 0_E^\circ$ and thereby knowing I_Q, one can isolate magnet flux linkage λ_D^M. Figure 2.16 shows that as line current increases, magnet flux linkage decreases, this phenomena was shown to a senior member of the drives group at ISEA who could not explain this, the author initially believed that it had something to do with "flux linkage resistance" or decreased permeance due to saturation and this was the case. In the Doktorarbeit by Dajaku [25], he shows that this decrease of magnet flux linkage in the d-axis direction is not a magnitude change, but rather the d and q axes themselves deflect due to the decreased permeance of the stator iron in the saturation

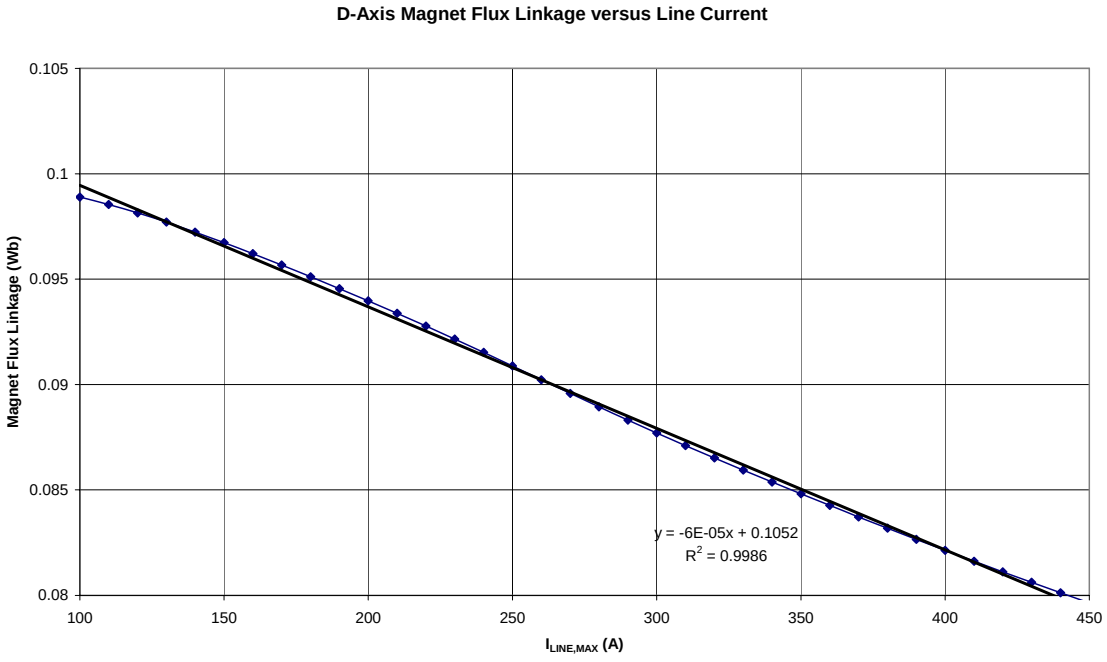

Figure 2.16 d-Axis Magnet Flux Linkage versus Peak Line Current

region. Typically one assumes that there is no q-axis magnetic flux linkage, but Dajaku showed that λ_Q^M can reach 24% of λ_D^M due to the deflection of the initial d and q axes. In the previous section, a torque peak phase shift was noted as the line current increased into saturation, this torque peak phase shift is directly related to the axes shifting and therefore having mutual d-q space inductances as well as q-axis magnet flux. This phenomenon was demonstrated to exist and quantified, but what causes it?

To understand that one must go back to Hopkinson's Law:

$$\Re = \frac{\Im}{\Phi} \tag{2.15}$$

Reluctance ($\Re$) is the result of the division of mmF (magnetomotive force) and coil flux. If one substitutes reluctance as follows:

$$\Re = \frac{l}{\mu_0 \mu_r A} \tag{2.16}$$

So that, reluctance is the result of magnetic path length over the permeability product by the cross sectional area and one knows:

$$Permeance = \frac{1}{\Re} \tag{2.17}$$

As sections of the machine saturate their permeability decrease, because permeability is the inverse of reluctance, a decrease in permeance means an increase in reluctance and therefore the potential for an increase in magnetic path length, with all other variables the same. Magnetic flux operates much like current and that is why Hopkinson's Law is compared to Ohm's law, because flux finds the path of least reluctance, and as it finds the path of least reluctance in a saturated machine, the d and q rotor axes deflect to

reflect this magnet flux path shift. Also, [25] showed that gamma can further deflect the d and q flux linkages by 20% with the same current, however as all saturation effects; this is most pronounced in high current regions as was evident in Figure 2.15, where numerous flux lines arced and found alternate paths of less reluctance.

2.2.4 Using Magnet Flux Linkage (λ_D^M) to Calculate L_D and L_Q

The primary goal at the beginning of this chapter was to discover machine operating behavior and design parameters. From the analysis of operating behavior and discovery of λ_D^M the d and q inductances may be discovered. As one might remember from earlier in the chapter, if one has the average torque over one electrical period and then transforms the phase and time values into the d-q domain by the Park Transform, then he has the ability to solve the following equation:

$$T_{EM} = (\frac{P}{2})(\frac{3}{2})(\lambda_D^M I_Q + (L_D - L_Q) I_D I_Q) \tag{2.13}$$

Due to a significant portion of this chapter concentrating on current response versus average torque, it is safe to say that those two parameters are known, as well as P, which was revealed to be 10, in Table 2.1. Utilizing what was discovered in the last section, that one with some degree of error may predict magnet flux linkage, the d-q space torque equation may be solved for a gamma value other than 0 and this will result in a difference in d and q inductances, one may then discover those inductances. This is because, while these values are constants in the d-q domain versus rotor position, they are not constants versus load angle. By varying gamma and using the response of the inductance difference, the maximum difference is when $\gamma = 0^{\circ}_E$ and the result is entirely q-axis inductance and then the value when $\gamma = 90^{\circ}_E$ is the minimum and the result is entirely d-axis inductance. This process described in [22],[25] allowed for the calculation of L_D = 0.89mH and L_Q = 1.97mH, resulting in a saliency ratio of 2.2, all

values which are reasonable and fulfill the mission of this chapter. The following chapter will discuss noise in electric machines and then its causes in order to lead in the main results chapter, Chapter IV, which explores reducing noise in this electric machine and goes more into detail over a few topics which have already been mentioned, but whose subject matter belongs with the acoustic work.

CHAPTER III
NOISE OF AN ELECTROMECHANICAL ORIGIN IN ELECTRIC MACHINES

In a literature study of the source of funding and therefore interest in electric machine acoustic research, recent research has emanated from the automotive and naval warfare sectors. Both of these markets have clear reasons for this research, naval warfare uses electric machines on submarines for propulsion and both space utilization and stealth are critical features of these crafts. The automotive sector is embracing high efficiency electric machines, such as PMSMs, to replace belt driven and hydraulic accessories, which add loads to the ICE and are less efficient than their electrical counterparts. Also of course larger electric machines are being utilized as both the primary propulsion system in electric vehicles, such as fuel cell vehicles, and as a complimentary propulsion source in the many varieties of hybrid vehicles.

The present market for hybrid vehicles being pursued by many hybrid manufacturers is the luxury segment, this is logical as the consumer in this market already is willing to pay a premium for performance. In this segment two of the major manufacturers are Bayerisch Motoren Werke AG (BWM) and Daimler AG under their Mercedes-Benz brand, whose brands depend on the high quality and seamless integration of any new technology adopted by their respective product lines. Due to the luxury aspect of this market segment, the consumer expects a level of performance as well as reduced noise from the automobile and environment outside of the vehicle during driving. This expectation creates research in the area of electrical machine acoustics that did not exist when these electrical machines were confined to industrial settings where noise is more acceptable.

A research group that has done significant work in the area of electric machine acoustics is the Electrical Machines and Drives group at the University of Sheffield in England. Many other studies have started their acoustic analysis of PMSMs based on a model

developed by Dr. Zhu of the aforementioned group. The problem with this mathematical model is that it assumes a stator without slot openings to increase ease of calculation and modeling, the issue with this is that, as will be described more in detail later, the slot openings are a fundamental component of acoustics in electrical machines and therefore cannot be excluded from any model which hopes to analyze acoustics. When I learned this I thought about a quote from Nikola Tesla in 1934, "Today's scientists have substituted mathematics for experiments and they wander off through equation and equation and eventually build a structure which has no relation to reality." For examining machine acoustics a mathematical model without slot openings is a collection of equations which does not achieve what it was intended to do. If a heavily referenced model does not reflect reality, where do you start examining machine noise?

3.1 What Is Noise and Where Does It Come From?

Let us begin at the start, what is noise and where does it come from? One must be able to answer this question before he may seek the answer. In *Noise and Vibration of Electrical Machines*, Timar writes that noise is an "audible sound or mixture of sounds which may have an unpleasant effect on human beings, disturbs the concentration and does not convey any useful information." This definition implies that noise is an unwanted parasitic side-effect of electric machines, much like losses due to various factors including eddy currents, end winding flux leakage and ohmic heating of windings. In research for this thesis it was easy to find references relating to the design of a machine regarding efficiency, power density, cost or thermal losses [10],[22],[25]; however acoustic design is often not the primary machine design focus as the primary function of the machine is to convert electrical energy to mechanical energy and the previously mentioned factors involve cost and form, which is a premium in many applications. Due to acoustic performance not being a primary factor in the design stage of a machine, such studies as this one must be conducted at a later date in order to improve a machine after many parameters are set in the design process. The PMSM

studied in this thesis is planned to be produced in the near future, so the implementation strategy of any solution must be done in such a way that the machine itself is not changed.

The second question posed above is "Where does it come from?" There are numerous sources of acoustic noise in vehicles, in [20],[26] these sources are discussed more heavily. However, for the electric machine itself there remains a few sources of noise such as: bearing noise, inverter switching, aerodynamic noise and of course housing and stator noise due to electromagnetic forces in the air gap of the machine. This thesis only considers electromagnetic forces on the stator itself and their effect on machine acoustics, for a more complete structural study on this machine; including the housing please refer to [26].

Noise of an electromagnetic origin in an electric machine has one source; it is the radial force fundamental and its harmonics. The harmonics of radial force is called its ripple and is analogous to torque ripple. Torque ripple causes load acoustics and vibrations, which are undesirable and have been heavily studied in PMSM due to their previous primary use in precision machining industrial applications. Harmonics result from any waveform which is comprised of any frequency other than the fundamental frequency. The idea of harmonics originated from acoustics, where a string vibrated at a frequency that was a multiple of the base frequency desired. In the case of electric machines there are many harmonics which interest the designer and developer, torque and force harmonics which result from non-homogenous flux paths though both the rotor and stator and therefore an imperfect distribution of flux, resulting in a non-ideal matching of the current fundamental and back EMF waveforms. Figures 3.1, 3.2 and Equation 3.1 on the following page demonstrate how the Fourier harmonics of the electromagnetic forces from the electromagnetic system are passed through to the mechanical system and therefore cause mechanical displacements of the stator and stator housing which results in acoustic noise. This imperfect distribution of air gap flux can also occur if the

machine is idealized to have sinusoidally distributed stator windings (in the case of the PMSM) and then these windings are fed with purely sinusoidal currents, when in fact the machine does not have perfectly sinusoidally distributed windings, as that never occurs.

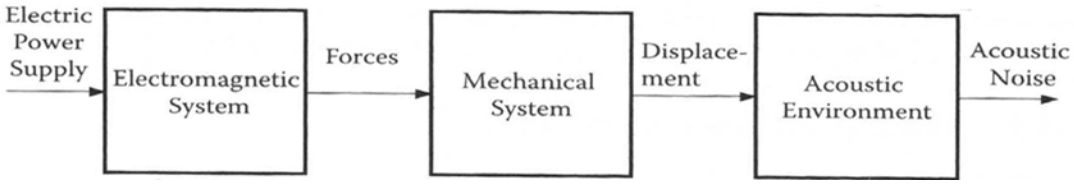

Figure 3.1 Block Diagram of Electric Machine Noise Generation

$$T_{EM} = T_L + J\frac{d\omega_R}{dt} + B\omega_R \tag{3.1}$$

Thus in order to avoid harmonics in the torque and force waveforms produced by the interaction of the current fundamental and back EMF harmonics (which results as a differentiation of the air gap flux harmonics versus time), one must alter the current harmonics in order to produce different air gap flux harmonics which interact with the current fundamental in a way that reduces the torque or force harmonics as desired. In [26], it was shown that this problem is overdetermined and that one must choose what initial parameters they also wish to maximize the solution for, furthermore the same work demonstrated that reducing force or torque harmonics and therefore ripple are not independent.

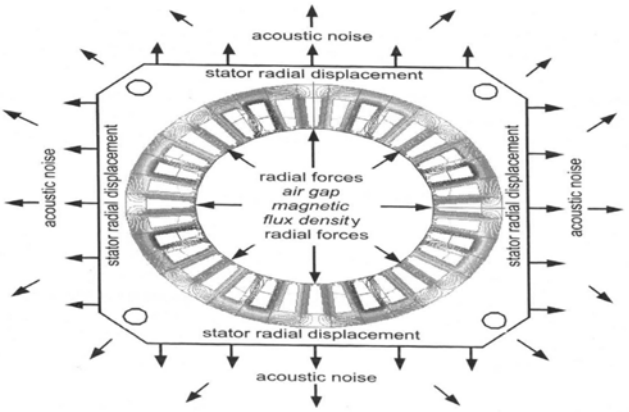

Figure 3.2 Representation of Figure 3.1 as an Electric Machine [27]

3.2 How to Reduce Machine Noise

There are many mechanical (physical) ways to reduce acoustic noise in PMSMs which are well understood by researchers. In [27], Gieras discusses numerous ways of reducing torque and force ripple including: magnet magnetization direction, segmented magnets, skewed magnets, shifted magnets, proper stator slot number, specially shaped slots, skewed slots, dummy slots, fractional pitch windings and adjusted tooth shoe shape. All of these mechanical methods have been employed to various degrees of success, but manufacturing each solution to the precision required by the machine is often costly and problematic. Control solutions for machine noise however are often much more cost effective and can be implemented once a machine has been prototyped and its design parameters are fixed, such as the case with the machine used to support this thesis. Control solutions are often implementable purely as software add-ons or require minimal hardware such as a more precise encoder for spatial resolution, or sensors for line parameters.

3.3 What To Look for in Acoustics

When inspecting the results of acoustic simulations or measurements of an electric machines there are a few particular things that are very important. The first of these is the mode of stator deflection that is primary to the cause of the noise. Deflection modes mean that a certain type of deformation of that stator such as a “breathing” representing mode 0 or higher order modes such as 1, which is due to eccentricities, or 2 which cause “bending” of the stator. These modes are determined by radial sound pressure level (SPL) measurement to determine the homogeneity of the stator deflection, if the primary acoustic SPL is homogeneous, then the primary mode is 0. If one side dominates the SPL measurement, this represents a mode 1 eccentricity effect and if two sides dominate over two others; this would suggest the bending mode 2. For a more full explanation of stator deflection modes [26] and [27] are excellent sources of this topic. In the particular

study presented in this thesis, it was determined by [26] that a mode 0 investigation of the stator was sufficient to explain the acoustic spectrum seen in Chapter IV.

Once the mode is determined the second effect to consider is the radial force harmonics, similarly to the way that power quality is analyzed. In acoustics it proves to be more beneficial to analyze the space harmonics of the radial forces from the waveforms of the time invariant waveforms in d-q space. In power quality analysis odd space harmonics are the prevalent harmonics in a balanced system fed by three-phase currents and manifest themselves as a symmetric addition to the fundamental of the investigated waveform, be that force, torque, or current. Even harmonics however suggest that there suggest that there is an imbalance or asymmetry in the source of the waveform, in the case of electric machines, large even harmonics would suggest eccentricity, material consistency issues, or an imbalance the air gap flux. Transferring this over to radial force space harmonics the opposite is true, even harmonics are the dominating harmonics as they are the product of even time current harmonics and odd space harmonics represent asymmetries in the stator construction or flux waveforms that cause machine noise.

In the next chapter, these fundamental aspects of machine acoustics will be applied to a specific machine, then used to explain its acoustic performance, and finally utilized to create a control strategy in order to minimize the radial force ripple and therefore noise that the machine produces.

CHAPTER IV
INVESTIGATION AND DEVELOPMENT OF A SOLUTION FOR ACOUSTIC ISSUES IN A PARTICULAR MACHINE

ISEA was initially provided waveform files to provide data as to the acoustic behavior of the machine as well as Figure 4.1 below. This figure demonstrates the sound pressure level (SPL) in decibels (dB) at certain frequencies as a function of machine mechanical rotor speed.

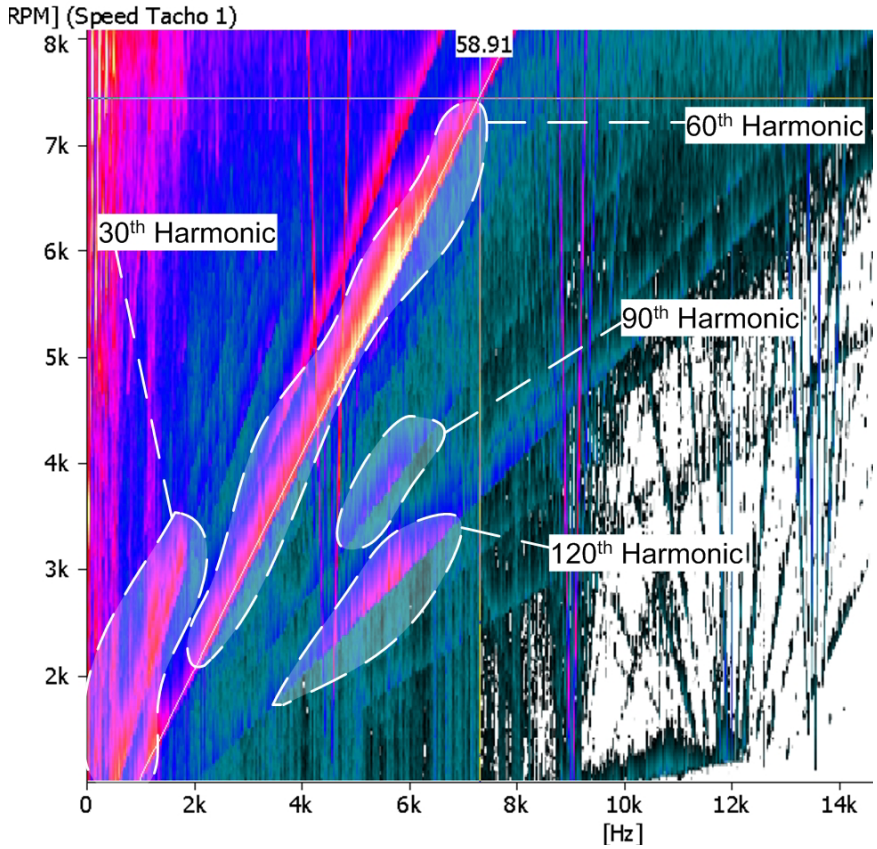

Figure 4.1 Provided Spectrograph with Critical Areas Circled

Clearly by the above figure, the most important frequency to investigate is the 60th mechanical radial force harmonic (shown in Figure 4.1 as 58.91 by a crude oscilloscope cursor estimation) or 12th electrical force harmonic as the previous definition of

$p \times f_{MECH} = f_{ELEC}$ or in this case, the mechanical frequency is five times lower than the electrical frequency and therefore the number of the corresponding harmonic is higher. The second observation after the fact that the 60th mechanical force harmonic is much higher is that the 30th mechanical force harmonic disappears shortly after 3000 RPM; this would suggest that this harmonic is based on the magnitude of the current in the speed range below rated speed and decreases greatly once the machine enters the constant power region or that the machine is operated as shown in the Section 4.1.

4.1 Operation Estimation from Machine Parameters and Control Research

In Figure 4.3 on page 51, the machine parameters from Table 2.1 are used to create a maximum power curve and then based on the provided control data, as well as research in the topic from [28],[29],[30],[31], a reasonable estimation of control strategy and machine performance is given in order to compare with the acoustic response shown in Figure 4.1. The most noticeable difference in the control strategy that was used to produce Figure 4.1 is that below the rated speed of the machine the control strategy employed is the Maximum Torque per Ampere (MTPA) approach, where the field is weakened before the rated speed due to optimal MTPA operation between $\gamma = 34^{\circ}_{E} \rightarrow 46^{\circ}_{E}$, demonstrated by Figure 4.2 on the next page.

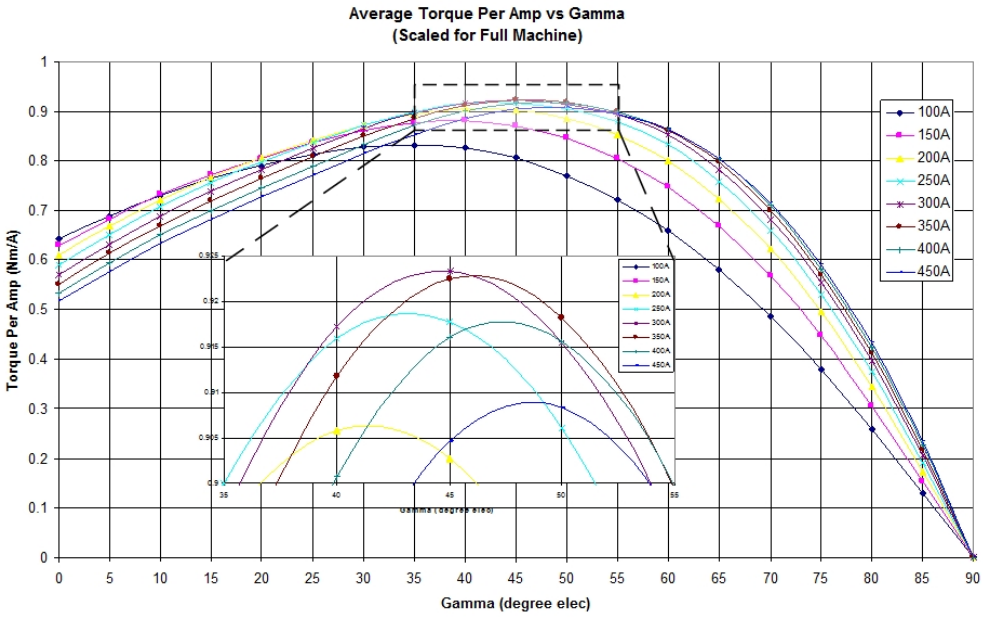

Figure 4.2 Average Torque per Ampere versus Gamma with Maximum Region Zoomed

A traditional approach, in the area below rated speed, would be to operate at $\gamma = 0^{\circ}_{E}$ and then adjust I_Q in order to fulfill the torque command T^*. This operation would continue until ω_R (rated speed), at which time the field must be weakened due to reaching the maximum power point at rated speed and torque. The next operation region shown in Figure 4.3 is the constant secant current region. This region begins when $\gamma = 46^{\circ}_{E}$ for maximum rms secant current $I_{S,RMS,MAX}$, as the inverter either cannot produce more current than 300A $I_{S,RMS}$, or this is the thermal limit of the machine windings, the true limit of secant current was never provided and this value is only an assumption due to it was often the maximum value given in the machine operation tables provided by the industry partner. In [22] Krause states that electric machines are designed to operate slightly within the saturation region. If this is the case there is key information missing from the industry partner about the operation limits of this machine. Based on the results of Chapter III, this machine does not display performance saturation effects until 311.77A $I_{S,RMS}$, 11A higher than the maximum values given in the provided operation tables.

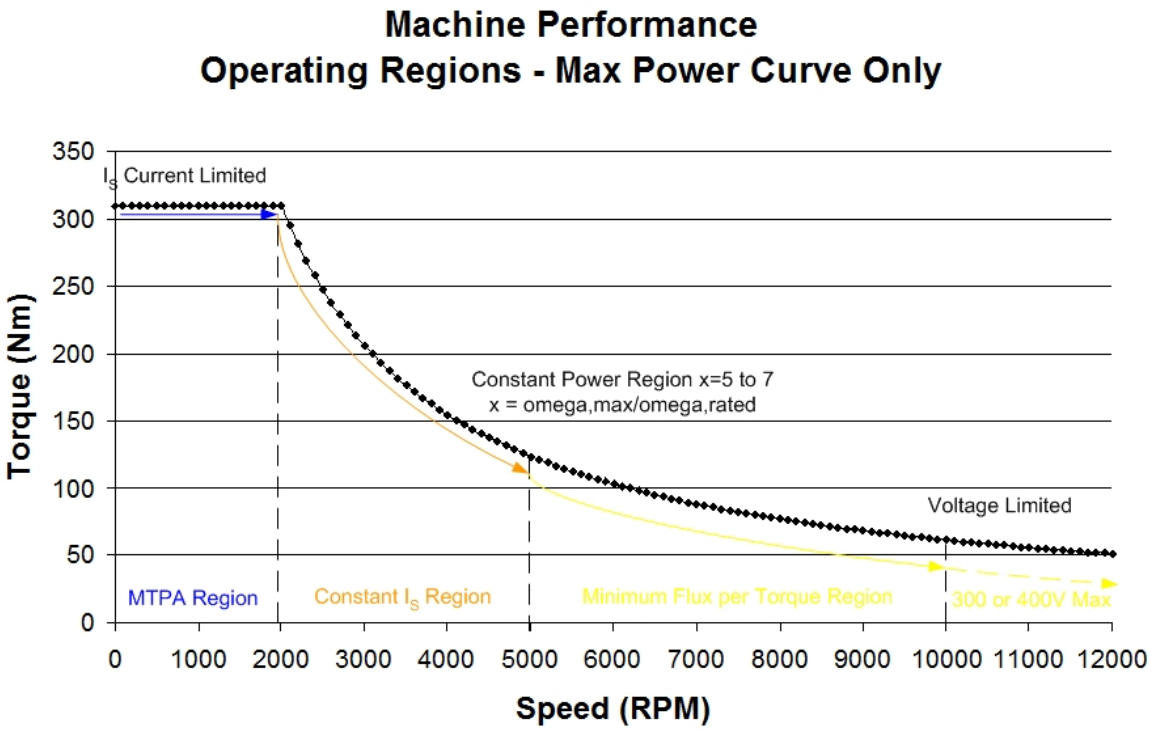

Figure 4.3 Estimation of the Control Strategy and Machine Performance

The third area of machine operation identified by other research conducted by the industry partner is the Minimum Flux per Torque Region (MFPT). This region is the third subsection of the constant power region and occurs along the line where the available torque curve is tangent to the secant voltage (V_S) ellipse in d-q space. As the operation speed increases in a machine, the voltage ellipse in d-q space centered on $\left(-\frac{\lambda_D^M}{L_D},0\right)$ collapses to smaller and smaller ellipses, until there is no more voltage ellipse and therefore no secant current vector. Following the point where the total maximum torque curve versus gamma is tangent to the voltage ellipse as it collapses with increasing machine speed, it creates the MFPT curve, which is plotted with the other two operation regions mentioned before, in Figure 4.4 below.

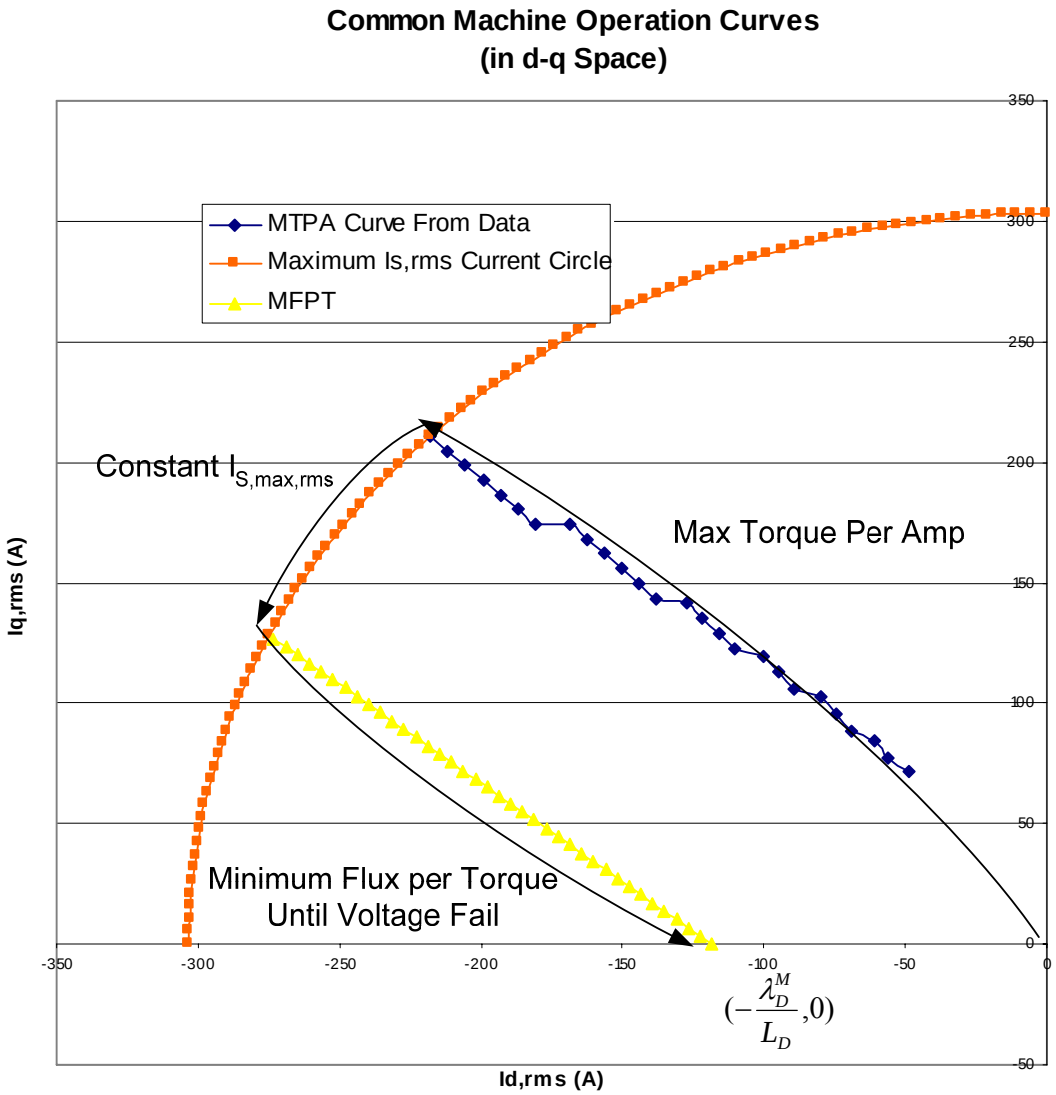

Figure 4.4 Three Regions of Machine Operation Represented by d-q Currents

4.2 Radial Force Investigation with Purely Sinusoidal Currents

4.2.1 Radial Force versus Rotor Position (Corollary to Subheading 2.2.2)

The first logical step to analyze radial forces was conducted in conjunction with the torque analysis in Chapter II. In the case of the force simulation, the procedure in ANSYS was done at the same time as the torque simulations due to the thesis supervisor

creating a simulation control macro which invoked both the TORQSUM and FMAGSUM macros which are part of the base ANSYS package. The text output provided by these macros were read into MATLAB with an m-file and then into Excel if data manipulation was more useful. In the case of this chapter, often the more powerful engineering mathematics of MATLAB was necessary and much more of the work was done there.

Below is Figure 4.5 which shows the total and radial force versus rotor position for the 170A $I_{LINE,MAX}$ (147.22 $I_{S,RMS}$), $\gamma = 34^{\circ}_{E}$ operating point, as was used in Chapter II.

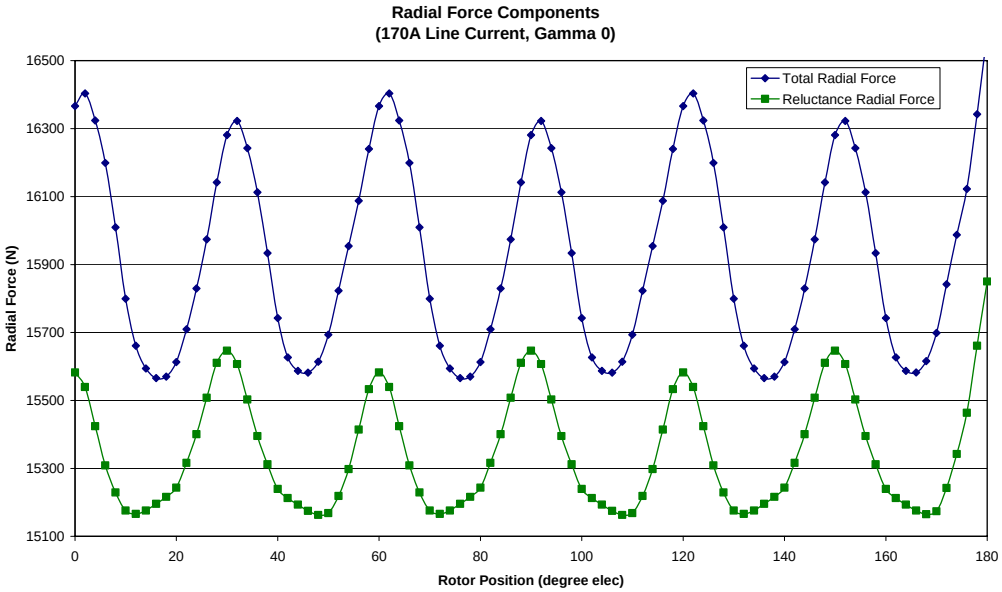

Figure 4.5 Total and Reluctance Radial Force versus Rotor Position

Something that will begin in this section is that each time a key waveform is given it will be accompanied by its corresponding harmonic spectrum in order to better understand the actual composition of the waveform and what magnetic origins there are for machine noise. Figures 4.6 and 4.7 below represent the spectrums of the two waveforms in Figure 4.5 above; the key result is that the harmonics are almost identical.

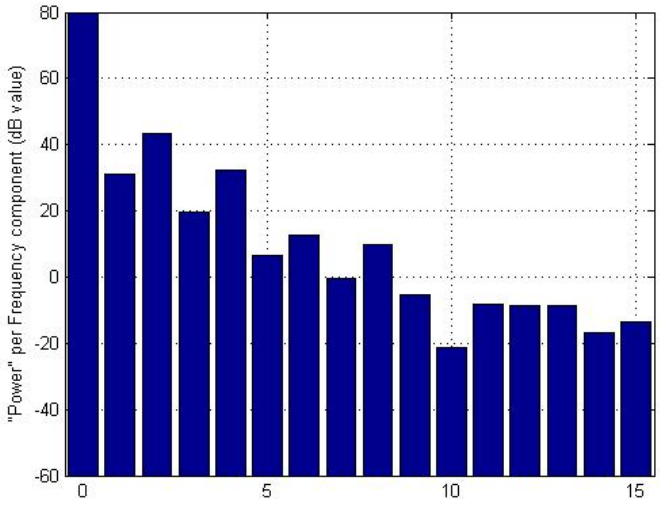

Figure 4.6 Total Radial Force Harmonic Spectrum

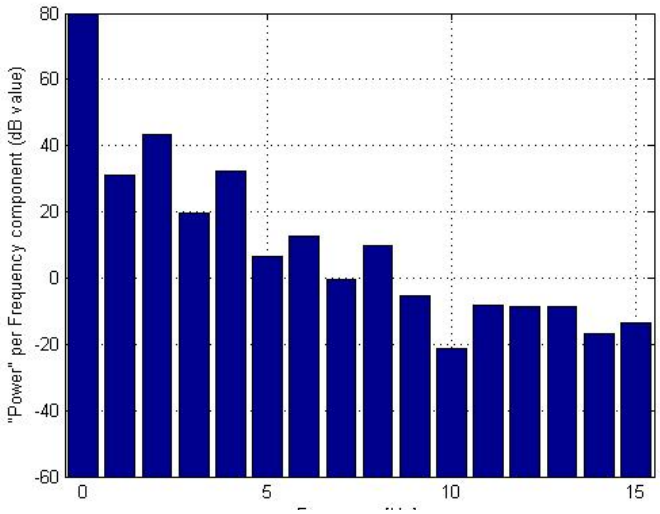

Figure 4.7 Reluctance Radial Force Harmonic Spectrum

One might notice that unlike Figure 2.6, Figure 4.5 is missing both cogging and electrodynamic radial force, this is due to the fact that that cogging radial force is 1/3 the magnitude of either reluctance or total radial force, therefore it does not make sense to show it on the same axis as the scale difference would preclude any details being shown, it is included separately in Figure 4.8 below. Furthermore, the radial force ripple due to cogging radial force is very small when compared to the other radial force ripple

components from electrodynamic and reluctance sources. The spectrum of the cogging radial force waveform, Figure 4.9, shows that very few of the harmonics which exist are above 0dB, whereas the total radial force harmonic components are often over 50dB, as will be seen later in the chapter.

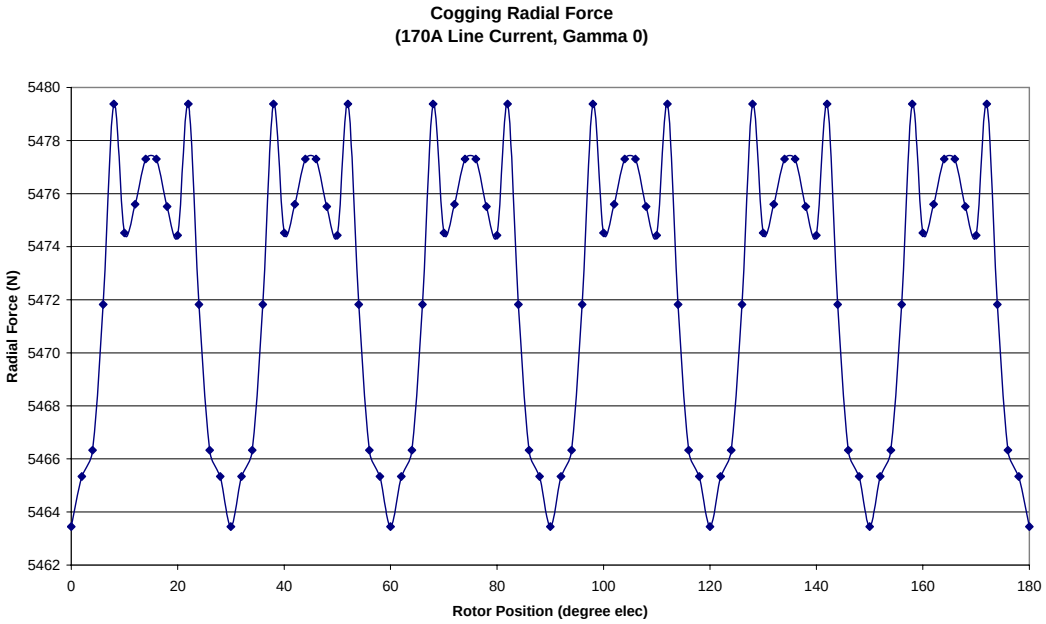

Figure 4.8 Cogging Radial Force

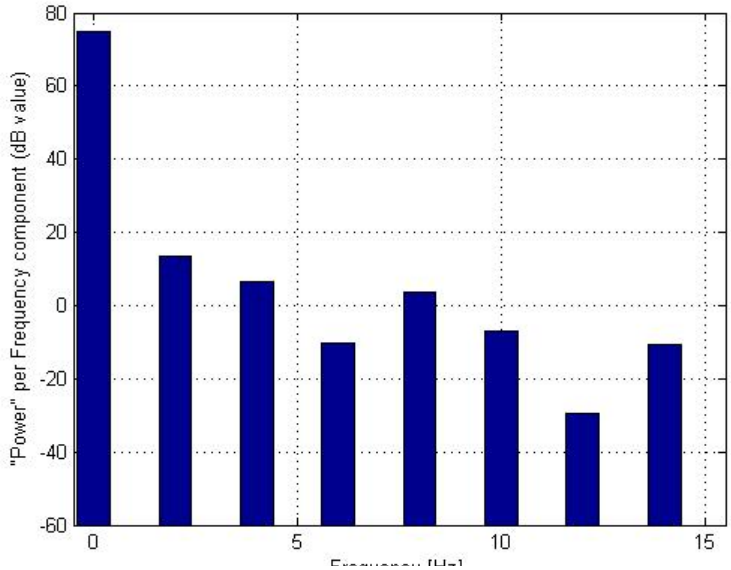

Figure 4.9 Cogging Radial Force Waveform Harmonic Spectrum

As the reader might remember from Chapter III, if a waveform is balanced and symmetric, then there are no odd harmonics as is the case in Figure 4.9, demonstrating that the cogging radial force waveform is balanced and that there are no structural asymmetries or eccentricity causing the cogging force to have odd harmonics.

Electrodynamic radial force however was left out of Figure 4.5 because there was an attempt to summate all of the radial forces as was done with torques in Chapter II; however an issue was discovered with the addition of the forces in that the summation of the forces exceeded the total force. This problem focused on the speculative method of using the FEM to solve for reluctance torque and force, because there are times in the simulation where the dB component of a reluctance force harmonic exceeds the dB "power" of the total radial force harmonic, in which case there is no way that this harmonic can exist, as there is no such thing as adding a negative logarithm in order to make the acoustic or radial force power spectrum sum to the lower total radial force harmonic. Table 4.1 below demonstrates the issue that is being discussed.

Table 4.1 Harmonic Content of the Waveforms Presented in Figs 4.2 and 4.3

Harmonic	Total Force (dB)	Reluctance Force (dB)	Cogging Force (dB)	Electrodynamic Force (dB)
0	84.0712	83.7468	74.793	FALSE
1	31.9577	30.8842	-269.8112	25.362178
2	48.8783	43.4272	13.3191	47.41949
3	17.5857	19.7625	-255.5788	FALSE
4	30.973	32.4017	6.3964	FALSE
5	10.6732	6.3621	-332.3217	8.662558
6	7.8052	12.7016	-10.1508	FALSE
7	-7.066	-0.486	-267.0938	FALSE
8	17.6795	9.8586	3.7256	16.680999
9	-6.038	-5.2535	-252.1793	FALSE
10	6.8486	-21.4267	-7.1893	6.667
11	-15.0683	-8.4053	-265.0184	FALSE
12	0.007	-8.5058	-29.5217	-0.6578875
13	-14.1973	-8.7982	-262.7168	FALSE
14	-1.1782	-16.9387	-10.4756	-1.85398
15	-15.4061	-13.4679	-243.2737	FALSE

It is clear by the harmonics which have FALSE values, that when the real value of the reluctance harmonic exceeds the dB value of the total radial force harmonic, there is no possible solution for the electrodynamic force as adding harmonic content is given by the equations:

$$L_{\Sigma} = 10\log_{10}\left(\frac{P_1^2 + P_2^2 + \ldots + P_N^2}{P_0^2}\right) \tag{4.1}$$

$$\Rightarrow 10\log_{10}\left(\left(\frac{P_1}{P_0}\right)^2 + \left(\frac{P_2}{P_0}\right)^2 + \ldots + \left(\frac{P_N}{P_0}\right)^2\right) \tag{4.2}$$

$$\text{Substituting } \left(\frac{P_i}{P_0}\right)^2 = 10^{\frac{L_i}{10}}, i = 1,2,3..n \tag{4.3}$$

$$L_{\Sigma} = 10\log_{10}\left(10^{\frac{L_1}{10}} + 10^{\frac{L_2}{10}} + \ldots + 10^{\frac{L_N}{10}}\right) \text{(dB)} \tag{4.4}$$

In the case of the above values, n is three and solving these equations for the 3rd component which should be additive, results in a computer equation solver (In this case a Texas Instruments TI-89 Titanium Calculator) giving the result of "false," meaning that there is absolutely no value real or imaginary that fulfills the 3rd acoustic level in the equation, as regardless of the magnitude of decibel, its additive power cannot be less than zero. While this result verifies that the fixed permeability method of FEM should be used to calculate reluctance values in the future, it does not discount that the reluctance force and therefore torque are a reasonable approximation of the actual value, it just means that they are not exactly perfect, which was already supposed in Chapter II.

The second and more useful result that Table 4.1 and Figure 4.5 provides is that, although it was proven that the method of reluctance solving was somewhat inaccurate, they did show that the majority of the power of the total radial force is the result of the reluctance radial force. This result is further substantiated by [25] where Dajaku states that radial force and radial force ripple is greater with more salient machines. If

reluctance radial force is the strongest component of radial force, and the both tangential and radial reluctance forces increase with saliency, then it is logical that when a more salient machine is investigated that the radial force ripple is larger because the primary contributor to those forces (reluctance radial force ripple) has been increased.

4.2.2 Flux Harmonic Component Investigation

In order to support this thesis, a large simulation was run in order to create a data set of many operating points to best determine the acoustically optimal operating points for the test machine. This data set consists of 1656 operating points organized into a 3D matrix with (γ,Θ,I), (load angle, rotor position and line current or secant current) as the axes variables. In order to utilize this data into d-q space there are two methods that may be used, the torque and currents can be transformed as was done in Chapter II, or the harmonic content can be analyzed in order to remove rotor position Θ as a variable and isolate a 2D slice of the matrix. For ease of use, MATLAB m-files were programmed in order to sort, arrange and perform transforms on the operating point data which made them more usable and understandable resulting in the results and figures in this subsection.

The first reasonable investigation of the radial force ripple, seemed to be examining how the harmonic component themselves react the changes in the operating points. The idea was that there could be particular operating points that were "better" or improved for a single chosen or several chosen harmonics. The most important harmonic to this study is the 60^{th} mechanical harmonic, however for completeness and knowledge value, the constant component and the first four harmonics are examined in this section.

Figure 4.10 on the next page shows the response of the constant force component. A Master's Thesis by Jiao at Clemson University, demonstrates that as the field is weakened, radial force weakens. Clearly this is the case, as each of the current line

maintains its relative distance from the neighboring current values and the entire group of currents decreases homogeneously. The effect that is being displayed is exactly what you are doing when you increase the load angle; you reduce the flux in the air gap and are therefore reduce the force on the stator teeth. Considering that a salient machine, such as an IPMSM, will usually be operated in the field weakening regime and this particular machine is always run in this regime per the operation regions shown in Figure 4.3, this result of the previous thesis demonstrates very little.

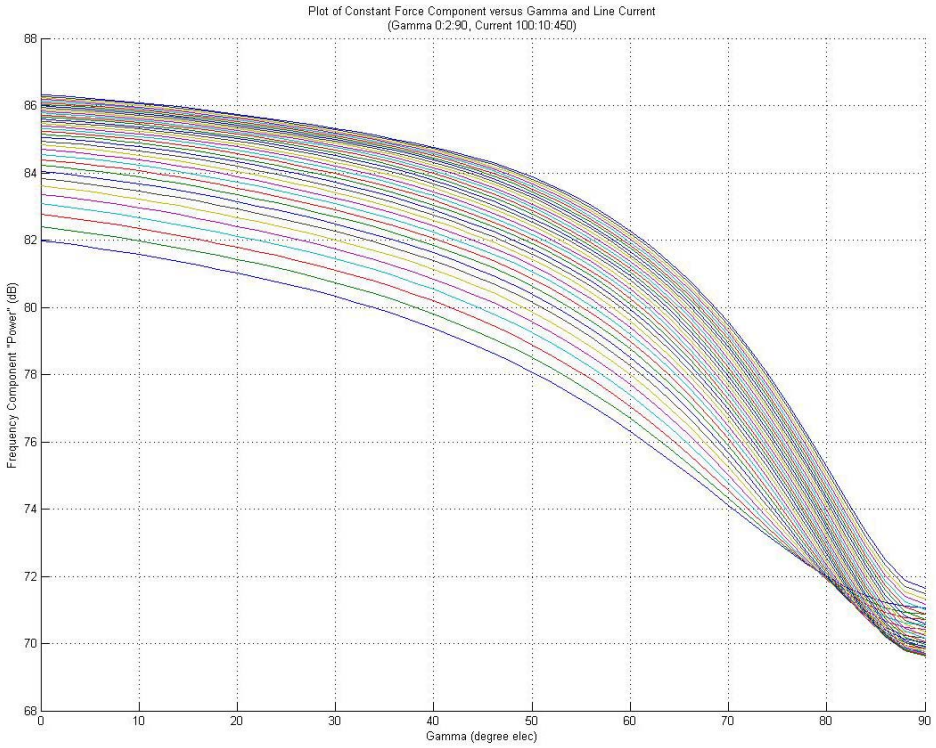

Figure 4.10 Constant Force Component versus Load Angle and Line Current

Following that, the first actual radial force harmonic (30th mechanical or 6th electric) was analyzed. This harmonic shows itself in the spectrograph of Figure 4.1 as a strong noise component in the low speed range of operation. Looking at Figure 4.11 on the next page, it is very clear why this harmonic is so strong at the low speed range, $\gamma = 34^{\circ}_{E} \rightarrow 46^{\circ}_{E}$ is used by the tested control strategy in the MTPA region until

approximately 3000RPM coupled with large line currents to produce high torque values in the sub-base speed range. By using the highest currents to produce torque in the low speed range for acceleration and the particular gammas which are suited for MTPA operation, Figure 4.11 shows that these two operating parameters couple to produce the maximum values of 30th mechanical radial force harmonics for all the operating points investigated. Figure 4.1 shows that this harmonic quickly disappears after ~3000RPM, what this would suggest by inspection of Figure 4.11 is that either the current was greatly reduced or the operating point of $\gamma = 60^{\circ}_{E}$ was reached in the $I_{S,RMS,MAX}$ region of operation, shown by Figure 4.4. Operating point data provided by the industry partner suggests that load angles around $\gamma = 50^{\circ}_{E}$ are used at 2000RPM, so it is quite possible this is the case.

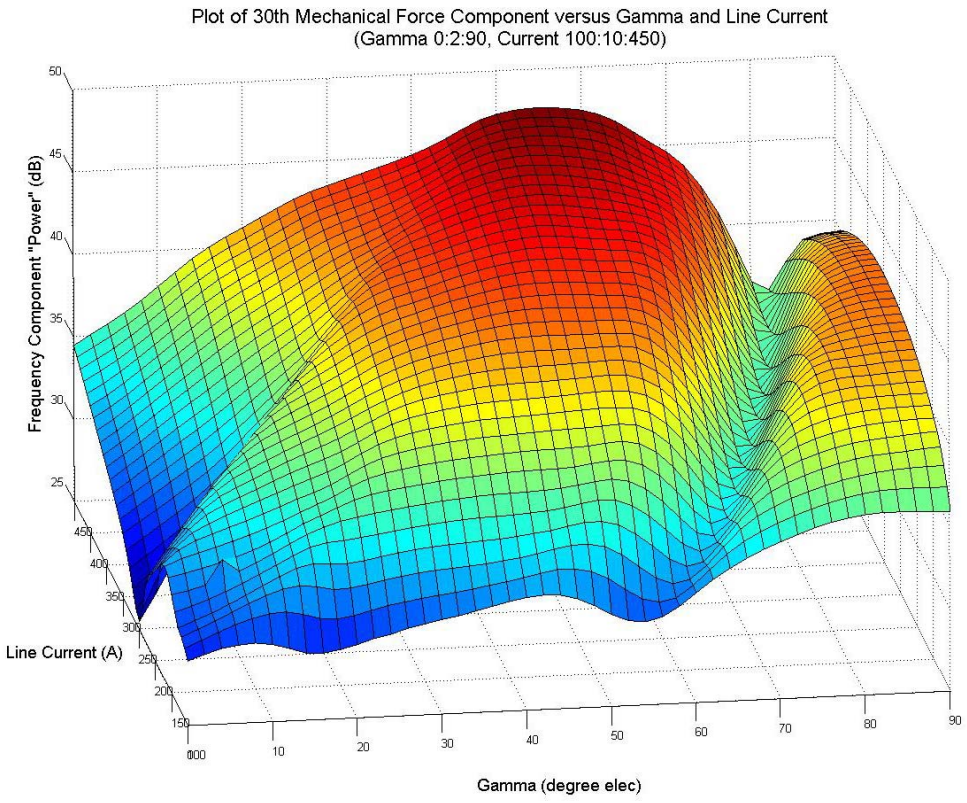

Figure 4.11 30th Mechanical Radial Force Component versus Gamma and Line Current

Once $\gamma = 60^{\circ}_{E}$ is reached in Figure 4.11, the 30th mechanical force component reduces dramatically for all operating currents until $\gamma = 70^{\circ}_{E} \rightarrow 80^{\circ}_{E}$ at which time there is a current dependant minimum reached and then the value of the 30th harmonic begins to increase again. The nature of the local minimum is unknown, but is clearly has some relation to saturation as its phase advances with line current and appears similar to the electrodynamic torque response versus gamma shown in Figure 2.3 and the linearity of the torque response versus gamma in Figure 2.12. To reduce this harmonic the MTPA operation used in the low speed range of the machine could be changed to use a more conventional $\gamma = 0^{\circ}_{E}$ and increasing secant current in order to meet torque command, this seems particularly useful as the highest currents produce the lowest harmonic values in the no to low field weakening regime and therefore fit the operating demands of the below rated speed operation well. Otherwise, a less realistic option is that operating points around the local minimum of $\gamma = 70^{\circ}_{E}$ could be utilized, but this does not make as much sense for the low speed range, despite the fact that the industry partner already uses field weakening in this range.

The second harmonic analyzed is the primary concern of this thesis, the 60th mechanical radial force harmonic. The magnitude of this harmonic with respect to the operating points is shown below in Figure 4.12 and has a noticeably higher scale than the 30th harmonic. The results show that the range of magnitudes for this harmonic is less current dependent than the 30th harmonic and has relatively a small variation due to load angle. What is noticeable is that Figure 4.12 is that after the local minimum, which occurs again around $\gamma = 70^{\circ}_{E}$, the magnitude of the 60th harmonic increases significantly, resulting in much more noise from this harmonic. Operating point data from the industry partner suggests that at 5000RPM a load angle of $\gamma = 70^{\circ}_{E} \rightarrow 80^{\circ}_{E}$ is used and when this is compared to Figure 4.1, this shows that the magnitude of the 60th harmonic grows after 5000RPM, this suggests that similarly to Figure 4.12, the industry partner advances gamma in order to increase speed and in doing so moves into a region where

the acoustic output of the 60th mechanical radial force harmonic increases ~8-10dB or doubles in acoustic intensity compared to values used for machine control in the MTPA region.

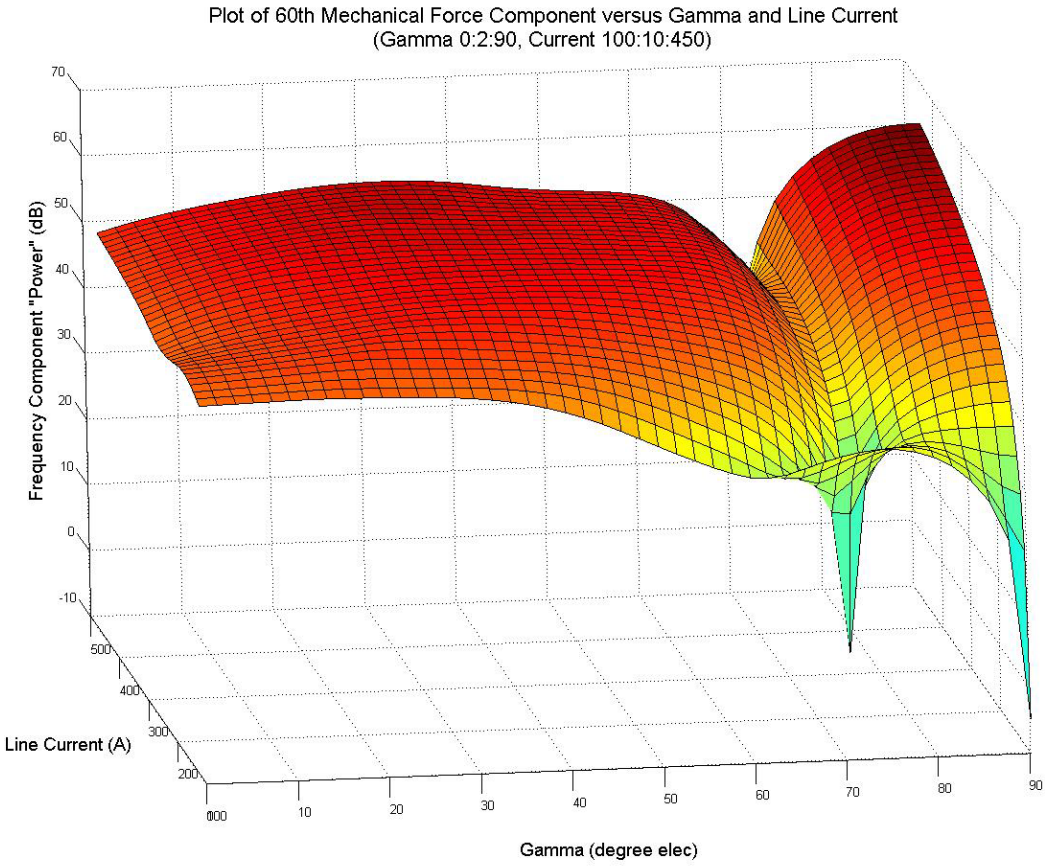

Figure 4.12 60th Mechanical Radial Force Component versus Gamma and Line Current

The limited variance of the 60th radial force harmonic with respect to line current and load angle limit choices of operating points in order to reduce this harmonic with purely sinusoidal currents. As was the result for the 30th harmonic, the 60th harmonic can be reduced by operating near the absolute minimum region of $\gamma = 65^{\circ}_{E} \rightarrow 75^{\circ}_{E}$, which are reasonable load angle values to improve the area of most concern with respect to the 60th harmonic as shown by Figure 4.1. Clearly the issue with that is that if the machine is required to operate faster than $\gamma = 75^{\circ}_{E}$, the 60th harmonic will increase just as it did in

the test provided by the industry partner. In order to provide a better solution to this harmonic, a method utilizing non-purely sinusoidal currents is discussed at the end of this chapter.

The next harmonic is the 90th mechanical radial force harmonic, which is shown on the next page as Figure 4.13. This harmonic has a lower amplitude scale than both the 30th and 60th harmonics and does not manifest itself in the spectrograph of Figure 4.1. However, it is of interest to analyze the range of operating points and examine why this harmonic does not have a high magnitude. The answer to why this harmonic does not manifest itself in the spectrograph is that by the time the operating regions of the industry partner correspond very well to the lower values of this harmonic, compared to the 30th harmonic where the operating regions were the absolute worst for that harmonic. The MTPA operating region uses load angles centered on $\gamma = 40^{\circ}_{E}$, if one inspects Figure 4.13, this is the region which contains the "notch" or local minimum that has been previously seen around $\gamma = 70^{\circ}_{E}$ in the 30th and 60th harmonics and is therefore an excellent place to operate the machine with respect to this harmonic. The constant secant current operating region follows that and increases the load angle, which should produce a higher amplitude for the 90th harmonic in this region, and as expected Figure 4.1 shows that between ~3500RPM and 4500RPM the 90th harmonic shows up with a higher intensity for this brief period and then disappears again. It disappears again because the next machine operating region is the MFPT region, which utilizes progressively lower secant currents with increasing gamma, as was shown in Figure 4.4. What this means is that by looking at the effect in reduced line currents in Figure 4.13 one can note that at lower current levels the level of this harmonic drastically reduces back to levels similar to the MTPA region of operation and is shown likewise in Figure 4.1. Because the natural response of this harmonic functions very well with the industry partner's machine control strategy there is no reason to suggest improvements to purely sinusoidal operating for this harmonic as it is also of minimal concern due to its performance. However, of note is that this harmonic along with the 30th harmonic is an

odd harmonic in the radial force spectrum and because of this it is the product of an asymmetry of the radial force waveform. If that waveform asymmetry was corrected, this harmonic is eliminated entirely. A method of doing that is proposed later in this chapter.

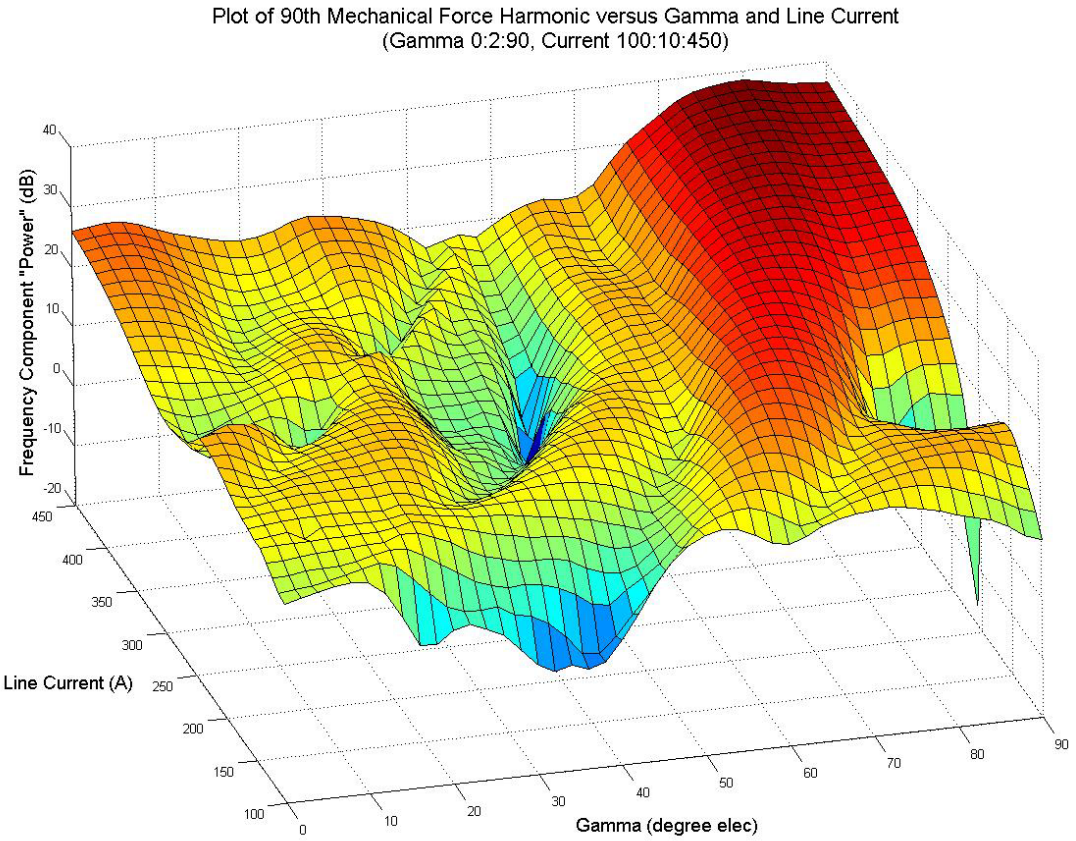

Figure 4.13 90th Mechanical Radial Force Component versus Gamma and Line Current

The final radial force harmonic analyzed is the 120th mechanical harmonic. The response of this harmonic to gamma and line currents is shown on the next page in Figure 4.14. This harmonic was described by the thesis supervisor as of some importance, because there is a localized region of noise in the MTPA operating region of the machine between ~2500RPM to 3500RPM. Observation of Figure 4.14 shows why this local noise problem occurs with this harmonic, similarly to the 30th harmonic, this harmonic has a local maximum region from $\gamma = 35^{\circ}_{E} \rightarrow 65^{\circ}_{E}$, which are precisely the load

angles used by the industry partner for the MTPA region. This effect is compounded like the 30th harmonic due to increased harmonic amplitude due to current, the higher currents required in the MTPA region also produce the highest 120th harmonic values. In Figure 4.1 the 120th harmonic is not very strong before the MTPA region due to its strong reduction with lower load angles.

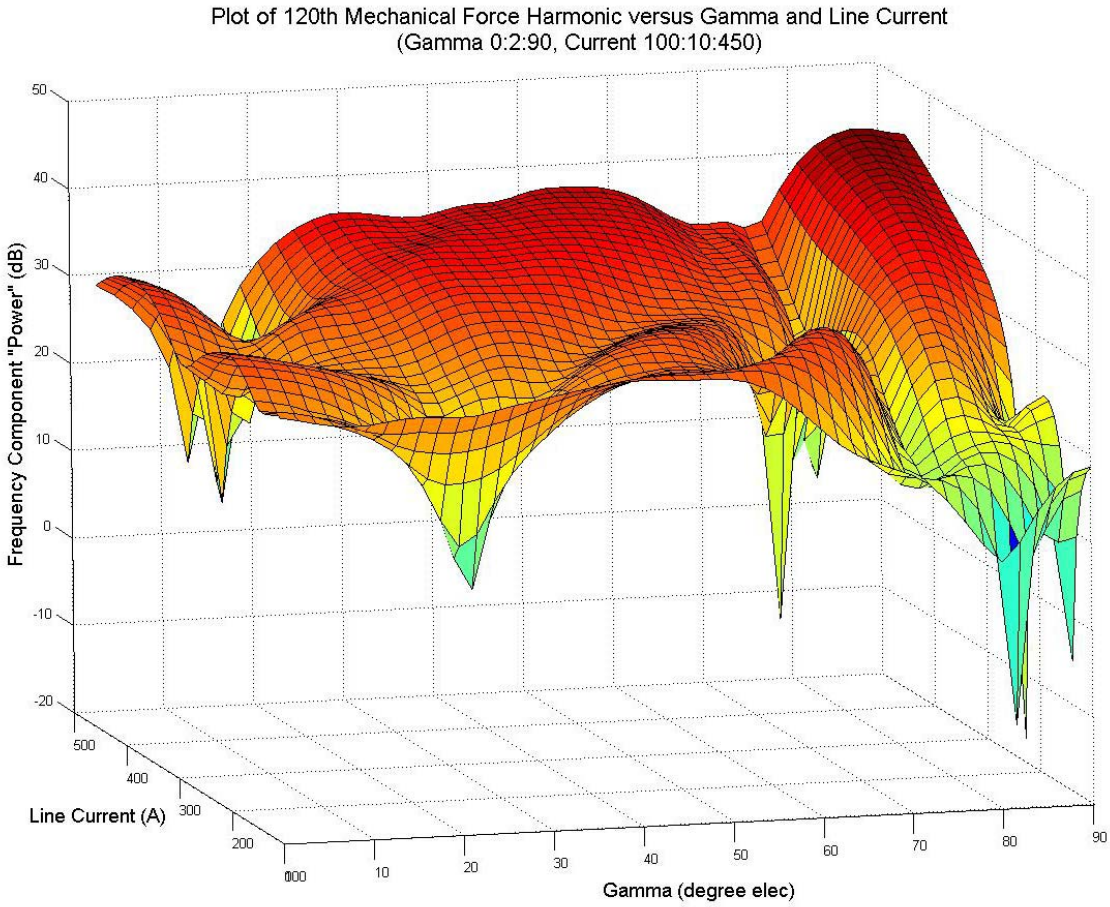

Figure 4.14 120th Mechanical Radial Force Component versus Gamma and Line Current

Following the MTPA region there is the "notch" for all currents which centers on $\gamma = 70^{\circ}_{E}$ and provides dampening of this harmonic during the maximum secant current operating region. Then as the industry partner's control strategy moves into the MFPT region, the amplitude of this harmonic is reduced due to the lower currents that this

operating region utilizes, which offsets the strong harmonic magnitude increase with higher line currents displayed in Figure 4.14.

Due to the requirement that the machine use high current amplitudes in the MTPA operating region and that the load angles of this region are fixed, it does not look like the one area of noise concern for this harmonic can be mitigated with purely sinusoidal currents. Similarly to its even harmonic predecessor the 60th harmonic, in order to eliminate the area of concern for this harmonic, a non-purely sinusoidal current waveform must be injected to better match the back EMF harmonics to the fundamental of the flux. This will be discussed later in the chapter.

4.3 30th Mechanical Harmonic Investigation and Proposed Correction

The issue causing the 30th mechanical harmonic is that there is a radial force waveform imbalance; this is clearly the issue as odd harmonics indicate that there is an asymmetry in the waveform itself. The author believes this imbalance is caused by reduced flux from the coils that reside in slots which contain two separate phases. In order to ensure that this is the case, the simulation FEM model was changed so that the current was able to be controlled individually with six slots rather than three phases. This change was done so that the current and therefore the flux in the half phase slots could be independently controlled without changing the current and flux in the full phase slots. This method also employs utilizing the average of the two current phases in the half phase slots and then boosting this averaged current, this is not possible with a standard three wire system and that is why the model was expanded to six wires and the coils were reassigned.

An initial test was done after the model was changed to verify that the new current control model produced the same waveform as the previous simulations, the operating point of $\gamma = 0^{\circ}_{E}$, 300A $I_{LINE,MAX}$ (259.81A $I_{S,RMS}$) was chosen because due to previous

tests in Chapter II, it was known that this operating point was not in the saturation region but the higher current would produce a very noticeable torque waveform peak imbalance, which is the identifying noise marker of the 30th harmonic in the noise spectrograph of Figure 4.1. Initially this study will use torque waveforms to demonstrate the waveform imbalance, however in the future this will be revised to include only results from the radial force waveform, as these should have been the waveform under study and correction in this section. Figure 4.15 below was the initial baseline of this study, the torque waveform imbalance when the original three phase current control model was fed with purely sinusoidal currents.

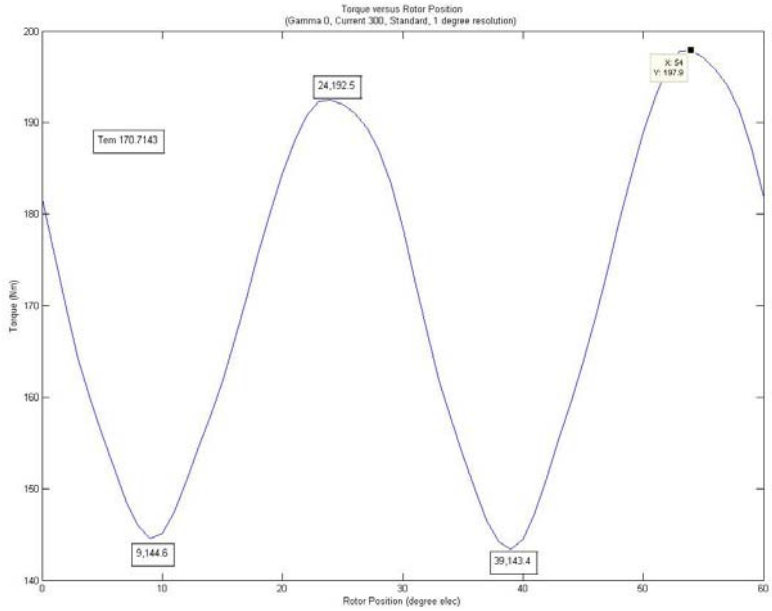

Figure 4.15 Torque versus Rotor Position for (0,300), Original Model

Figures 4.15 above, its harmonic spectrum Figure 4.16 and Figure 4.17 on the following page demonstrate that the new method of current control produces the exact same waveform as was previously used throughout the FEM simulation process; this was a necessary baseline to ensure that the starting point of correcting the waveform asymmetry was the same as experienced using three phase control, which has been proven to accurately reflect the operation and noise results of the industry partner's machine in the previous section.

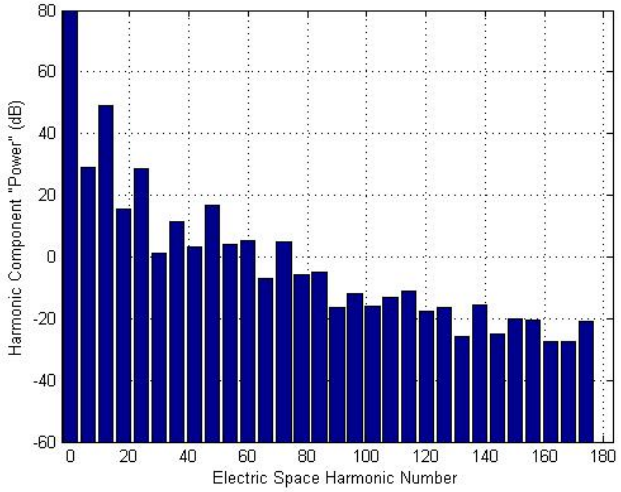

Figure 4.16 Radial Force Spectrum for (0,300), Original Model

The local maximum peaks at 24°_{E} and 54°_{E} are equivalent in both figures as 192.5Nm and 197.9Nm respectively, with a small deviation due to the differing angular resolutions in each figure, as the original method has an angular resolution of 1°_{E} while the six slot control method has an angular resolution of 2°_{E} used to shorten simulation time. The spectrum shows that the original simulation has odd space harmonics and therefore asymmetries.

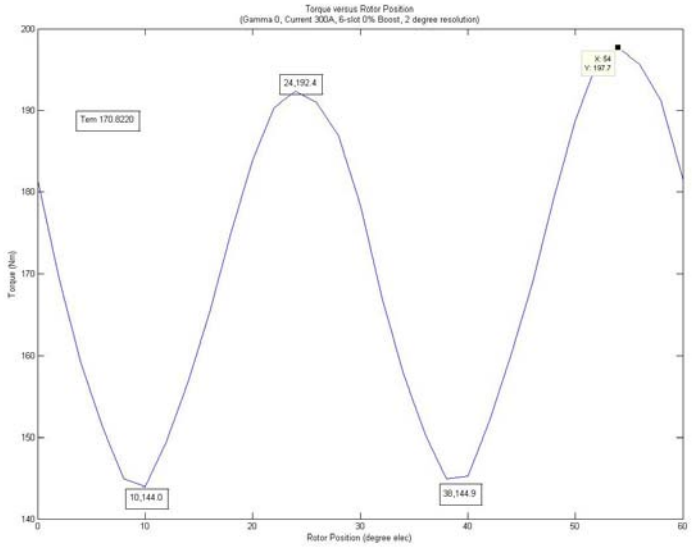

Figure 4.17 Torque versus Rotor Position for (0,300), 6-Slot Model, 0.0% Boost

Following that verification, an iterative process of balancing the peaks of the torque waveform occurred. Initially a small boost of 2.8% was given to the current of the half phase slots. This was done because at this operating point, the average torque per ampere value is ~1Nm/A and thus a desired increase of the lower peak of 2.8% of its value would have seemed to equate to a 2.8% current boost. However, this boost produced an increase of 2.3Nm to the peak at 24°_{E} and a 1.4Nm increase to the peak at 54°_{E}, which provided a maximum deviation improvement of 0.9Nm. This initial test showed that boosting the current and therefore the flux in the half phase slots would increase the amplitudes of the two peaks which are lower than the respective peaks the next half cycle at a rate faster than the peaks whose amplitude is trying to be matched. The original upper peak deviation was 5.2Nm and after the 2.8% half slot current boost, the deviation reduced to 4.4Nm as shown below in Figure 4.18.

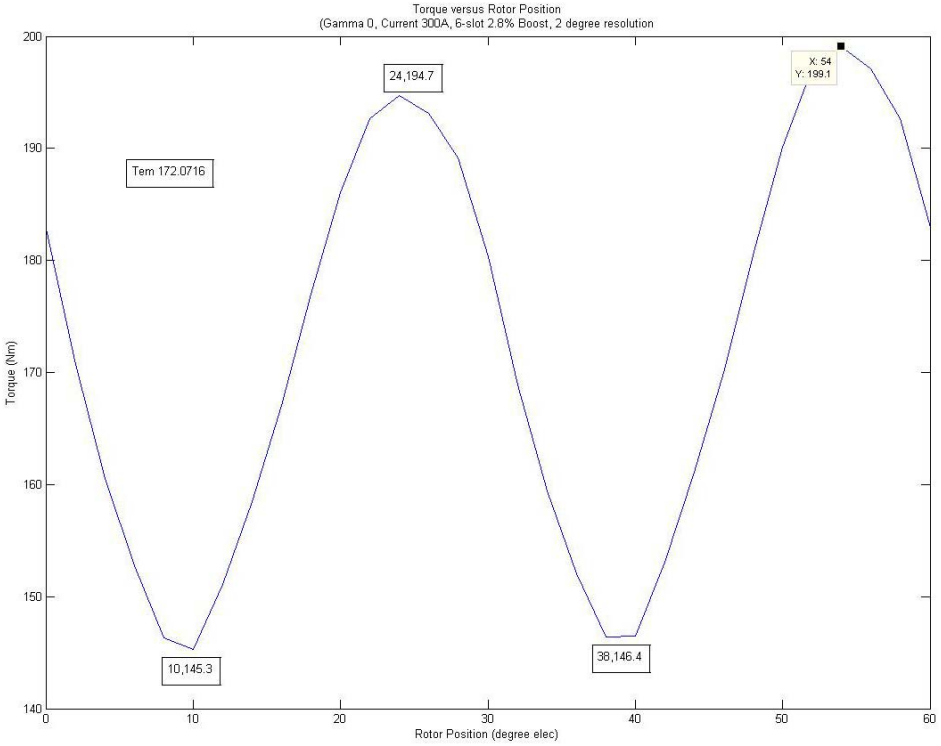

Figure 4.18 Torque versus Rotor Position for (0,300), 6-Slot Model, 2.8% Boost

Following that test and assuming that a linear improvement would follow, the half slot boost was calculated to need 18.2% in order to achieve waveform balance and the currents were adjusted and simulated again. The result of this simulation is show on the next page in Figure 4.19. The figure shows that at the 24°_{E} there was a 17.1Nm increase over the previous boost test and a total of 19.4Nm from the baseline. This drastic boost created a 2.0Nm deviation in the opposite direction, meaning that the peaks that were previously the lower peaks now were higher. The 54°_{E} peak increased only 10.7Nm over the previous result for a total of 12.1Nm total increase.

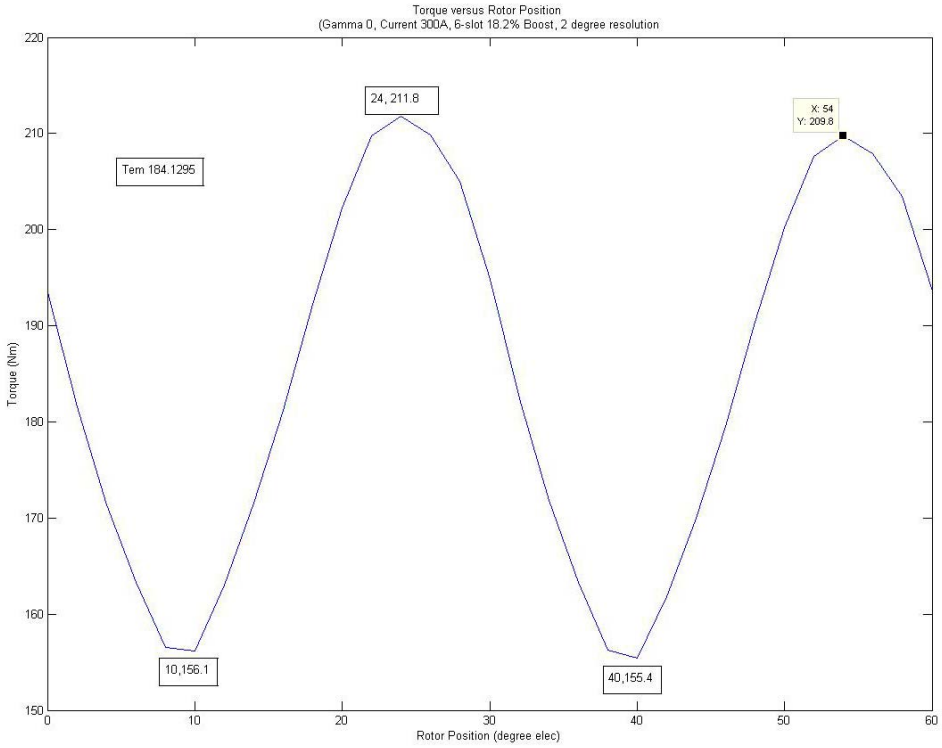

Figure 4.19 Torque versus Rotor Position for (0,300), 6-Slot Model, 18.2% Boost

Considering that the half phase slots had been boosted too much with 18.2%, the next step was to reduce the boost to 12%. This resulted in a 12.1Nm increase over the baseline to 204.6Nm for the 24°_{E} peak and 7.2Nm increase over the baseline to 205.1Nm for the 54°_{E} peak. The deviation between the two peaks was now 0.5Nm and the mean

was 179.17Nm. This was essentially a third intermediate step but it continued to verify that this method could work.

The next step was to increase the boost to 13% for the half phase slots; this resulted in a waveform that was almost completely balanced. The 10°_{E} local minimum was 152Nm and the 30°_{E} following local minimum was 152.1Nm, the 24°_{E} local maximum was 205.7Nm and the 54°_{E} local maximum was 205.8Nm. The deviation between the minimum and maximum peaks was at a maximum of 0.1Nm, however there was still odd harmonics produced from the imbalance of the waveform. The mean value of the torque waveform, or T_{EM} increased from the baseline 9.07Nm, which is similar to the result of a line current 20A higher than the set line current for the simulation, meaning that the injection of the boost currents is equivalent to a 6.7% increase in current in the case of this operating point. All of these critical points are shown below in Figure 4.20.

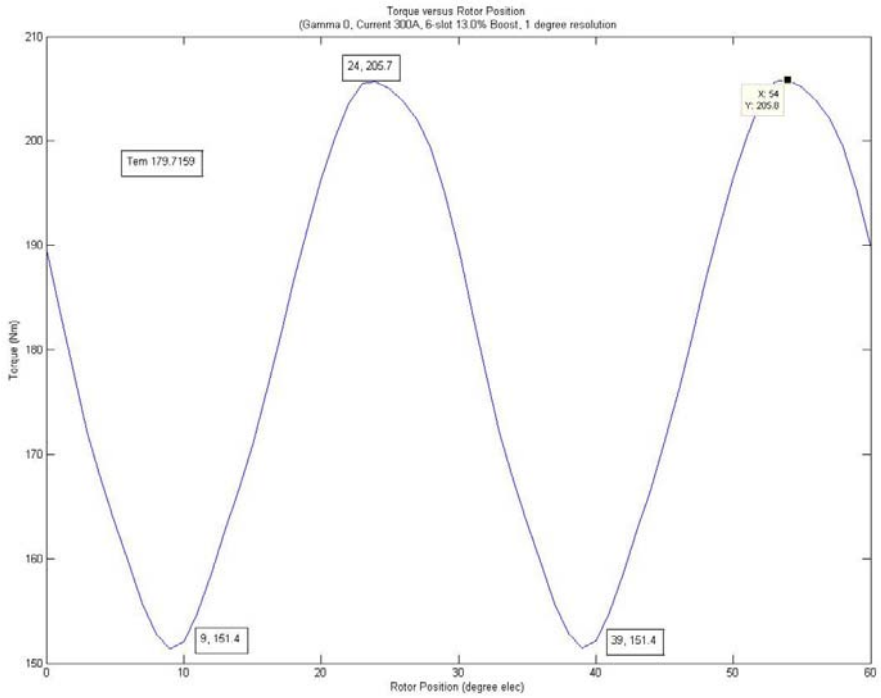

Figure 4.20 Torque versus Rotor Position for (0,300), 6-Slot Model, 13.0% Boost

At this point, the author felt that the odd harmonics were sufficiently improved, however upon conversing with the thesis supervisor, it was suggested that the harmonic spectrum could be improved to an ideal state and was demonstrated how. First he calculated the total average current in the half phase slot versus a normal full phase slot. Following that he used the difference in the average current magnitudes to calculate a boost factor needed to increase the half phase slots to the same average current level as the full phase slots, shown below as 15.47%. This calculation is valid if the method of six-slot control is used where the phase currents are averaged, boosted and then applied to the half phase slot conductors equally.

$$\frac{1}{2}\left(\sin(\theta)+\sin(\theta-\frac{2\pi}{3})\right)=\frac{1}{2}\sqrt{3}\left(\sin(\theta)+\sin(\theta-\frac{2\pi}{3})\right) \tag{4.5}$$

$$\frac{1}{\left(\frac{1}{2}\sqrt{3}\right)}-1=0.1547 \tag{4.6}$$

Upon applying the 15.47% boost specified by the mathematical solution above to the half phase slots the waveform ideally balanced the peaks out as well as the spectrum eliminating all odd harmonics completely, rather than the "very close" solution arrived by iteration. The results of this were that the peaks of the two half cycles had a deviance of 0.0Nm as it was again perfect waveform balance. The 24°_{E} peak had a value of 206.1Nm and the peak at 54°_{E} had a value of 206.1Nm. The local minimums at 9°_{E} and 39°_{E} had values of 151.7Nm and 151.7Nm respectively, which confirms the balance and is shown in Figure 4.21 on the next page. The waveform is also accompanied by Figure 4.22, which is its harmonic spectrum which shows definitively that the waveform is balanced and all of the odd harmonics have been removed.

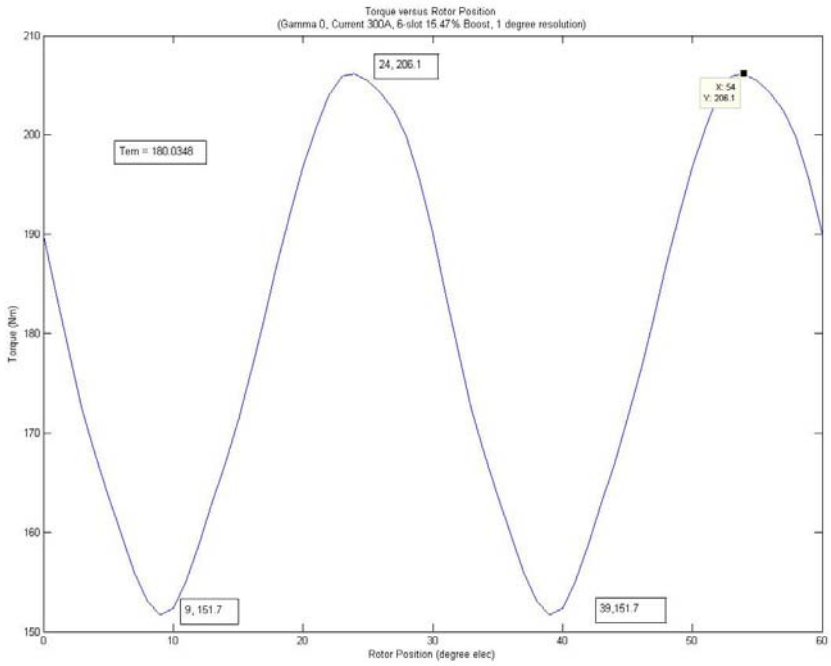

Figure 4.21 Torque versus Rotor Position for (0,300), 6-Slot Model, 15.47% Boost

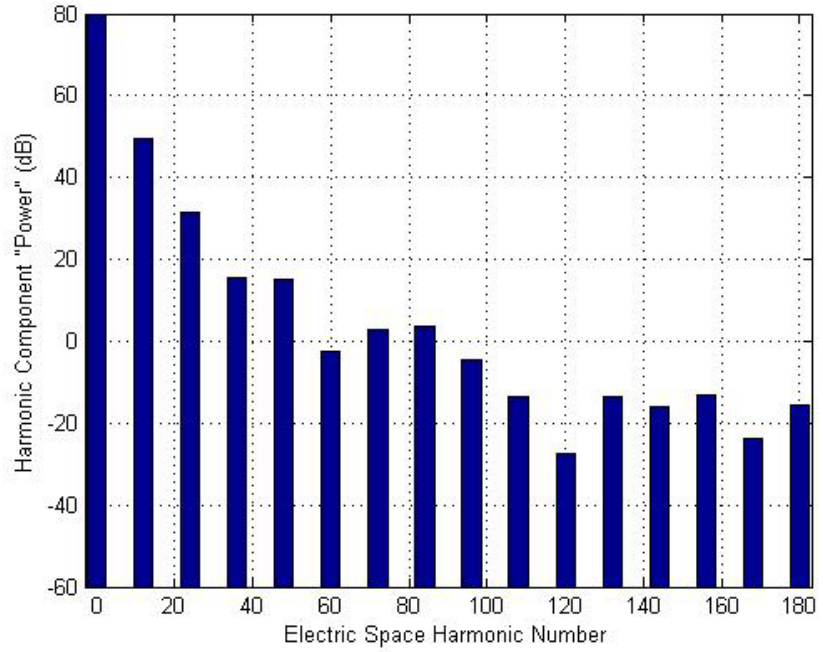

Figure 4.22 Harmonic Component Spectrum for Six-Slot Control (0,300) 15.47% Boost

The next situation to investigate considering this issue was whether the flux boost solution was current and gamma independent, or rather this solution was limited to the one previously explored operating point, or rather this was a product of the machine itself, doing two further tests could isolate the problem and ensure that it was an issue with flux distribution concerned with the half phase slots or if it was something else. The first of these tests was to adjust gamma to another value. In order to ensure a proper baseline for the test, a known and familiar simulation value of $\gamma = 40^{\circ}_{E}$ was used at the previous current of 300A $I_{LINE,MAX}$ (259.81A $I_{S,RMS}$), in order to isolate gamma related response to the half phase slot boosting solution.

The model again shows that the unboosted half phase slots do not effect the operation of the machine and it has the torque peak deviation as before with a much more extreme gamma value; in this case the local maximums have a 4.8Nm peak variance to the peak of the next half cycle as shown in Figure 4.23 on the next page. Following that confirmation that the models retained their agreeance, a simulation was run where the half phase slots were boosted by 15.47% again. The results of this were that the peaks of the two half cycles had a deviance of 0.0Nm as it was again perfect waveform balance. The 19°_{E} peak had a value of 324.89Nm and the peak at 49°_{E} had a value of 324.9Nm. The local minimums at 7°_{E} and 37°_{E} had values of 266.1Nm and 266.1Nm respectively, which confirms the balance and is shown in Figure 4.24 on the next page.

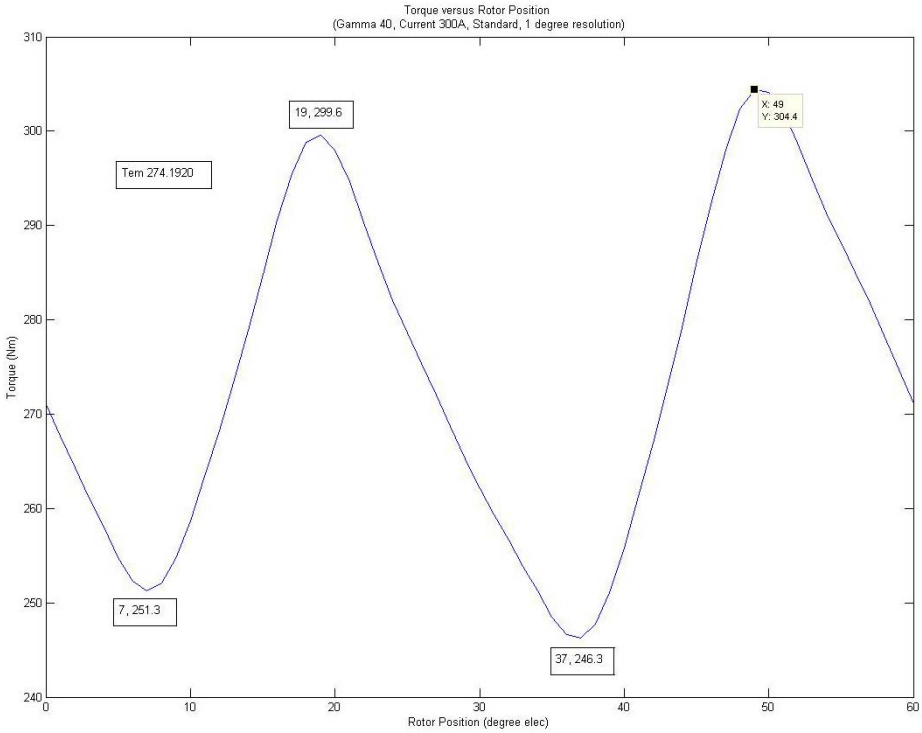

Figure 4.23 Torque versus Rotor Position for (40,300), Original Model

Combined with the boosted torque waveform is also the spectrum of that waveform in Figure 4.25. The spectrum in Figure 4.26 confirms that the waveform is ideally balanced where the approach of looking at the local maxima could hide some waveform deformation; the spectrum shows even minor flaws due to the superior resolution of the decibel scale.

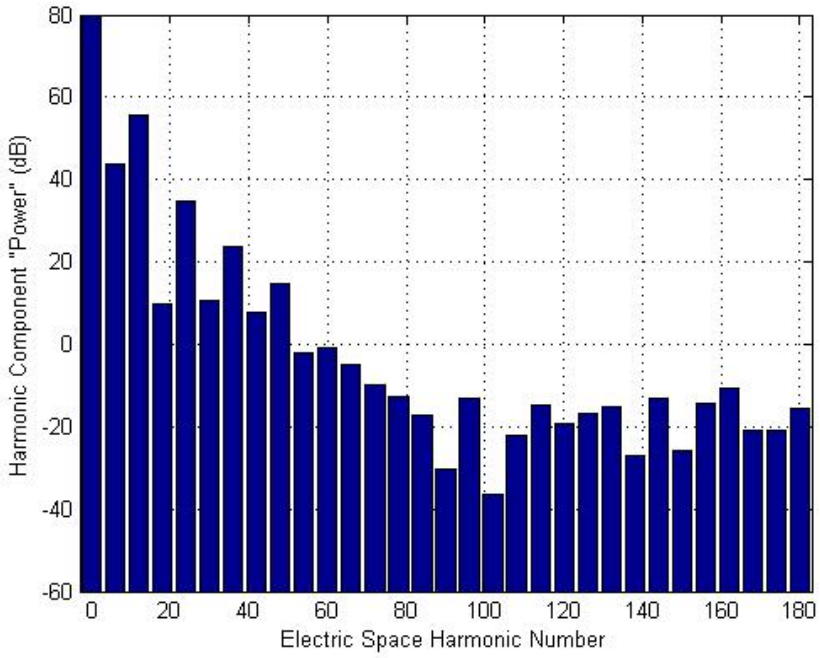

Figure 4.24 Harmonic Spectrum for (40,300) Original Model

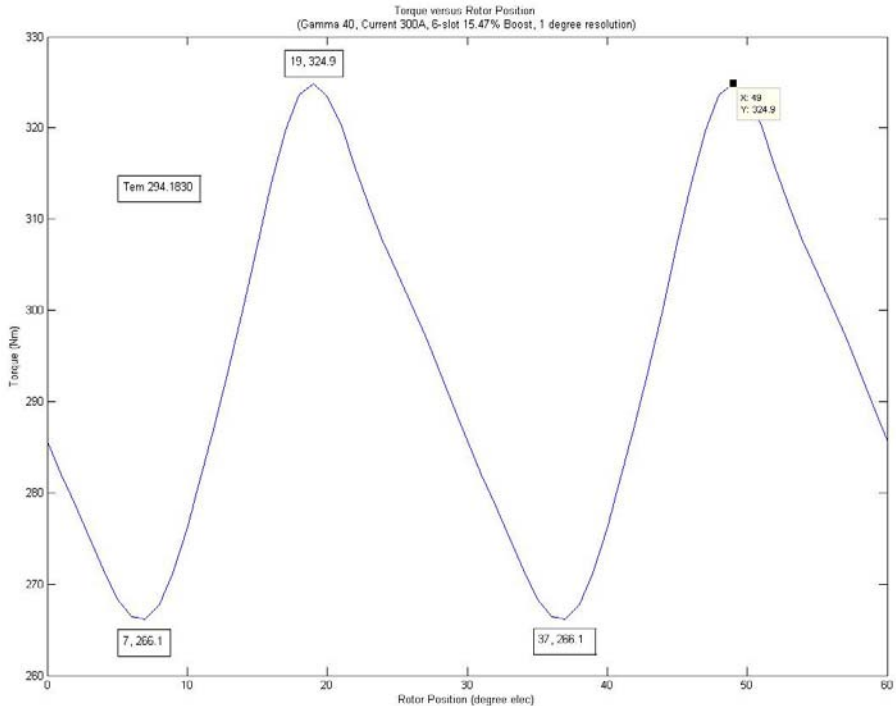

Figure 4.25 Torque versus Rotor Position for (40,300), 6-Slot Model, 15.47% Boost

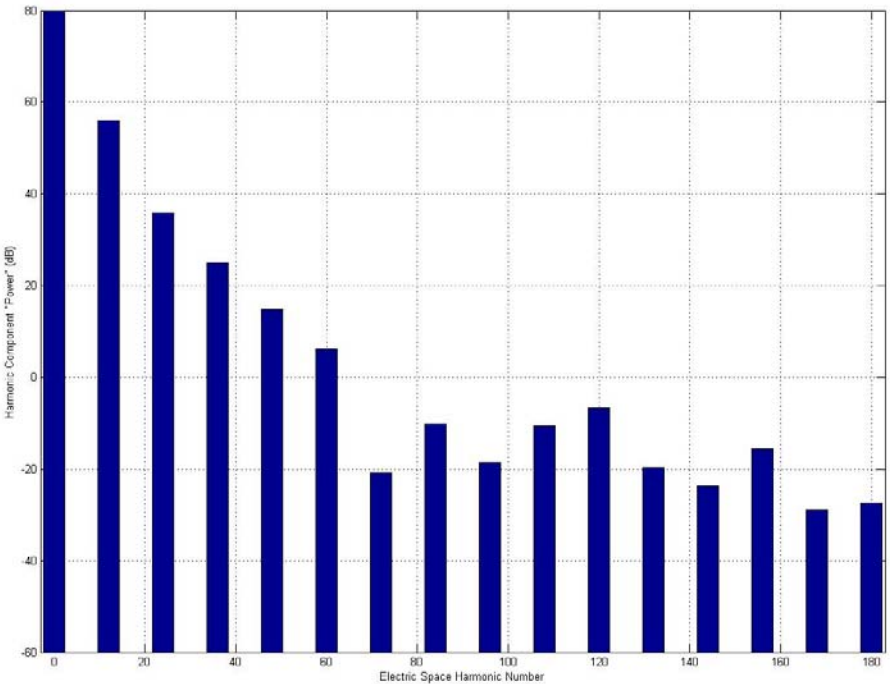

Figure 4.26 Harmonic Component Spectrum for Six-Slot Control (40,300) 15.47% Boost

This result showed that the improvement in the torque waveform and therefore the half phase slot boost method was independent of gamma and a more likely candidate for a winding issue; however a second test had to be conducted in order to isolate that.

The next test that was conducted reduced the simulation current to 200A $I_{LINE,MAX}$ (173.21A $I_{S,RMS}$) and gamma was returned to $\gamma = 0^{\circ}_{E}$ in order to isolate line current as a variable. This current was chosen because it represented a significant drop in current and saturation as well as it was a known value which was within the linear region of machine operation, as was shown in Chapter II. Like the previous tests, the simulation data from the previous control model was read in and analyzed in order to establish a baseline for comparison of the six slot control method and the half phase boost strategy.

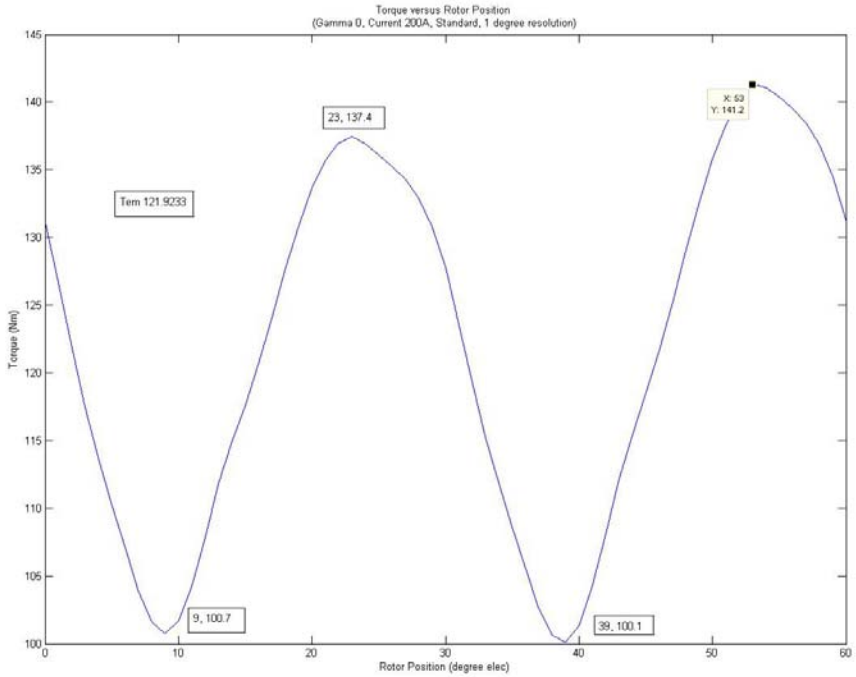

Figure 4.27 Torque versus Rotor Position for (0,200), Original Model

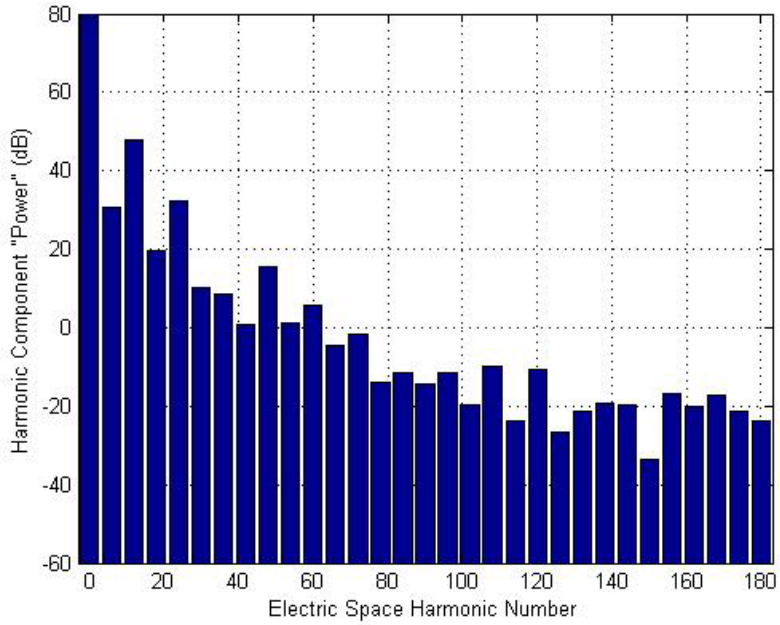

Figure 4.28 Harmonic Spectrum of (0,200), Original Model

This operating point shown in Figure 4.27 and its corresponding harmonic spectrum in Figure 4.28 on the previous page, showed a mean torque of 121.92Nm and peaks of 137.4Nm and 141.2Nm at 23°_{E} and 53°_{E} respectively. The deviation of these two peaks was 3.8Nm reduced from 5.4Nm for the $\gamma=0^{\circ}_{E}$ 300A $I_{LINE,MAX}$ previous operating point. This reduction in peak amplitude deviation corresponds to the reduction in stator current amplitude and no improvement of the flux distribution of the half phase slots, a discussion of the effects of high currents on the local maximum and minimum deviation occurs later in the chapter. Following the baseline data from the complete operating point test, a test was run where the currents in the half slots were boosted 15.47% the same as in the previous evaluations. The results of this simulation was a mean torque of 129.45Nm and peaks of 148.07Nm and 148.0Nm at 23°_{E} and 53°_{E} respectively. The local minimum peaks were 107.3Nm and 107.3Nm at 9°_{E} and 39°_{E} respectively and is shown below in Figure 4.29 and its corresponding harmonic spectrum in Figure 4.30 on the following page. Like the previous validation steps, the spectrum of the balanced waveform is shown on the next page.

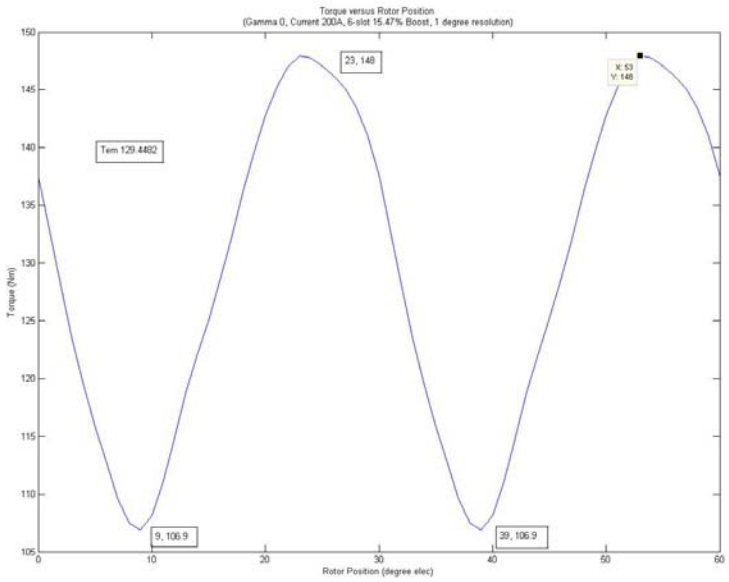

Figure 4.29 Torque versus Rotor Position for (0,200), 6-Slot Model, 15.47% Boost

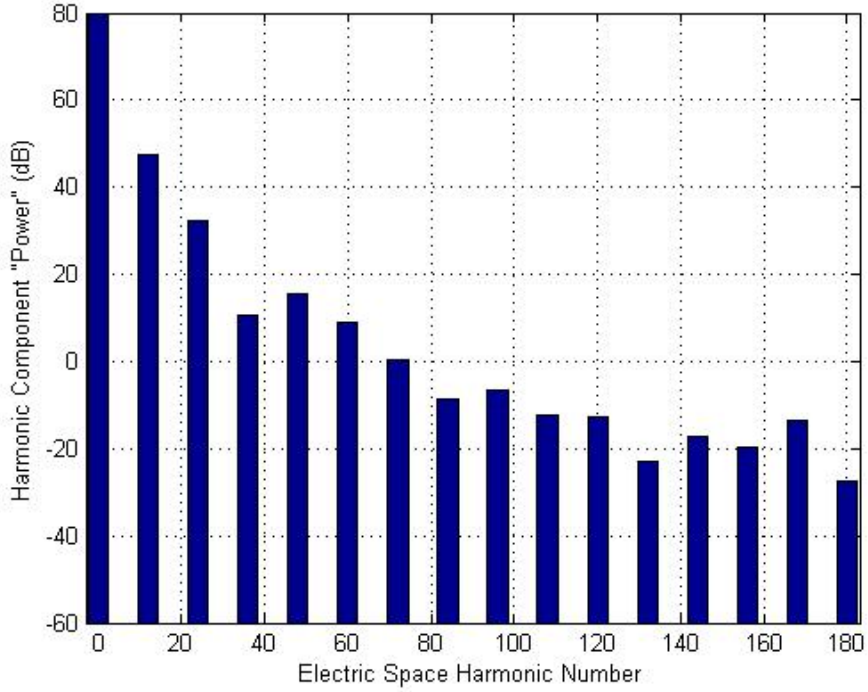

Figure 4.30 Harmonic Spectrum for the (0,200) Operating Point with 15.47% Boost

These results demonstrate that the boosting of the half phase slot currents and therefore flux is both current and gamma independent and is valid for all operating points of the machine. This validates that the flux distribution of the half phase slots is ideally sinusoidal and therefore to create a symmetric sinusoidal flux distribution waveform, as required by PMSM theory, the half phase slots need to have increased flux, there are several methods in which to do this.

In order to more clearly verify the source of the problem, it was suggested that the spatial location of the windings be investigated, in that the “beat” could also be a result of the typical 2-4-2 turn dual layer winding “S” shape of the phase winding distribution and potentially a “T” shaped distribution could solve the imbalance, Figures 4.31 and 4.32 on the following page demonstrates the difference between these two configurations.

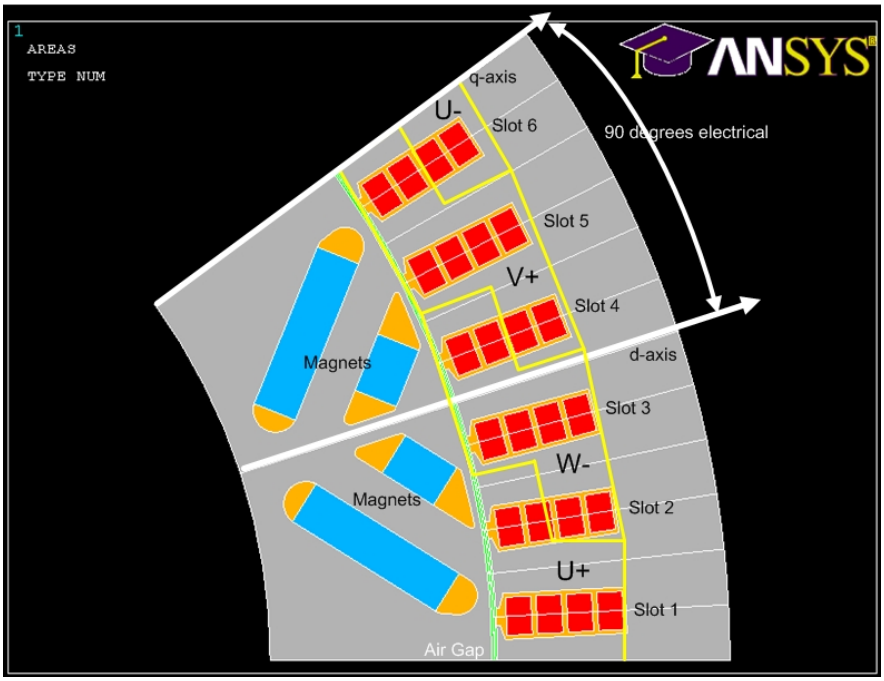

Figure 4.31 Illustration of "S" Phase Assignment of Dual Layer Winding

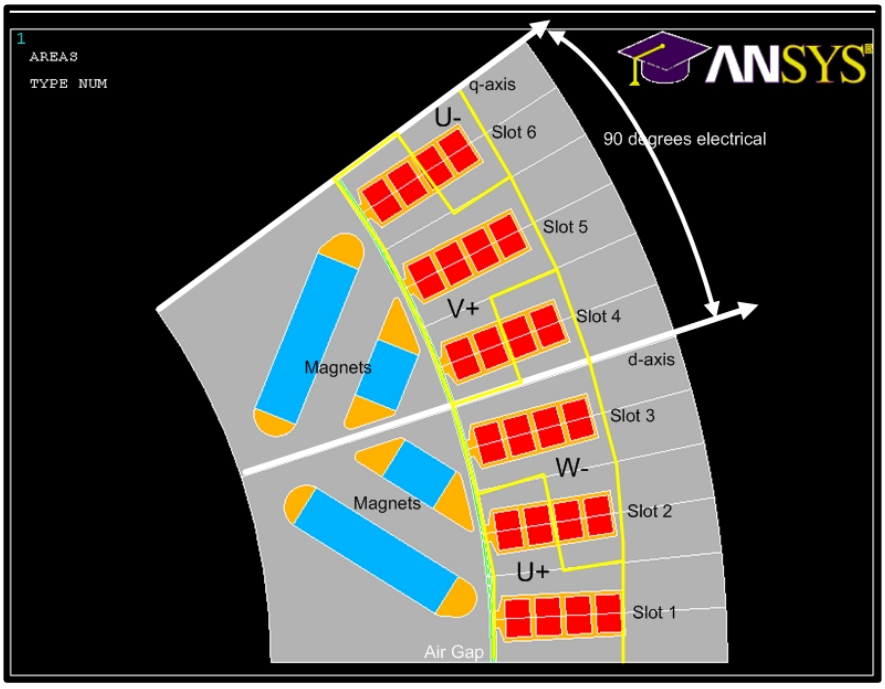

Figure 4.32 Illustration of "T" Phase Assignment of Dual Layer Winding

After conducting a baseline test with no boost, the results showed that there was a 5.5Nm peak deviation with the $\gamma=0^{\circ}_{E}$ 300A $I_{LINE,MAX}$ operating point, and accounting for resolution error, this result was exactly the same as the baseline provided by the previous "S" shaped winding distribution result. The difference in this model was that when the current was boosted 15.47% in the half phase slots, this showed that the orientation of the phases in the slots had an effect on the upper and lower local maxima of the torque waveform independently. Or rather that the position of the turns in the slot affected the bottom or the top peaks, correlating the particular lack of flux to the phase that is more near the airgap. This result was as expected as discussions with other members of the drive group and a recent Doktorarbiet demonstrates that the resultant air gap flux is more heavily dependent on the turns nearest to the air gap.

4.3.1 How to Implement the Flux Distribution Boost Physically

In the previous section I showed that the flux at the ends of the phase windings and the flux distribution needed to be improved, so flux is clearly the problem and there are fortunately several ways to increase flux.

1. Current
    a. Possible with 6 wires as shown in the previous section, but we only have 3 wires with our real machine and I doubt that I will get a complete redesign of a machine and the inverter to fix an acoustic problem.
2. Inductance
    a. Increasing the relative inductance of the coils of the four turns in the half slots would effectively produce more flux per given current. This could be done by using a more inductive material such as a doped copper for those turns and then a normal copper for the full phase slots, I also do not see this happening as it complicates manufacturing the machine, also more inductive wires mean more heat and more losses, which are never the goals of an electric machine. However, it is an option none the less.

3. Winding Geometry
    a. It was suggested that if a “T” shaped dual layer winding was used instead of the standard “S” shaped phase winding this might cause the beat to reduce or be corrected. This was not the case, but it was noted that changing the position of the half phase slot windings caused a change in the top and bottom peaks in the torque and force waveform, more about this will be covered in the next section.
4. Turns per Slot
    a. This would be the ideal way to increase flux by 13% in the half phase slots in a typical wound stator and would be possible, however the particular machine in question does not have conductors which facilitate easily adding additional strands. This factor limits increasing the number of turns in those slots and renders all mechanical options for rectifying the flux distribution impossible to implement.

4.3.2 How to Implement the Flux Distribution Boost Using Three Phase Currents

Based on the previous section it is clear that it is minimally effective to use purely sinusoidal currents to minimize the even harmonics 60,120,180. However it was shown in the previous work by [26] that these harmonics could be effectively reduced by harmonic injection based on simulating the operating cycle for one pole, analyzing the spectrum and then solving the harmonic problems. Because this method must use a calculated force spectrum in order to formulate the proper harmonics for the phase currents, it is not possible to be implemented in the form previously used. However, if the thesis supervisor’s current harmonic injection solution was coupled with a feed forward front-end which utilized pre-calculated radial force spectrums for numerous operating points, it would be highly effective, fast and able to be implemented within inverter software. All of these are all requirements for a solution for the industry partner, as the machine in this study is ready for production and is unable to be altered

mechanically, as suggested in the previous section, in order to reduce radial force harmonics.

This thesis provided a 3D array based on sinusoidal currents parameterized by (γ,Θ,I) for numerous operating points, proving results for force and torque, which were converted into their respective spectral components as well and tabularized. In machine control, machine speed (ω_R) is a dependant variable based on torque. If there is available inverter voltage headroom and a torque command (T*) is given which exceeds rolling and aerodynamic resistance and grade (or more generally load torque T_L) the machine will accelerate, thereby increasing ω_R. Depending on inverter voltage headroom, as determined by backEMF (E), γ and I can be solved numerous ways to fulfill a T*. Using a position encoder to determine the exact rotor position, and using the inverter terminal values to predict the machine response, one can use the 3D array produced by the research supporting this thesis in order to predict the radial force spectrum, or a particular harmonic of the radial force spectrum, at many operating points and eliminate it. This operation would occur in the pre-processing section of the current waveform command, with respect to the torque command, and is completely a software or minimal hardware solution.

The basic logic is that for an operating point, the operator demands a torque to either increase or decrease the speed of the vehicle T*, at this point the search function uses a pre-formulated 3D matrix of operating points which determines the available operating point parameters for the commanded torque (γ and I), as well as the expected resulting torque and force spectrums with complete spectrum or desired specific k values, in this case k = 3 is of most interest as this relates to the 60^{th} electrical force harmonic.

Based on the input parameters of: T*, ω_R, ε (the amplitude of the tolerance band for the torque command) and k (the desired harmonic) the "Hunter" m-file will provide the subsequent operating points for the entire machine which fulfill these values without

exceeding maximum machine power or maximum inverter current capability. Figure 4.33 below shows the user input interface of the Hunter.m MATLAB macro.

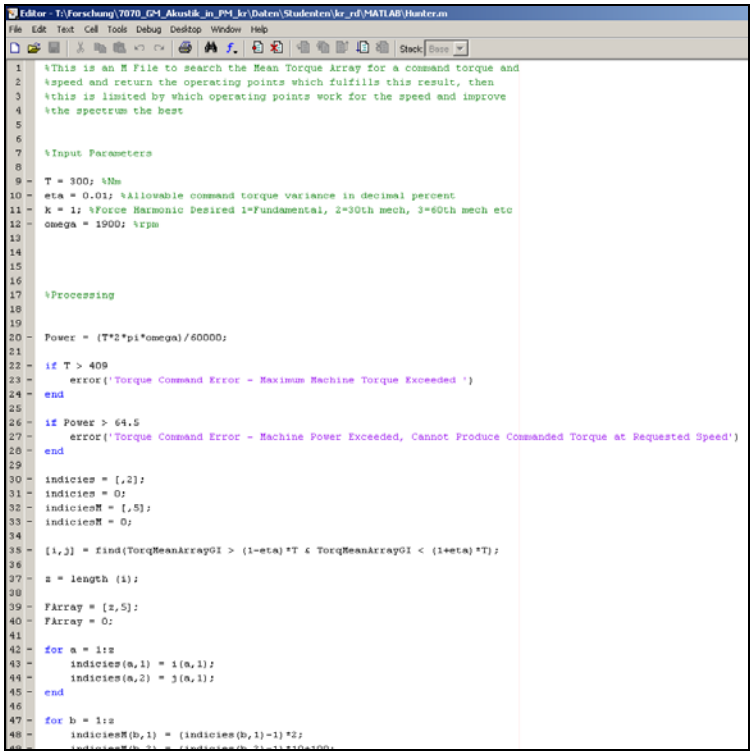

Figure 4.33 Display of Hunter.m and the Required Input Parameters

The exact process of finding the operating points at this time is:

1. Load FRadArray.mat and TorqArray.mat, these are data files which each contain a 61x1656 array of γ, and I versus Θ
2. Run QuickPlot.m, this was originally a plotter program, but have evolved into creating "servant" or sorted arrays which are necessary and helpful. It also has the ability to plot the dB magnitudes of various current components versus gamma based on an input harmonic value k.
3. Set Parameters in Hunter.m
4. Run Hunter.m (F5)
5. View the output file FArray.mat

In the FArray.mat file the following data is displayed for all data points that meet the previously stated search conditions, as displayed in the right panel of Figure 4.34 below. The first column is the k^{th} harmonic's magnitude in decibels. The 2^{nd} coulumn is the load angle; the 3^{rd} column is the line current, which is converted to secant rms current in column 4. The 5^{th} column is I_D and then the 6^{th} column is I_Q. Following this operation is needed a "filter" type level where another level of logic chooses what is the best of these operating points. Such a filter could be based on least ohmic losses, or choosing the harmonic value with the lowest magnitude in order to decrease the amplitude of required current harmonic injection to reduce that harmonic.

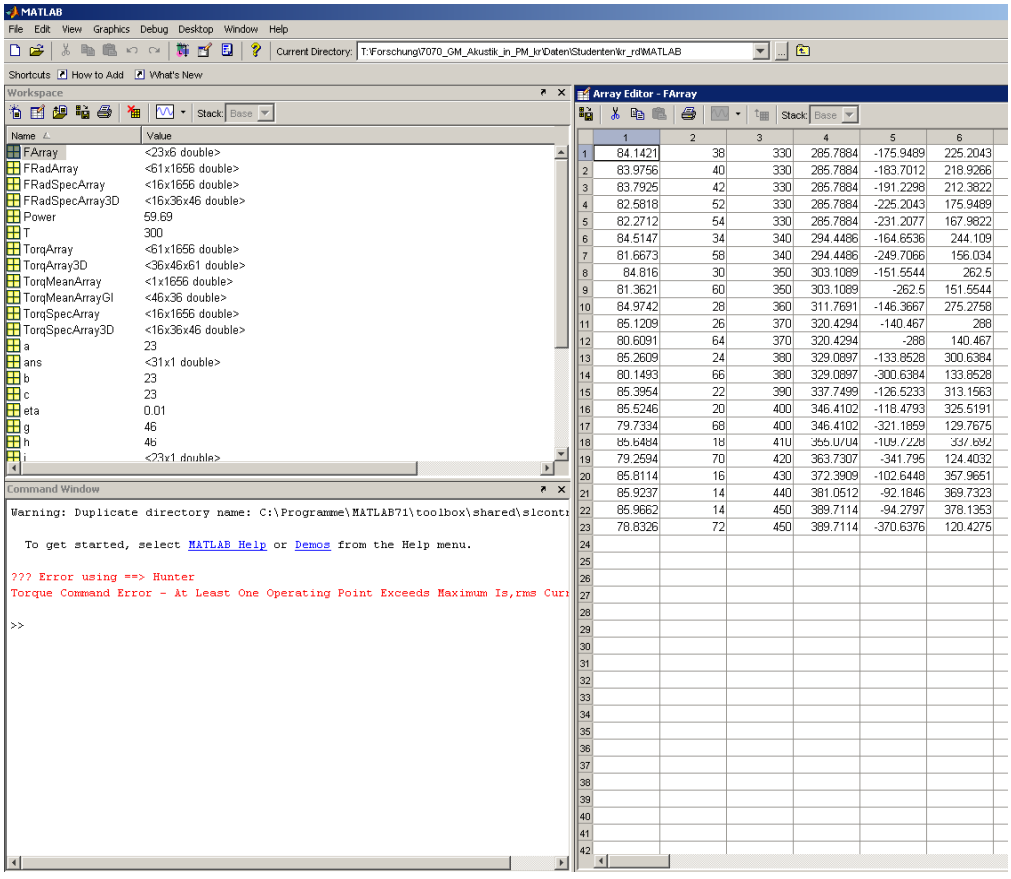

Figure 4.34 The Output of the Hunter.m MATLAB Macro – FArray

CHAPTER V
CONCLUSION

This thesis has been successful in the primary goal of examining and developing a control strategy in order to reduce the noise caused by electromagnetic causes in a particular PMSM in development by an industry partner of ISEA. The research carried on work by Mr. Matthias Boesing and expanded the knowledge of this machine in both its operation and noise reduction.

The particular results of this research were that an idea of the permanent magnet flux was discovered along with the d and q axis inductances. Furthermore, the effects of saturation on machine operation were investigated and the linearity of torque was explained with regards to the load angle and line currents.

In the radial force chapter, the sum and harmonics of the radial force of this machine was investigated. It was found that the 30^{th} mechanical harmonic of the radial force was due to a flux asymmetry due to low currents in the half phase slots of the dual layer stator winding. It was shown that this harmonic and its higher order multiples could be ideally eliminated through one process, boosting current in the half phase slots. This particular solution is not readily available as an add-on solution to the industry partner and therefore the large 3D array of operating points used to support this thesis was developed into a pre-processing unit that could be implemented in software for Mr. Boesing's previously discovered harmonic injection strategy to eliminate targeted radial force harmonics. The primary areas that must still be investigated with respect to this machine is to verify the results of flux linkage and the d and q axis inductances as well as develop a mathematical model from those values which does not require a large pre-simulated table of operating points, as this solution did. Also, an exact study on the method of control utilized by the industry partner could further support or improve the supposed relationships between the radial force harmonics and the noise spectrograph.

Furthermore, the results from this thesis must be combined with further research that takes into account the discomfort of the occupants of a vehicle with respect to which frequency harmonics are important to cancel. It was considered throughout the thesis that the most important mechanical frequency harmonic was the 60^{th} harmonic; however it is possible that at higher speed ranges, lower harmonics are more critical due to their perception to the occupants of the car. Finally, that data needs to be applied to efficiency models of the machine in order to determine if improving the noise quality of the machine is compatible with desired efficiency, or to what degree can the two aspects be compatible.

REFERENCES

[1] M. Ehsani, *Modern Electric, Hybrid Electric, and Fuel Cell Vehicles*, Boca Raton, FL, CRC PRESS, 2005.

[2] United States Central Intelligence Agency, *CIA World Factbook – United States, Canada, National Debt List, Proved Oil Reserves*, https://www.cia.gov/library/publications/the-world-factbook/index.html, retrieved February 28, 2008.

[3] S. Holditch, "Oil and After," *Texas A&M Engineer Magazine, Premier Edition – The Energy Issue*, Texas A&M Engineering Communications, 2006.

[4] D. Mayes, "Texas A&M Agricultural Economist Shares in Nobel Peace Prize," *AgNews*, Texas A&M Agricultural Communications, October 18, 2007.

[5] *Wikipedia*, "Combustion," http://en.wikipedia.org/wiki/Combustion, retrieved February 28, 2008.

[6] R.Y. Barazarte, R. Doolittle, G.G. Gonzales, "A Comparison of Liquid and Gaseous Fuels for Vehicles," Hybrid Vehicle Additional Course Project, ELEN 686, Texas A&M University Electrical Engineering, December 2006.

[7] J. Quain, *Popular Mechanics Magazine*, "Super Trains: Plans to Fix U.S. Rail Could End Road & Sky Gridlock," December 2007.

[8] N. Mohan, *Electric Drives: An Integrative Approach*, MNPERE, Minneapolis, 2003.

[9] R.W. De Doncker, "Modern Electric Drives: Design and Future Trends," *IEEE 5th International Power Electronics and Motion Control Conference (IPEMC),* Shanghai, China, 2006.

[10] T. A. Lipo, *Introduction to AC Machine Design*. University of Wisconsin, Madison, WI, 2nd edition, 2004.

[11] Driving America's Future, "A Real Solution," http://www.drivingamericasfuture.org/docs/fundsforalternativefuels, retrieved February 28, 2008.

[12] Texas Transportation Institute, "2007 Urban Mobility Report," Texas A&M University System, College Station, TX, September 2007.

[13] *Wikipedia*, "BMW 1-Series," http://en.wikipedia.org/wiki/BMW_1_Series, retrieved February 28, 2008.

[14] BMW Group, "The New Two-Mode Hybrid System from the Global Hybrid Cooperation," *27th International Vienna Motor Symposium*, Vienna, additional handout packet, Austria 2006.

[15] J.M. Miller, "Comparative Assessment of Hybrid Vehicle Power Split Transmissions," *US Army Vetronics Institute 4th Annual VI Workshop Series*, Warren, MI, January 10-13, 2005.

[16] M. Vella, *Business Week*, "At L.A. Show Hybrids Are Big," http://www.businessweek.com/autos/content/nov2007/bw20071114_511094.htm, November 15, 2007, retrieved February 28, 2008.

[17] D. Kiley, *Business Week*, "Is GM's Green Tech Better Than Toyota's?," http://www.businessweek.com/autos/content/nov2007/bw20071113_975898.htm, November 14, 2007, retrieved February 28, 2008.

[18] *Wikipedia*, "Two Mode Hybrid," http://en.wikipedia.org/wiki/Two-Mode_Hybrid, retrieved February 28, 2008.

[19] "SEL Transmission" (in English), Department of Mechanical Engineering, Technical University of Chemnitz, http://www.tu-chemnitz.de/mb/MaschElem/SEL.php, retrieved February 28, 2008.

[20] D. Schmitz, "Analysis of Noise Quality Development of Permanent Magnet Synchronous Machines for Use in Vehicles" (in English), Diplomarbeit, ISEA, RWTH Aachen, 2007 (unpublished).

[21] *Wikipedia*, "List of Hybrid Vehicles," http://en.wikipedia.org/wiki/List_of_hybrid_vehicles, retrieved February 28, 2008.

[22] P. C. Krause, O. Wasynczuk, and S. D. Sudhoff, *Analysis of Electric Machinery and Drive Systems*. Wiley-IEEE Press, Hoboken, NJ, 2002

[23] R. Doolittle, N. Frank, A. Skorcz, *Design of a High Speed PMSM for Vehicular Applications*. Electrical Engineering 612, Motor Design Course Project, December 2006.

[24] D.W. Novotny, T.A. Lipo, *Vector Control and Dynamics of AC Drives*, Oxford University Press USA, New York, NY, 1996.

[25] G. Dajaku, “Electromagnetic and thermal modeling of highly utilized pm machines,” Ph.D. dissertation, Institut für Elektrische Antriebe und Aktuatorik; Universität der Bundeswehr Münchnen, 2006.

[26] M. Bösing, “Noise emission in permanent magnet synchronous machines,” Master's thesis, Intitute for Power Electronics and Electrical Drives, RWTH Aachen University, 2007.

[27] J. Gieras, C. Wang, J.C. Lai, *Noise of Polyphase Electric Motors*, CRC Press, Boca Raton, FL, 2006.

[28] B.-H. Bae, N. Patel, S. Schulz, and S.-K. Sul, “New field weakening technique for high saliency interior permanent magnet motor,” in *Industry Applications Conference, 2003. 38th IAS Annual Meeting. Conference Record of the*, vol. 2, Oct. 2003, pp. 898–905.

[29] M. Meyer and J. Bocker, “Optimum control for interior permanent magnet synchronous motors (IPMSM) in constant torque and flux weakening range,” in *12th International Power Electronics and Motion Control Conference*, Portoroz, Aug. 2006, pp. 282–286.

[30] J. L. Kirtley Jr., *Electric Machines*. Department of Electrical Engineering and Computer Science, Massachusetts Institute of Technology, 2005.

[31] O. Wallmark, “Control of permanent-magnet synchronous machines in automotive applications,” Ph.D. dissertation, Division of Electric Power Engineering, Department of Energy and Environment, Chalmers University of Technology, 2006.

VITA

Randy Gene Doolittle received his Bachelor of Science degree in Electrical Engineering from Texas A&M University – College Station in 2006. He chose to attend Texas A&M University for graduate school to study electrical engineering in September 2006. He received his Master of Science degree in May 2008. His thesis was based on the analysis and noise reduction of permanent magnet synchronous machines. His research interests are international energy use, electric machine design, diesel motor based hybrid platforms and liquid renewable fuels.

Mr. Doolittle can be reached at RandyDoolittle@gmail.com or through his advisor Dr. Mark Ehsani, Professor, Department of Electrical and Computer Engineering, 3128 TAMU, Texas A&M University, College Station, TX 77843.